THE UNIVERSITY OF CHICAGO

DIRECT OPTICAL LITHOGRAPHY OF COLLOIDAL INORGANIC NANOMATERIALS FOR PHOTONIC AND OPTOELECTRONIC APPLICATIONS

A DISSERTATION SUBMITTED TO

THE FACULTY OF THE DIVISION OF THE PHYSICAL SCIENCES

IN CANDIDACY FOR THE DEGREE OF

DOCTOR OF PHILOSOPHY

DEPARTMENT OF CHEMISTRY

BY

JIA-AHN PAN

CHICAGO, ILLINOIS

JUNE 2022

Table of Contents

List of Figures v

List of Tables x

Acknowledgements xi

Abstract xiii

Chapter 1. Introduction 1

1.1. Introduction to colloidal nanomaterials 1

1.2. Devices from colloidal nanomaterials 4

1.3. Direct optical patterning of functional inorganic nanomaterials (DOLFIN) 7

1.4. Chapter bibliography 9

Chapter 2. Photosensitive ligands and additives for solubility modulation of colloidal nanomaterials 14

2.1. Selection of photosensitive ligands and additives for patterning nanomaterials 14

2.2. Interaction forces between colloidal NCs 15

2.2.1. Van der Waals interactions 15

2.2.2. Steric interactions 16

2.2.3. Electrostatic double-layer interactions 17

2.3. Numerical evaluation of the electrostatic double-layer interactions 18

2.4. Patterning NCs with light-sensitive stabilizing ligands 20

2.4.1. Ammonium Dithiocarbamate (ADC) 21

2.4.2. Butyldithiocarbamate (*Bu*-DTC) 22

2.4.3. Potassium Ethyl xanthate (PEX) 23

2.4.4. 5-Mercapto-1-methyltetrazole (MTT) 24

2.4.5. 1,2,3,4-thiatriazole-5-thiolate (TTT) 25

2.4.6. Ammonium 1,1-dithiooxalate (DTO) 27

2.5. Patterning NCs with photosensitive additives 27

2.6. Mechanisms of solubility modulation of NCs by photosensitive ligand/additive 29

2.7. Summary 32

2.8. Chapter bibliography 32

Chapter 3. Direct optical lithography of colloidal metal oxide nanomaterials for diffractive optical elements with 2π phase control 36

3.1. Introduction to oxide NC patterning 36

3.2. Selection of diazo-2-naphthol-4-sulfonic acid (DNS) as the photosensitive compound.... 39

3.3. Photochemically active oxide NP inks 43

3.4. Insights into the mechanism of patterning oxide NPs with DNS 46

3.5. Direct optical lithography of oxide NPs with DNS. 51

3.6. Characterization of amorphous ZrO_2 NP-SICA films. 57

3.7. Fabrication and testing of oxide NP gratings 60

3.8. Tunability and miscibility of oxide NPs for compositional and microstructural control... 64

3.9. Discussion on NPs that require more optimization. 66

3.10. Conclusion 68

3.11. Materials and methods. 69

3.12. Chapter bibliography. 72

Chapter 4. Direct optical lithography of $CsPbX_3$ nanocrystals via photoinduced ligand cleavage with post-patterning chemical modification and electronic coupling 77

4.1. Introduction.....77

4.2. Direct optical patterning of $CsPbX_3$ NCs with oxime sulfonate esters.....79

4.3. Patterning mechanism of $CsPbX_3$ NCs with oxime sulfonate esters 83

4.4. Emission color tuning of the LHP NC patterns 92

4.5. Photoconductivity of patterned $CsPbBr_3$ NC films.....96

4.6. Conclusion 97

4.7. Materials and methods.....97

4.8. Chapter bibliography.....101

Chapter 5. Ligand-free direct optical lithography of bare colloidal nanocrystals via photo-oxidation of surface ions with porosity control 107

5.1. Introduction.....107

5.2. Photo-oxidation patterning of NCs.....110

5.3. Investigating the mechanism of photo-oxidation patterning 114

5.4. Porosity control of patterned NC films.....119

5.5. Summary.....122

5.6. Materials and methods.....123

5.7. Chapter bibliography.....127

Chapter 6. Conclusions and Outlook 133

6.1. Thesis summary 133

6.2. Future directions.....134

List of Figures

Figure 1.1. The diversity of colloidal nanocrystals (NCs) in composition, size, and shape. 2

Figure 1.2. Schematic of the hot-injection synthesis of ZnSe NCs 3

Figure 1.3. Schematic of the heat-up synthesis of ZrO_2 NCs.....3

Figure 1.4. Schematic of the solution deposition methods for colloidal NCs. 5

Figure 1.5. NC devices including solar cells (A), light emitting diodes (B), photodetectors (C) and transistors (D).....6

Figure 1.6. Schematic comparing the process of traditional photolithography to the direct optical lithography of functional inorganic nanomaterials (DOLFIN). 8

Figure 2.1. Chemical structures of photosensitive compounds that enable NC patterning.....15

Figure 2.2. Numerical calculation of the electrostatic double layer interaction between NCs 19

Figure 2.3. Photodecomposition reactions of the photo-sensitive stabilizing ligands explored...20

Figure 2.4. NC patterns obtained using photo-sensitive stabilizing ligands 21

Figure 2.5. FTIR, ESI-MS and photodecomposition equation for ADC. 22

Figure 2.6. ESI-MS spectrums of *Bu*-DTC before DUV irradiation and photodecomposition equation for *Bu*-DTC.....23

Figure 2.7. Chemical analysis of PEX and $Cd(EX)_2$ and a proposed decomposition pathway....24

Figure 2.8. ESI-MS of MTT and its decomposition products. Below: proposed mechanism for photodecomposition. 25

Figure 2.9. ESI-MS, ^{13}C NMR, and FTIR spectra for TDD experiments and the proposed patterning mechanism. 27

Figure 2.10. Photodecomposition of additives for NC patterning. 28

Figure 2.11. NC patterns obtained by adding a photosensitive additive to NC solutions.....29

Figure 2.12. Patterning mechanisms that enable changes in NC solubility upon photodecomposition of the photosensitive ligand or additive. 30

Figure 3.1. Mechanism of conversion of 1-DNS and 2-DNS into SICA.[33] 42

Figure 3.2. Optical properties of the sensitizer and NCs. 43

Figure 3.3. The two methods of obtaining colloidal NPs in DMF involving either a solvent exchange or a ligand stripping procedure. 44

Figure 3.4. Size of the NPs and changes in zeta potential during the patterning process 45

Figure 3.5. Direct photolithography process of oxide nanoparticles with DNS. 46

Figure 3.6. FTIR spectra of ZrO_2-DNS films before irradiation, after irradiation, after development, and after annealing at 400 °C. 47

Figure 3.7. Electrospray ionization mass spectroscopy (ESI-MS) of 2-DNS in DMF before and after irradiation. 47

Figure 3.8. Calculated microscopic pK_a values of acidic protons of DNS-like compound (left) and SICA (right) in a solvent of DMF. 48

Figure 3.9. Patterns formed by mixing ZrO_2 NPs with two other photoacid generators in comparison with 2-DNS. 49

Figure 3.10. Control mechanism studies with pre-irradiated DNS (SICA) and benzene-1,4-dicarboxylic acid (BDA). 50

Figure 3.11. Optical microscope images of various oxide NPs optically patterned using DNS. .52

Figure 3.12. Powder XRD data of the synthesized ZrO_2, ITO and HfO_2 NCs. 52

Figure 3.13. DOLFIN patterning with 405 nm photons. 53

Figure 3.14. Resolution and thickness tests of single-layer amorphous ZrO_2 NPs patterns on silicon and glass substrates. 54

Figure 3.15. Multilayer direct patterning of oxide NPs. 56

Figure 3.16. Optical and surface roughness characterization of amorphous ZrO_2 NP–SICA films. 57

Figure 3.17. Powder XRD data of amorphous ZrO_2 NPs mixed with 2-DNS before and after annealing at 450 °C. 58

Figure 3.18. Measured and modeled data of a ZrO_2 film on a quartz substrate. 58

Figure 3.19. Fits of the spectroscopic ellipsometry data to a Tauc–Lorentz model for the oxide layer. 59

Figure 3.20. Characterization of diffraction gratings made by patterning amorphous ZrO_2 NPs.61

Figure 3.21. Patterning diffraction gratings made of CeO_2 NCs. 63

Figure 3.22. Pattering mixtures of NCs and NPs. 65

Figure 3.23. Plots of van der Waals interaction energy between two spheres. 67

Figure 3.24. (A) ^{31}P-NMR spectra of ZrO_2-TOPO NPs and HfO_2-TOPO NPs as synthesized. (B) ^{31}P-NMR spectra of ZrO_2-TOPO NPs after different surface treatment procedures. 68

Figure 4.1. Outline of the processing steps for direct photolithography of $CsPbX_3$ LHP NCs with the photosensitive oxime sulfonate ester. 80

Figure 4.2. Patterns of $CsPbBr_3$ NCs changes to their PLQY with various treatments. 82

Figure 4.3. PL lifetime of $CsPbBr_3$ NC films after different treatments compared to $CsPbBr_3$ OAc/OAm NCs. 83

Figure 4.4. Investigation of the $CsPbBr_3$ NCs and their ligands after each step of the DOLFIN patterning process. 85

Figure 4.5. Film absorption spectra of $CsPbBr_3$ NCs 86

Figure 4.6. Changes to the PLQY of $CsPbBr_3$ NC solutions.....86

Figure 4.7. Absorption spectra of a solution of PA-480 upon irradiation with 405 nm light. 87

Figure 4.8. Decomposition pathway of PA-480 in air. 87

Figure 4.9. FTIR spectra of a film of PA-480 before and after irradiation with 405 nm light.....89

Figure 4.10. Fitting of the (100) and (200) XRD peaks at each point of the patterning process with a multilayer diffraction fitting algorithm.....90

Figure 4.11. Transmission electron microscope images of $CsPbBr_3$ NCs at each point of the patterning process. 91

Figure 4.12. Optical microscope image of $CsPbBr_3$ NCs patterns using ILP-110N. 92

Figure 4.13. Modulating the emission color of NC films changing the halide composition.....93

Figure 4.14. PL shift after chloride exchange of a patterned $CsPbBr_3$ NC film.....94

Figure 4.15. Multiple pattern layers of LHP NCs.....95

Figure 4.16. PL and optical microscope images after one and two layers of LHP NC patterns without any intermediate layer. 95

Figure 4.17. Photoconductivity of patterned $CsPbBr_3$ NCs after treatment with trifluoroacetic acid/butylamine.....96

Figure 5.1. Schematic of the patterning process via surface photo-oxidation of bare NCs. 111

Figure 5.2. Optical microscope images showing patterns of ZnSe-BF_4 NCs obtained by photo-oxidation patterning. 112

Figure 5.3. Optical microscope images of patterns made of various NCs and counterions.....114

Figure 5.4. UV-vis spectra showing changes in the NC absorption spectra upon increasing light exposure.....115

Figure 5.5. UV-vis of oleate-capped NCs in toluene before and after irradiation.....116

Figure 5.6. Pictures and optical microscope images upon irradiation of ZnSe-BF_4 NCs in air or in air-free conditions. 116

Figure 5.7. Further investigation of the pattering mechanism via photo-oxidation.....118

Figure 5.8. Zeta potential measurements of ZnSe-BF_4 NCs upon various irradiation times with 405 nm light.....119

Figure 5.9. Tuning the porosity and refractive index of patterned ZnSe NC films. 121

Figure 5.10. XRD spectra before and after hot isostatic pressing treatment of ZnSe-BF_4 NCs.122

List of Tables

Table 3.1. Chemical structures of SICA and different DNQ variants investigated. 41

Acknowledgements

I would like to thank Prof. Dmitri Talapin for his guidance and support as my research advisor throughout my graduate studies. Dmitri has inspired me with his creativity and rigor in thinking and conducting scientific research. His insights into troubleshooting experimental issues were invaluable. I also learned how to construct an interesting and compelling research story from him. I would also like to thank my committee members, Prof. John Anderson and Prof. Greg Engel for their advice and time in reviewing my thesis.

My time in the lab has been greatly enriched by the many Talapin lab members which I have had the opportunity to collaborate and work with. Prof. Yuanyuan Wang and Dr. James Matt Kurley were very generous with their time in getting me started with projects. I have particularly benefited from fruitful conversations about optical patterning with Haoqi Wu, Prof. Himchan Cho, Dr. Igor Coropceanu, and Dr. Justin Ondry. I am also grateful for help and discussions with other current and former lab members including Josh Portner, Wooje Cho, Aritrajit Gupta, Di Wang, Dr. Chenkun Zhou, Zirui Zhou, Prof. Xinzheng Lan, Dr. Patrick Cunningham, Dr. Abhijit Hazarika, Dr. Vishwas Srivastava, Dr. Vlad Kamysbayev, Dr. Margaret Hudson, Dr. Eric Janke, Prof. Jong-Soo Lee, Zichao Rong, Anthony Gomez and Jason Lynch.

I am also greatly appreciative of the help from the University of Chicago staff including Tanya Shpigel, Dr. Vera Dragisich, Melinda Moore, Dr. Alexander Filatov, Dr. Justin Jureller, Dr. Peter Duda, Dr. Wook Jun Nam, Dr. Jin Qin, Dr. Qiti Guo, and Dr. Antoni Jurkiewicz. Their help with administration and instrumentation has enabled my research to proceed smoothly.

My time in Chicago has also been greatly enriched by the communities that I have been part of. To my Living Hope Church family including Brian Hempel, Tony Stevenson, the Beiers, Martin Putra, Avery Peck, Sam Hendley, Andrew Wang, the Franchuks, Sophia Zheng, the Rawls,

the Thoburns, the Wengers, the Grahams, Jackie Graves, Beza Desta, the Kochs, Marie Kim, Sarah Kwon, Chin Ying Wu, Elaine Tang, Ziyang Hao, Nathan Smith, Wayne Nobes, Elaine Kouame, the Kims, AJ Calhoun, the Andersons, Walker Haynes and Herbert Lin, you have been a spiritual and emotional support to me and a partner in living out God's love. I am also very grateful for my friends from the UChicago Graduate Christian Fellowship, including Susan Lee, Brian Hempel, Jair Pinedo, Jennifer Hu, Carolyn Zhang, the Hickernells, Kaleb Nyquist, Jarret Angbazo, Hannah Park, Joe Morrison, Allen Zhu, Venezah St Louis, Lyndon Zhang, Alex Lee, and Jasmine Tan.

Finally, I would like to thank my family who have always been there for me whether close-by or halfway around the globe. My mum and dad have always encouraged my development as a scientist and as a person. Our weekly virtual family chats have always grounded me to things that really matter. To my beloved wife, Cheng Yin Eng, you have been my rock throughout my studies. Thank you for your listening ear and encouraging words that have kept me going throughout these years.

Abstract

This thesis focuses on the development of chemical approaches for direct optical patterning of colloidal nanomaterials. In Chapter 1, we introduce colloidal nanomaterials and their device applications. We then discuss the need for new methods to pattern nanomaterials which motivate the development of direct optical lithography of functional inorganic nanomaterials (DOLFIN).

Chapter 2 discusses the establishment of a library of photosensitive ligands and additives for DOLFIN. We demonstrate the use of these photosensitizers to pattern a variety of NCs and study their photodecomposition pathways and products. We also discuss the various chemical mechanisms that enable the solubility of NCs to be modulated by the decomposition of the photosensitizers.

In Chapter 3, we directly optically pattern oxide nanoparticles (NPs) by mixing them with photosensitive diazo-2-naphthol-4-sulfonic acid and irradiating with widely available 405 nm light. We demonstrate the direct optical lithography of ZrO_2, TiO_2, HfO_2, and ITO NPs and investigate the chemical and physical changes responsible for this photoinduced decrease in solubility. Micron-thick layers of amorphous ZrO_2 NPs were patterned with micron resolution and shown to allow 2π phase control of visible light. We also show multilayer patterning and use it to fabricate features with different thicknesses and distinct structural colors. Upon annealing at 400 °C, the deposited structures have excellent optical transparency across a wide wavelength range ($0.3 - 10\ \mu$m), a high refractive index ($n = 1.84$ at 633 nm) and are optically smooth. We then fabricate diffractive optical elements, such as binary phase diffraction gratings, that show efficient diffractive behavior and good thermal stability. Different oxide NPs can also be mixed prior to patterning, providing a high level of material tunability.

Chapter 4 involves the direct photo-patterning approach for lead halide perovskite (LHP) NCs through the binding and subsequent cleavage of a photosensitive oxime sulfonate ester. The photosensitizer binds to the NCs through its sulfonate group and is cleaved at the N–O bond during photo-irradiation with 405 nm light. This bond cleavage decreases the solubility of the NCs which allows patterns to emerge upon development with toluene. Post-patterning ligand exchange results in photoluminescence quantum yields up to 76%, while anion exchange provides tunability in the emission wavelength. The patterned NC films show photoconductive behavior, demonstrating that good electrical contact between the NCs can be established.

In Chapter 5, we introduce the direct optical patterning of bare NCs that does not require any additional photosensitive ligands or additives. We determined that photo-exposure of ligand-stripped, bare NCs in air significantly reduces their solubility in polar solvents due to photo-oxidation of surface ions. This approach enabled the patterning of bare ZnSe, CdSe, ZnS, InP, CeO_2 NCs as well as mixtures of ZnSe with ZrO_2, HfO_2, or CdSe/ZnS NCs. The photo-oxidation process was studied by various methods including UV-vis and X-ray photoelectron spectroscopy. We also demonstrate porosity and refractive index modulation of patterned NC films. This allowed the refractive index of the ZnSe NC film to be modulated between $n = 1.87$ and $n = 2.10$. Our findings showcase an easily accessible patterning method for bare NCs.

Chapter 1. Introduction

1.1. Introduction to colloidal nanomaterials

Colloidal nanomaterials are inorganic particles with sizes about 1–200 nm that are well-dispersed in a solvent. This includes colloidal nanocrystals (NCs), quantum dots (QDs), colloidal nanoplatelets, and amorphous nanoparticles. In the last few decades, colloidal nanomaterials have been investigated intensively in terms of their syntheses, fundamental properties, and device applications.[1-4] A large, diverse library of colloidal nanomaterials has been established with tunability in composition, size and shape (**Figure 1.1**). For instance, NCs can be made metallic, semiconducting, insulating, or magnetic based on their composition (**Figure 1.1A–D**). Synthetic advances have also allowed multi-component NCs to be fabricated (**Figure 1.1E**), allowing for increasing compositional complexity.

The size of colloidal NCs can also be tuned and is particularly striking for semiconducting NCs, also known as quantum dots (QDs). When the radius of a semiconducting NC is smaller than its exciton Bohr radius, quantum confinement effects lead to the widening of the bandgap as the NC size is decreased, which enables the emission wavelength of the NCs to be tuned (**Figure 1.1F–G**). The color tunability of these QDs, their high photoluminescence quantum yields (PLQY), and narrow emission linewidths have led to the implementation of QDs in various optoelectronic applications. Furthermore, NCs with various shapes can also be synthesized through anisotropic growth control of the NCs. For example, depending on the synthetic conditions, gold NCs can be synthesized in the shape of rods, cubes, octahedrons and tetrahedrons (**Figure 1.1H–K**). This has enabled the enhancement of plasmonic properties via the geometric concentration of electric fields.

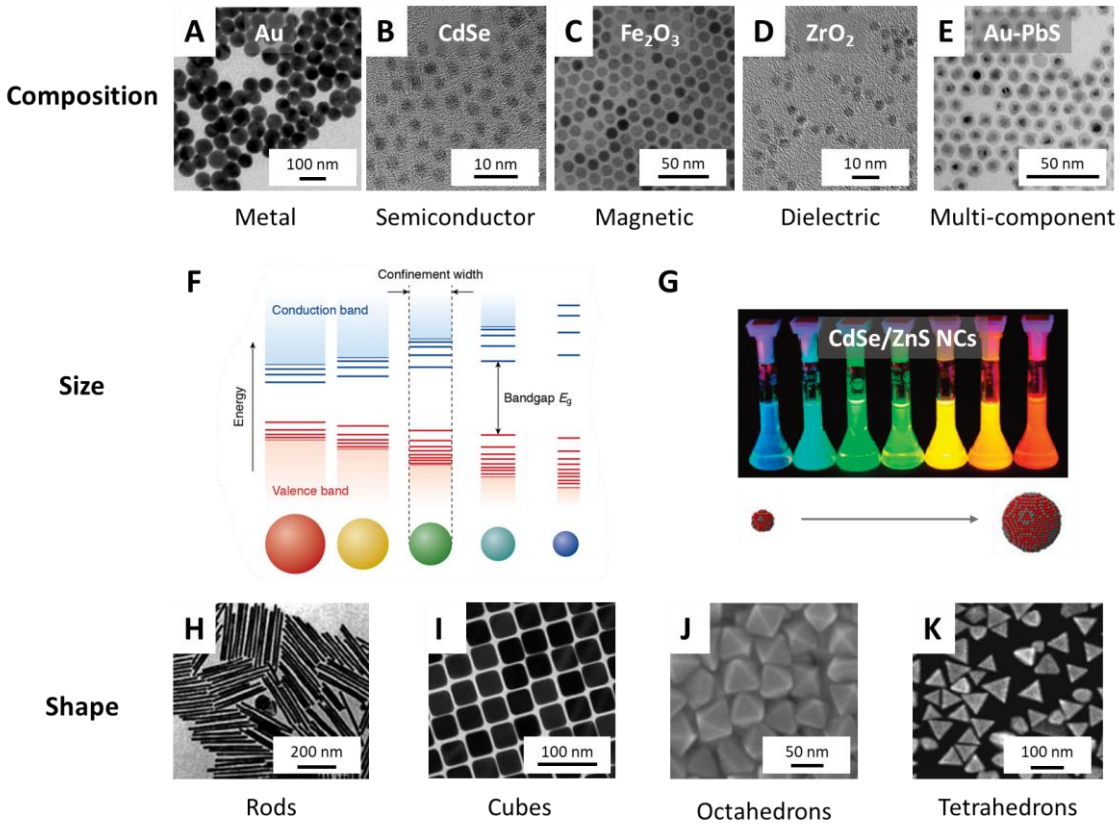

Figure 1.1. The diversity of colloidal nanocrystals (NCs) in composition, size, and shape. (A–E) Gold (A), CdSe (B), Fe_2O_3 (C), ZrO_2 (D), and Au-PbS (E) NCs. (F) Schematic of quantum confinement effect in semiconducting NCs. (G) Luminescent CdSe/ZnS core-shell NCs with different core sizes. (H–K) Gold NCs with different shapes such rods (H), cubes (I), octahedrons (J) and tetrahedrons (K). (A) Adapted with permission from ref. 5. Copyright 2004 American Chemical Society. (B) Adapted with permission from ref. 6. Copyright 2013 American Chemical Society. (C) Adapted with permission from ref. 7. Copyright 2001 American Chemical Society. (E) Adapted with permission from ref. 8. Copyright 2008 American Chemical Society. (F) Adapted with permission from ref. 3. Copyright 2016 Springer. (G) Adapted with permission from ref. 9. Copyright 2002 Wiley. (H) Adapted with permission from ref. 10. Copyright 2001 American Chemical Society. (I) Adapted with permission from ref. 11. Copyright 2018 American Chemical Society. (J) Adapted with permission from ref. 12. Copyright 2007 Wiley. (K) Adapted with permission from ref. 13. Copyright 2008 American Chemical Society.

Many synthetic approaches for colloidal nanomaterials have been developed. A popular and well-developed approach involves the high-temperature synthesis of NCs in organic solvents in the presence of long-chain organic surfactants.[14] For example, ZnSe NCs can be synthesized

through the hot injection of a Se suspension into a solution of zinc oleate (**Figure 1.2**). Alternatively, a heat-up synthesis may also be used. For instance, heating-up $ZrCl_4$ and Zr isopropoxide in trioctylphosphine oxide to a temperature of 340 °C leads to the formation of tetragonal-phase ZrO_2 NCs (**Figure 1.3**). These high-temperatures synthesis in a coordinating solvent has the advantages of high monodispersity and good crystallinity.

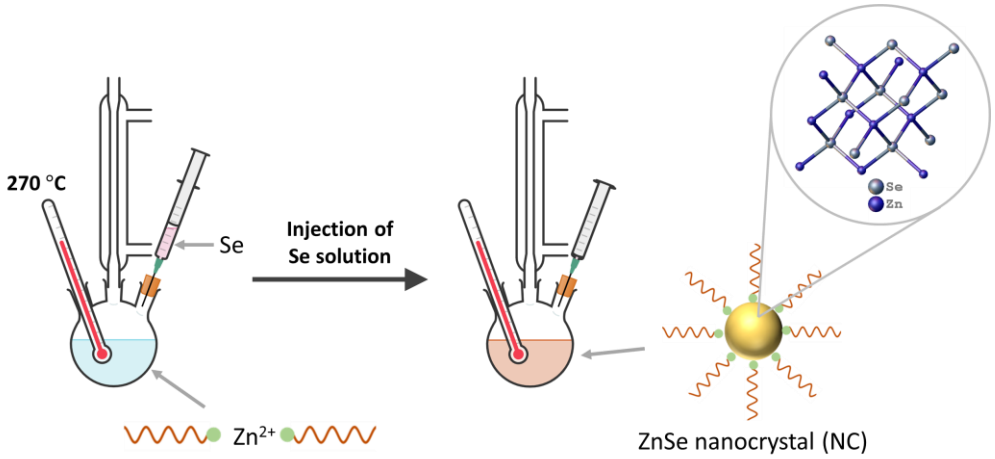

Figure 1.2. Schematic of the hot-injection synthesis of ZnSe NCs with conditions from ref. [6].

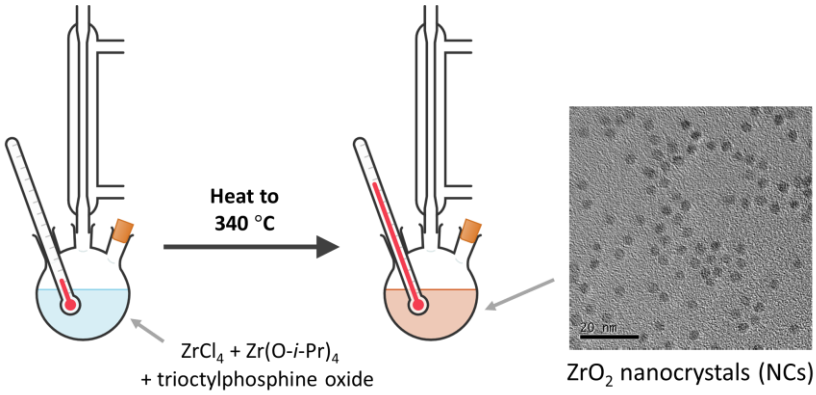

Figure 1.3. Schematic of the heat-up synthesis of ZrO_2 NCs with conditions from ref. [15].

Another common approach for the synthesis of colloidal metal oxide nanoparticles (NPs) is the so-called "sol-gel" approach.[16] This method typically involves the hydrolysis and condensation of a metal precursor in an aqueous media. If the condensation reaction is stopped when the NPs (also called "sols") are at an appropriate nanometer size (before any gelation occurs), we can obtain NPs that are well-stabilized in the solution. Although this approach is simple and very scalable, its disadvantages include poor crystallinity and large polydispersity.

Besides the bottom-up synthesis that have been discussed so far, colloidal nanomaterials can also be obtained through top-down approaches that utilize bulk materials as the starting point. For instance, two-dimensional colloidal nanosheets can be obtained through the exfoliation of layered bulk materials.[17-19] This approach further extends the library of colloidal nanomaterials to compositions that are difficult to synthesize via solution-based chemistry. However, some downsides to these exfoliated nanomaterials are their large lateral polydispersity and limited surface chemistry.

1.2. Devices from colloidal nanomaterials

One of the conveniences of colloidal nanomaterials is its solution-processibility. This allows the NCs to be easily purified and characterized by common solution-handling techniques. To further utilize NCs and to integrate them with other components, it is necessary to deposit them as a thin film, which can be done through deposition methods such as dip-coating, drop-casting, ink-jet printing, spin-coating, spray-coating, and blade-coating (**Figure 1.4**). Compared to vapor-phase deposition approaches, these solution-deposition techniques have a low cost, are highly scalable, and have higher throughputs. For instance, it is quite straight-forward to deposit NCs on large multi-feet substrates by blade-coating, whereas it is a non-trivial problem for vapor

deposition due to requirements of vacuum and other issues. Also, NCs can be deposited on virtually any type of substrate regardless of material and form-factor, whereas vapor-phase deposition methods are often limited to epitaxially-matched, flat substrates. On the other hand, vapor-phase deposition techniques are often superior in their atomic precision, robustness, and material performance. Thus, the goal of developing solution-processible NCs is not to supplant these more established material fabrication approaches, but to provide a complementary materials platform.

Figure 1.4. Schematic of the solution deposition methods for colloidal NCs.

By solution-deposition techniques, various NC devices have been fabricated and demonstrated including solar cells, photodetectors, transistors, light-emitting diodes (LED), lasers, gas sensors, photonic devices, and color-conversion layers (**Figure 1.5**). [1, 20-22] These NC devices have been developed and optimized over the last several decades to the point where they are already commercially viable for certain applications such as in display technologies.

For devices that require charge transport between the NCs, the insulating long-chain organic ligands need to be removed or replaced.[1] A well-explored route to do this is via a solution-

phase inorganic ligand exchange which involves the replacement of the surface organic ligands with charge-stabilized moieties that provide colloidal stabilization via electrostatic repulsion.[23] This includes the binding of metal chalcogenide complexes,[24] chalcogenides,[25] halides,[26] oxoanions,[27] and halometalates.[28] These ions bind strongly to the surface of the NC and typically lead to a negatively-charged NC surface when dissolved in a polar solvent like NMF or DMF. Alternatively, the replacement of the organic ligands with a highly non-coordinating anion like BF_4^- can also provide electrostatic colloidal stability due to the positive charging of the "bare" NC surface. [29-32]

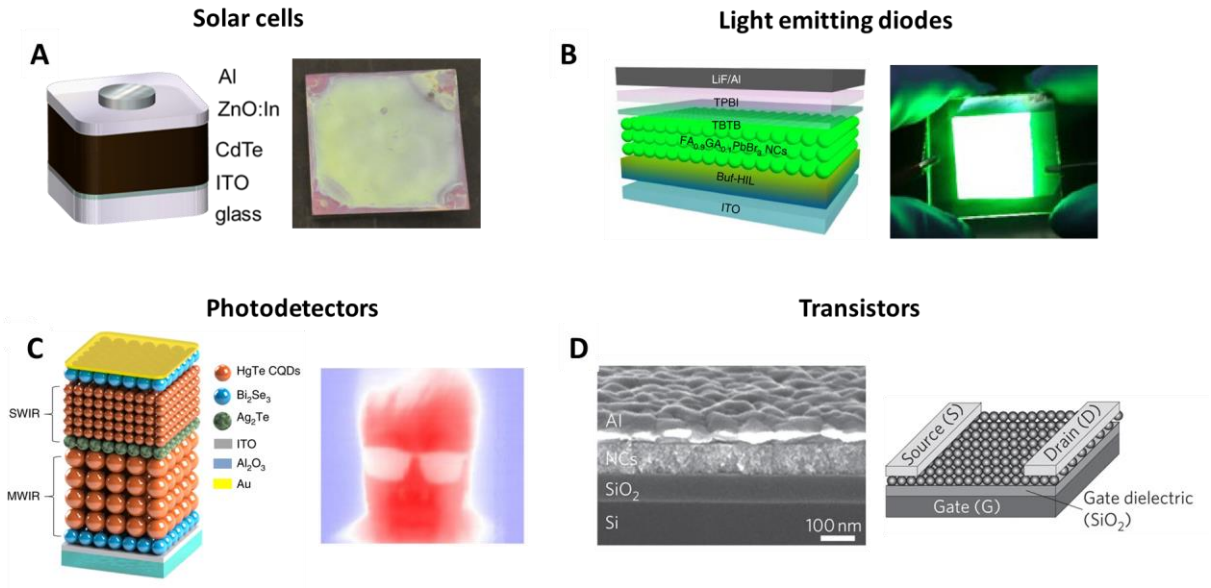

Figure 1.5. NC devices including solar cells (A), light emitting diodes (B), photodetectors (C) and transistors (D). (B) Adapted with permission from ref. [33]. Copyright 2021 Springer. (C) Adapted with permission from ref. [34]. Copyright 2019 Springer. (D) Adapted with permission from ref. [35]. Copyright 2011 Springer.

1.3. Direct optical patterning of functional inorganic nanomaterials (DOLFIN)

Although the use of NCs for various device applications has been clearly demonstrated, there still are challenges that limit the functionality and integration of NCs in real-world devices. One issue involves the difficulty in precisely depositing two-dimensional patterns of NCs. This patterning capability is crucial for the formation of more complex arrays of structures (e.g., LED arrays with red, green, and blue pixels), and for proper integration with other parts of a device (e.g., electrodes, interconnects, *etc.*).

Many routes to patterning colloidal NCs have been developed including ink-jet printing,[36-37] transfer printing,[38] nanoimprinting,[39] two-photon lithography,[40] direct ink writing,[41] extreme-UV lithography,[42] and photolithography.[43] The use of photolithography to pattern NCs is particularly attractive due its scalability, parallel processing, good resolution, widespread availability of light exposure tools.[44] In the standard photolithography process, a polymer photoresist is used as a sacrificial layer (**Figure 1.6**, left). This light-sensitive resist undergoes a solubility change upon light exposure which allows patterns to be formed upon development. Subsequently, a material is deposited on top of these polymer patterns (additive process), or an etching step is used to remove the underlying material (subtractive process). The stripping of the photoresist then leaves behind a patterned layer of the material of interest.

As one of the key underlying processes of modern device fabrication, the sacrificial photolithography process has been highly optimized to yield high-quality micro- and nano-scale patterns. This approach works well for vapor-phase deposition techniques since the vapor-to-solid transformation does not allow for any lateral movement during the deposition. This leads to the uniform deposition of material on the regions in between the photoresist. In contrast, the solution-phase deposition of a material onto a patterned polymer layer often leads to non-uniform

deposition due to capillary effects as the solvent evaporates. Furthermore, the sensitive nature of many colloidal nanomaterials often leads to their degradation during the photoresist development or stripping step.

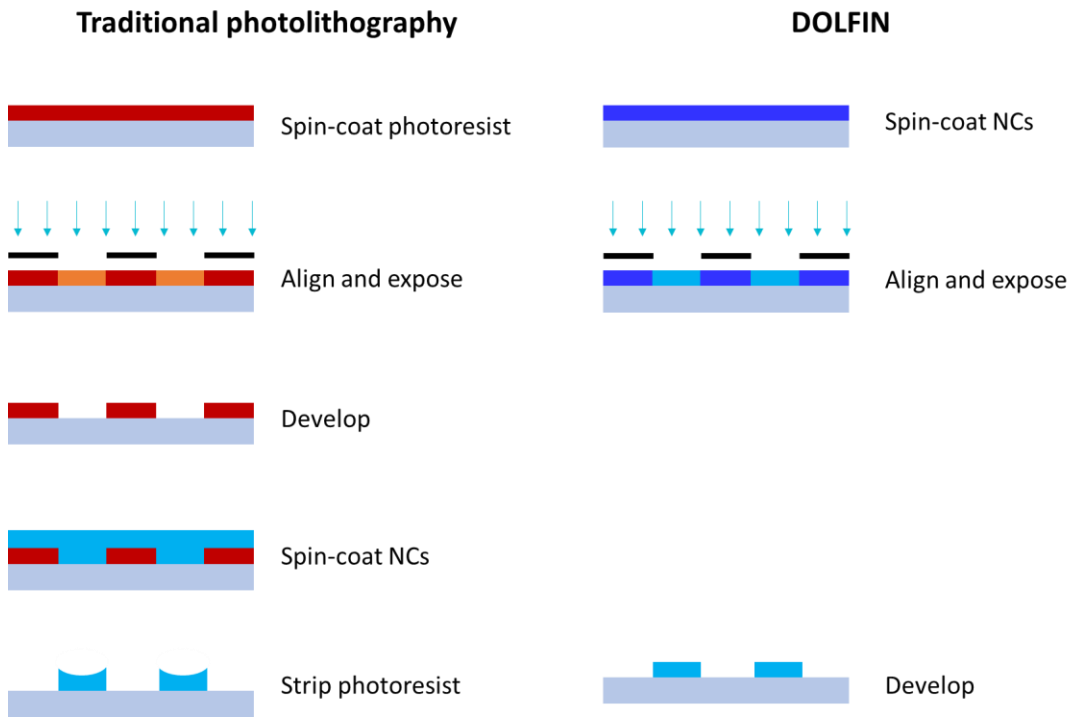

Figure 1.6. Schematic comparing the process of traditional photolithography to the direct optical lithography of functional inorganic nanomaterials (DOLFIN).

Due to the limitations of using traditional photolithography for solution-processed materials, we in the Talapin lab have been developing the direct optical lithography of functional inorganic nanomaterials (DOLFIN). In the DOLFIN process, we avoid the limitations of traditional photolithography processing by using a photo-patternable NC ink (**Figure 1.6**, right). In this process, the photosensitive NC ink is deposited as a thin film and directly exposed to light through a mask. The light-exposure triggers a photo-chemical reaction in the NC film which changes the solubility of the NCs in a developer solvent, leading to the formation of two-dimensional patterns.

It is important to note that there have been other chemical approaches that have been used for the direct patterning of NCs.[43, 45-50] These approaches have shown that high-quality micro-scale patterns of NCs can be obtained by direct optical patterning. However, the DOLFIN approach differs from these works on a few important features. First, our method places an emphasis on minimizing the amount of organic residue in the NC film after the patterning process. This enables the high packing fraction of NCs in the patterned film as well as the ability for electronic communication between NCs. Besides that, the DOLFIN approach aims establish a modular and general patterning approach in which the photosensitive ligands or additives can be compatible with a wide range of colloidal nanomaterials.

In the next few chapters, I will discuss the development of a library of approaches to fabricate high-quality NC patterns and demonstrate their use in photonic and optoelectronic devices.

1.4. Chapter bibliography

1. Talapin, D. V.; Lee, J.-S.; Kovalenko, M. V.; Shevchenko, E. V., Prospects of Colloidal Nanocrystals for Electronic and Optoelectronic Applications. *Chem. Rev.* **2010,** *110* (1), 389-458.

2. Park, J.; Joo, J.; Kwon, S. G.; Jang, Y.; Hyeon, T., Synthesis of Monodisperse Spherical Nanocrystals. *Angew. Chem. Int. Ed.* **2007,** *46* (25), 4630-4660.

3. Rabouw, F. T.; de Mello Donega, C., Excited-State Dynamics in Colloidal Semiconductor Nanocrystals. *Top. Curr. Chem.* **2016,** *374* (5), 58.

4. Xia, Y.; Xiong, Y.; Lim, B.; Skrabalak, S. E., Shape-Controlled Synthesis of Metal Nanocrystals: Simple Chemistry Meets Complex Physics? *Angew. Chem. Int. Ed.* **2009,** *48* (1), 60-103.

5. Hiramatsu, H.; Osterloh, F. E., A Simple Large-Scale Synthesis of Nearly Monodisperse Gold and Silver Nanoparticles with Adjustable Sizes and with Exchangeable Surfactants. *Chem. Mater.* **2004,** *16* (13), 2509-2511.

6. Flamee, S.; Cirillo, M.; Abe, S.; De Nolf, K.; Gomes, R.; Aubert, T.; Hens, Z., Fast, High Yield, and High Solid Loading Synthesis of Metal Selenide Nanocrystals. *Chem. Mater.* **2013,** *25* (12), 2476-2483.

7. Hyeon, T.; Lee, S. S.; Park, J.; Chung, Y.; Na, H. B., Synthesis of Highly Crystalline and Monodisperse Maghemite Nanocrystallites without a Size-Selection Process. *J. Am. Chem. Soc.* **2001,** *123* (51), 12798-12801.

8. Lee, J.-S.; Shevchenko, E. V.; Talapin, D. V., Au−PbS Core−Shell Nanocrystals: Plasmonic Absorption Enhancement and Electrical Doping via Intra-particle Charge Transfer. *J. Am. Chem. Soc.* **2008,** *130* (30), 9673-9675.

9. Rogach, A. L.; Talapin, D. V.; Shevchenko, E. V.; Kornowski, A.; Haase, M.; Weller, H., Organization of Matter on Different Size Scales: Monodisperse Nanocrystals and Their Superstructures. *Adv. Funct. Mater.* **2002,** *12* (10), 653-664.

10. Jana, N. R.; Gearheart, L.; Murphy, C. J., Wet Chemical Synthesis of High Aspect Ratio Cylindrical Gold Nanorods. *The Journal of Physical Chemistry B* **2001,** *105* (19), 4065-4067.

11. Park, J.-E.; Lee, Y.; Nam, J.-M., Precisely Shaped, Uniformly Formed Gold Nanocubes with Ultrahigh Reproducibility in Single-Particle Scattering and Surface-Enhanced Raman Scattering. *Nano Lett.* **2018,** *18* (10), 6475-6482.

12. Li, C.; Shuford, K. L.; Park, Q. H.; Cai, W.; Li, Y.; Lee, E. J.; Cho, S. O., High-Yield Synthesis of Single-Crystalline Gold Nano-octahedra. *Angew. Chem. Int. Ed.* **2007,** *46* (18), 3264-3268.

13. Seo, D.; Yoo, C. I.; Chung, I. S.; Park, S. M.; Ryu, S.; Song, H., Shape Adjustment between Multiply Twinned and Single-Crystalline Polyhedral Gold Nanocrystals: Decahedra, Icosahedra, and Truncated Tetrahedra. *The Journal of Physical Chemistry C* **2008,** *112* (7), 2469-2475.

14. Murray, C. B.; Norris, D. J.; Bawendi, M. G., Synthesis and characterization of nearly monodisperse CdE (E = sulfur, selenium, tellurium) semiconductor nanocrystallites. *J. Am. Chem. Soc.* **1993,** *115* (19), 8706-8715.

15. Joo, J.; Yu, T.; Kim, Y. W.; Park, H. M.; Wu, F.; Zhang, J. Z.; Hyeon, T., Multigram scale synthesis and characterization of monodisperse tetragonal zirconia nanocrystals. *J. Am. Chem. Soc.* **2003,** *125* (21), 6553-6557.

16. Hench, L. L.; West, J. K., The sol-gel process. *Chem. Rev.* **1990,** *90* (1), 33-72.

17. Naguib, M.; Kurtoglu, M.; Presser, V.; Lu, J.; Niu, J.; Heon, M.; Hultman, L.; Gogotsi, Y.; Barsoum, M. W., Two-Dimensional Nanocrystals Produced by Exfoliation of Ti3AlC2. *Adv. Mater.* **2011,** *23* (37), 4248-4253.

18. Kang, J.; Sangwan, V. K.; Wood, J. D.; Hersam, M. C., Solution-based processing of monodisperse two-dimensional nanomaterials. *Acc. Chem. Res.* **2017,** *50* (4), 943-951.

19. Grayfer, E. D.; Kozlova, M. N.; Fedorov, V. E., Colloidal 2D nanosheets of MoS2 and other transition metal dichalcogenides through liquid-phase exfoliation. *Adv. Colloid Interface Sci.* **2017,** *245*, 40-61.

20. Arquer, F. P. G. d.; Talapin, D. V.; Klimov, V. I.; Arakawa, Y.; Bayer, M.; Sargent, E. H., Semiconductor quantum dots: Technological progress and future challenges. *Science* **2021,** *373* (6555), eaaz8541.

21. Kagan, C. R.; Lifshitz, E.; Sargent, E. H.; Talapin, D. V., Building devices from colloidal quantum dots. *Science* **2016,** *353* (6302), aac5523.

22. Kovalenko, M. V.; Manna, L.; Cabot, A.; Hens, Z.; Talapin, D. V.; Kagan, C. R.; Klimov, V. I.; Rogach, A. L.; Reiss, P.; Milliron, D. J.; Guyot-Sionnnest, P.; Konstantatos, G.; Parak, W. J.; Hyeon, T.; Korgel, B. A.; Murray, C. B.; Heiss, W., Prospects of Nanoscience with Nanocrystals. *ACS Nano* **2015,** *9* (2), 1012-1057.

23. Wang, W.; Zhang, M.; Pan, Z.; Biesold, G. M.; Liang, S.; Rao, H.; Lin, Z.; Zhong, X., Colloidal Inorganic Ligand-Capped Nanocrystals: Fundamentals, Status, and Insights into Advanced Functional Nanodevices. *Chem. Rev.* **2021**.

24. Kovalenko, M. V.; Scheele, M.; Talapin, D. V., Colloidal Nanocrystals with Molecular Metal Chalcogenide Surface Ligands. *Science* **2009,** *324* (5933), 1417.

25. Nag, A.; Kovalenko, M. V.; Lee, J.-S.; Liu, W.; Spokoyny, B.; Talapin, D. V., Metal-free inorganic ligands for colloidal nanocrystals: S2–, HS–, Se2–, HSe–, Te2–, HTe–, TeS32–, OH–, and NH2–as surface ligands. *J. Am. Chem. Soc.* **2011,** *133* (27), 10612-10620.

26. Zhang, H.; Jang, J.; Liu, W.; Talapin, D. V., Colloidal nanocrystals with inorganic halide, pseudohalide, and halometallate ligands. *ACS Nano* **2014,** *8* (7), 7359-7369.

27. Huang, J.; Liu, W.; Dolzhnikov, D. S.; Protesescu, L.; Kovalenko, M. V.; Koo, B.; Chattopadhyay, S.; Shenchenko, E. V.; Talapin, D. V., Surface functionalization of semiconductor and oxide nanocrystals with small inorganic oxoanions (PO43–, MoO42–) and polyoxometalate ligands. *ACS Nano* **2014,** *8* (9), 9388-9402.

28. Dirin, D. N.; Dreyfuss, S. b.; Bodnarchuk, M. I.; Nedelcu, G.; Papagiorgis, P.; Itskos, G.; Kovalenko, M. V., Lead halide perovskites and other metal halide complexes as inorganic capping ligands for colloidal nanocrystals. *J. Am. Chem. Soc.* **2014,** *136* (18), 6550-6553.

29. Dong, A.; Ye, X.; Chen, J.; Kang, Y.; Gordon, T.; Kikkawa, J. M.; Murray, C. B., A generalized ligand-exchange strategy enabling sequential surface functionalization of colloidal nanocrystals. *J. Am. Chem. Soc.* **2010,** *133* (4), 998-1006.

30. Rosen, E. L.; Buonsanti, R.; Llordes, A.; Sawvel, A. M.; Milliron, D. J.; Helms, B. A., Exceptionally mild reactive stripping of native ligands from nanocrystal surfaces by using Meerwein's salt. *Angew. Chem. Int. Ed.* **2012,** *51* (3), 684-689.

31. Doris, S. E.; Lynch, J. J.; Li, C.; Wills, A. W.; Urban, J. J.; Helms, B. A., Mechanistic insight into the formation of cationic naked nanocrystals generated under equilibrium control. *J. Am. Chem. Soc.* **2014,** *136* (44), 15702-15710.

32. Wang, W.; Pan, Z.; Rao, H.; Zhang, G.; Song, H.; Zhang, Z.; Zhong, X., Proton Initiated Ligand Exchange Reactions for Colloidal Nanocrystals Functionalized by Inorganic Ligands with Extremely Weak Coordination Ability. *Chem. Mater.* **2019**.

33. Kim, Y.-H.; Kim, S.; Kakekhani, A.; Park, J.; Park, J.; Lee, Y.-H.; Xu, H.; Nagane, S.; Wexler, R. B.; Kim, D.-H.; Jo, S. H.; Martínez-Sarti, L.; Tan, P.; Sadhanala, A.; Park, G.-S.; Kim, Y.-W.; Hu, B.; Bolink, H. J.; Yoo, S.; Friend, R. H.; Rappe, A. M.; Lee, T.-W., Comprehensive defect suppression in perovskite nanocrystals for high-efficiency light-emitting diodes. *Nat. Photonics* **2021,** *15* (2), 148-155.

34. Tang, X.; Ackerman, M. M.; Chen, M.; Guyot-Sionnest, P., Dual-band infrared imaging using stacked colloidal quantum dot photodiodes. *Nat. Photonics* **2019,** *13* (4), 277-282.

35. Lee, J.-S.; Kovalenko, M. V.; Huang, J.; Chung, D. S.; Talapin, D. V., Band-like transport, high electron mobility and high photoconductivity in all-inorganic nanocrystal arrays. *Nat. Nanotechnol.* **2011,** *6* (6), 348-352.

36. Haverinen, H. M.; Myllyla, R. A.; Jabbour, G. E., Inkjet Printed RGB Quantum Dot-Hybrid LED. *Journal of Display Technology* **2010,** *6* (3), 87-89.

37. Zhang, L.; Chao, D.; Yang, P.; Weber, L.; Li, J.; Kraus, T.; Fan, H. J., Flexible Pseudocapacitive Electrochromics via Inkjet Printing of Additive-Free Tungsten Oxide Nanocrystal Ink. *Advanced Energy Materials* **2020,** *10* (17), 2000142.

38. Kim, T.-H.; Cho, K.-S.; Lee, E. K.; Lee, S. J.; Chae, J.; Kim, J. W.; Kim, D. H.; Kwon, J.-Y.; Amaratunga, G.; Lee, S. Y., Full-colour quantum dot displays fabricated by transfer printing. *Nat. Photonics* **2011,** *5* (3), 176.

39. Beaulieu, M. R.; Hendricks, N. R.; Watkins, J. J., Large-area printing of optical gratings and 3D photonic crystals using solution-processable nanoparticle/polymer composites. *ACS Photonics* **2014,** *1* (9), 799-805.

40. Krini, R.; Ha, C. W.; Prabhakaran, P.; Mard, H. E.; Yang, D.-Y.; Zentel, R.; Lee, K.-S., Photosensitive Functionalized Surface-Modified Quantum Dots for Polymeric Structures via Two-Photon-Initiated Polymerization Technique. *Macromol. Rapid Commun.* **2015,** *36* (11), 1108-1114.

41. Li, Q.; Lewis, J. A., Nanoparticle Inks for Directed Assembly of Three-Dimensional Periodic Structures. *Adv. Mater.* **2003,** *15* (19), 1639-1643.

42. Miszta, K.; Greullet, F.; Marras, S.; Prato, M.; Toma, A.; Arciniegas, M.; Manna, L.; Krahne, R., Nanocrystal Film Patterning by Inhibiting Cation Exchange via Electron-Beam or X-ray Lithography. *Nano Lett.* **2014,** *14* (4), 2116-2122.

43. Jun, S.; Jang, E.; Park, J.; Kim, J., Photopatterned semiconductor nanocrystals and their electroluminescence from hybrid light-emitting devices. *Langmuir* **2006,** *22* (6), 2407-2410.

44. Mack, C., *Fundamental principles of optical lithography: the science of microfabrication*. John Wiley & Sons: 2008.

45. Qualtieri, A.; Martiradonna, L.; Stomeo, T.; Todaro, M. T.; Cingolani, R.; Vittorio, M. D., Multicolored devices fabricated by direct lithography of colloidal nanocrystals. *Microelectron. Eng.* **2009,** *86* (4), 1127-1130.

46. Kim, W. J.; Kim, S. J.; Lee, K.-S.; Samoc, M.; Cartwright, A. N.; Prasad, P. N., Robust microstructures using UV photopatternable semiconductor nanocrystals. *Nano Lett.* **2008,** *8* (10), 3262-3265.

47. Minh, D. N.; Eom, S.; Nguyen, L. A. T.; Kim, J.; Sim, J. H.; Seo, C.; Nam, J.; Lee, S.; Suk, S.; Kim, J., Perovskite Nanoparticle Composite Films by Size Exclusion Lithography. *Adv. Mater.* **2018,** *30* (39), 1802555.

48. Hahm, D.; Park, J.; Jeong, I.; Rhee, S.; Lee, T.; Lee, C.; Chung, S.; Bae, W. K.; Lee, S., Surface Engineered Colloidal Quantum Dots for Complete Green Process. *ACS Appl. Mater. Interfaces* **2020,** *12* (9), 10563-10570.

49. Yang, J.; Hahm, D.; Kim, K.; Rhee, S.; Lee, M.; Kim, S.; Chang, J. H.; Park, H. W.; Lim, J.; Lee, M.; Kim, H.; Bang, J.; Ahn, H.; Cho, J. H.; Kwak, J.; Kim, B.; Lee, C.; Bae, W. K.; Kang, M. S., High-resolution patterning of colloidal quantum dots via non-destructive, light-driven ligand crosslinking. *Nat. Commun.* **2020,** *11* (1), 2874.

50. Kim, J.; Kwon, S.-M.; Kang, Y. K.; Kim, Y.-H.; Lee, M.-J.; Han, K.; Facchetti, A.; Kim, M.-G.; Park, S. K., A skin-like two-dimensionally pixelized full-color quantum dot photodetector. *Science Advances* **2019,** *5* (11), eaax8801.

Chapter 2. Photosensitive ligands and additives for solubility modulation of colloidal nanomaterials

Adapted with permission from Y. Wang, J.-A. Pan *et al. ACS Nano*, **2019**, *13*, 12, 13917-13931. Copyright 2019 American Chemical Society.

2.1. Selection of photosensitive ligands and additives for patterning nanomaterials

Direct optical patterning of nanomaterials requires designing photo-induced chemical reactions that affect their colloidal stability. This can be achieved by introducing a photosensitive component into the NC ink in the form of either a stabilizing photosensitive ligand or a photosensitive additive (**Figure 2.1**).

The first approach relies on development of small-molecule surface ligands that provide colloidal stability to the NCs but also chemically transform upon exposure to optical excitation with certain photon energy. Ideally, such ligands should leave no insoluble organic residue after photo exposure, which enables the formation of all-inorganic patterns of functional nanomaterials. The all-inorganic design is motivated by numerous studies showing utility of NCs capped with compact, inorganic surface ligands for various thin-film devices and other applications.[1-6]

The second approach to create DOLFIN inks utilizes two different molecular species to separately fulfill the above requirements: one component stabilizes the NC colloids while the second component acts as a photochemically active additive that alters NC solubility upon irradiation. Compared with the first type of ink, this approach can offer additional flexibility. By changing the combination of two components, we can prepare various inks to satisfy special needs in term of exposure wavelength, developing solvents, *etc*.

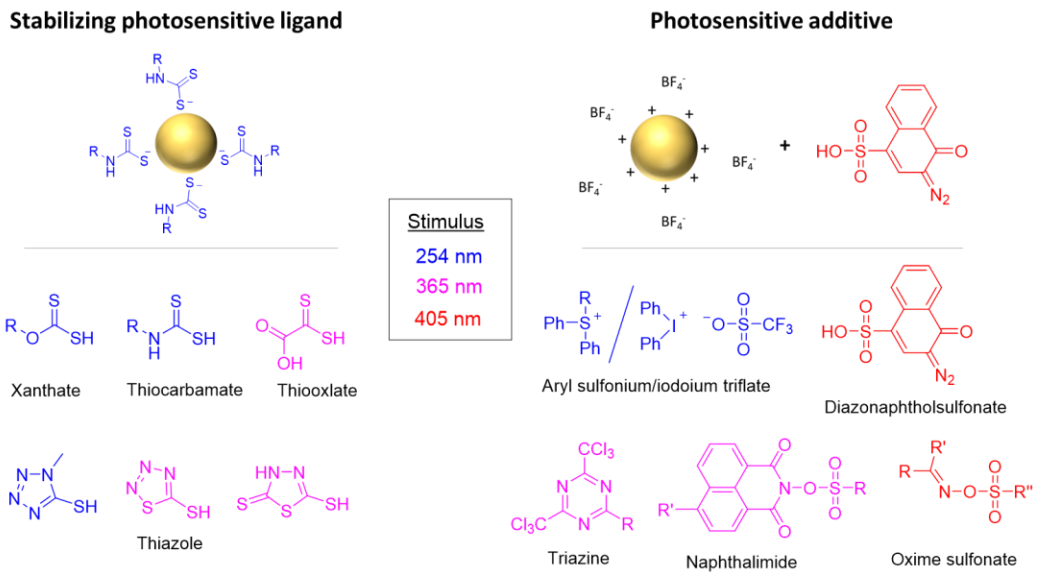

Figure 2.1. Chemical structures of photosensitive compounds that enable NC patterning. The compounds can be categorized as either (1) photosensitive ligands that also provide colloidal stability or (2) photosensitive additives that are added to pre-stabilized NCs.

2.2. Interaction forces between colloidal NCs

To understand how the solubility of NCs can be modulated in the DOLFIN process, we need to first understand the fundamental interaction forces present in a NC solution. This is because the NC patterning process takes advantage of photo-induced chemical changes that reduce or increase the strength of these interactions. There are three main types of colloidal NC interactions: Van der Waals forces, steric interactions, and electrostatic double layer repulsion.

2.2.1. Van der Waals interactions

The Van der Waals dispersion force is a ubiquitous force between all atoms and molecules due to the interaction of instantaneous dipoles that arise from the distortion of the electron cloud within the atom or molecule. For larger objects like NCs, we can estimate the van der Waals interaction using the Hamaker approach, which assumes that the forces are pairwise additive and is not retarded by the solvent between the NCs.[7-9] With this approach, we can express the van der

Waals interaction energy, U_{VdW} between two identical NCs of radius, a, and NC surface separation, d, as

$$U_{VdW} = -\frac{A}{6}\left(\frac{2a^2}{(4a+d)d} + \frac{2a^2}{(2a+d)^2} + \ln\frac{(4a+d)d}{(2a+d)^2}\right),$$

where A is the Hamaker constant, typically in the range of 10^{-20} – 10^{-19} J. This expression can be further simplified if we assume that the NC radius is much larger than the surface separation ($a \gg d$), which gives

$$U_{VdW} \approx -\frac{A}{12}\frac{a}{d}$$

From this expression, we can see that the Van der Waals attraction increases with the NC size and decreases with the surface separation.

2.2.2. Steric interactions

Without the presence of any other forces, the van der Waals attraction would lead to irreversible aggregation of the NCs and the inability to form a stabilized colloidal solution.[10] For NCs synthesized with long-chain organic ligands, this is avoided by the presence of steric interactions which is repulsive in the presence of a "good" non-polar solvent. A good solvent implies that there is a negative free energy (favorable interaction) when the organic ligands mix with the solvent molecules. When two NCs approach each other, these ligands overlap and exclude solvent molecules within this region, leading to a repulsive osmotic pressure that drives the NCs apart. On the other hand, if a "bad" solvent is introduced, there is a positive free energy (unfavorable interaction) between the NC ligands and the solvent, which leads to an attractive steric interaction between the NCs. Additionally, the "goodness" of a particular solvent also depends on the chemical nature of the ligand. For instance, a non-polar solvent like toluene would

be a good solvent for NCs with non-polar hydrocarbon ligands but may not be a good solvent for NCs with more polar ligands.

2.2.3. Electrostatic double-layer interactions

The surface of NCs in a liquid can be charged by either the ionization of surface groups or by the adsorption of ions onto the surface. This results in the build-up of an electrostatic double-layer of counterions, which consists of an inner layer of bound ions and an outer layer consisting of diffuse ions. The repulsion due to the interaction of the electrostatic double layer between two NCs allows the formation of electrostatically stabilized NCs.[11]

The electrostatic double-layer interaction between two spherical particles in a dilute mono-valent electrolyte solution is obtained by solving the Poisson-Boltzmann equation

$$\nabla^2 \cdot y = \kappa^2 \sinh y \,,$$

where $y = (ze\psi/kT)$ is the non-dimensional electric potential and κ^{-1} is the Debye length that is given by

$$\kappa^{-1} = \sqrt{\frac{\epsilon_0 \epsilon_r kT}{2N_A e^2 I}} \,,$$

where $I = \frac{1}{2}\sum_{i=1}^{n} c_i z_i^2$ is the ionic strength and ϵ_r is the relative permittivity of the solvent. Since this differential equation does not have an analytical solution, certain simplifying approximations are typically used to produce a closed-form solution for the electric potential. By applying the simplifying assumptions of the Derjaguin approximation (DA) and the linear superposition approximation (LSA),[8, 12-13] we can solve the Poisson-Boltzmann equation to obtain an expression for the electrostatic double layer (EDL) interaction energy between two NCs with constant surface potential, ψ_0, as

$$U_{EDL}^{DA,\ LSA} = 32\pi\epsilon a \tanh^2\left(\frac{\psi_0 e}{4kT}\right)\left(\frac{kT}{e}\right)^2 e^{-\kappa d} = \frac{64\pi akTc_0}{\kappa^2}\tanh^2\left(\frac{\psi_0 e}{4kT}\right) e^{-\kappa d} ,$$

where a is the NCs radius, d is the NC surface separation and c_0 is the ion concentration. However, the simplifying approximations mean that this expression is only valid when certain conditions are met, which are (1) the magnitude of the surface potential, ψ_0, is relatively small (< 30 mV), and (2) the NC radius is much bigger NC surface separation, which is larger than the Debye length ($a \gg d > \kappa^{-1}$). Another method to obtain a close-form solution to the Poisson-Boltzmann equation is by using the Derjaguin approximation (DA) in combination with the linear Poisson-Boltzmann approximation (LPB),[13-14] which gives

$$U_{EDL}^{DA,\ LPB} = 2\pi\epsilon_0\epsilon_r a\psi_0^2 \ln(1 + e^{-\kappa d}) .$$

2.3. Numerical evaluation of the electrostatic double-layer interactions

For small and highly charged NCs, the assumptions used in the Derjaguin approximation, linear superposition approximation and linear Poisson-Boltzmann approximations are not valid. This leads to large errors in the calculation of the electrostatic double-layer force. To overcome this limitation, I implemented a numerical approach that enables an accurate evaluation of the electrostatic interaction potential for scenarios that do not meet the conditions of these approximations.

The computation script (https://github.com/jiaahnp/DLVO_numerical) was written based on prior literature,[12, 15-16] and utilizes the "pdenonlin" function, which is part of the MATLAB partial differentiation toolbox. In this script, the electrostatic potential around two constant potential spheres (**Figure 2.2A**) was first evaluated using the "pdenonlin" function for a range of surface separations. The force between the particles was calculated by integrating the stress tensor across a hemisphere with the median plane as the base. The electrostatic interaction energy at each

surface separation was determined by integrating the force from a separation far enough (where the force is close to zero) to that point.

The correctness of our computation was checked by comparing our results to those in the literature (**Figure 2.2B**) and to analytical solutions that use simplifying approximations (**Figure 2.2C**). In the latter case, parameters were chosen where the approximations were most valid ($a \gg \kappa^{-1}$ and $\psi_0 \ll 25$ mV). Close agreement in both cases confirmed the validity of our numerical calculation. I then compared my computed results with the analytical solutions in the cases when the approximations where less valid ($a \approx \kappa^{-1}$ and $\psi_0 \gg 25$ mV). In this case, the approximations significantly overestimate the electrostatic repulsion, which shows the necessity for numerical approaches (**Figure 2.2D**).

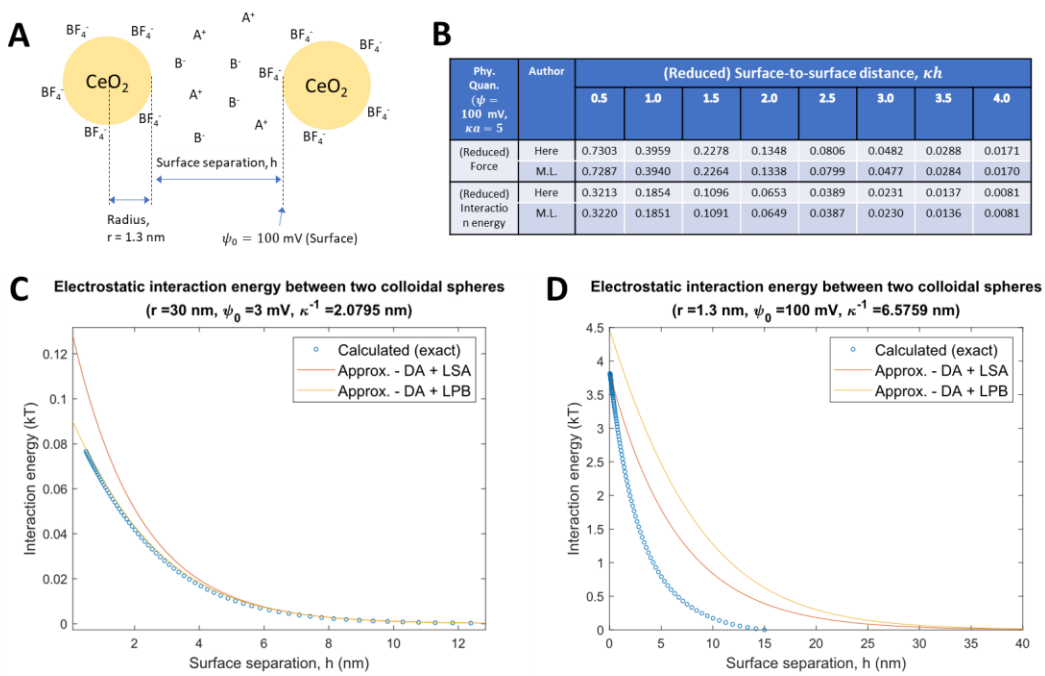

Phy. Quan. ($\psi = 100$ mV, $\kappa a = 5$	Author	(Reduced) Surface-to-surface distance, κh							
		0.5	1.0	1.5	2.0	2.5	3.0	3.5	4.0
(Reduced) Force	Here	0.7303	0.3959	0.2278	0.1348	0.0806	0.0482	0.0288	0.0171
	M.L.	0.7287	0.3940	0.2264	0.1338	0.0799	0.0477	0.0284	0.0170
(Reduced) Interaction energy	Here	0.3213	0.1854	0.1096	0.0653	0.0389	0.0231	0.0137	0.0081
	M.L.	0.3220	0.1851	0.1091	0.0649	0.0387	0.0230	0.0136	0.0081

Figure 2.2. Numerical calculation of the electrostatic double layer interaction between NCs(A) Schematic of the interaction to be evaluated. (B) Comparison between our numerical results and those in the literature.[17] (C–D) Comparison of the numerical results with approximated solutions for NCs with a small potential ($\psi_0 = 3$ mV) and large particle size (D) and for NCs with a large potential ($\psi_0 = 100$ mV) and small particle size.

2.4. Patterning NCs with light-sensitive stabilizing ligands

To pattern NCs with light-sensitive stabilizing ligands (**Figure 2.3**), we utilize in a one-phase solution exchange to functionalize the surface of the NCs with these ligands. This is done by adding the compound to organically capped NCs in a non-polar solvent like toluene. The addition of the ligand leads to the precipitation of the NCs which indicate that the long-chain organic ligand has been replaced by the small, charged ligand. This allows the NCs to be subsequently well stabilized in a polar solvent like DMF due to the formation of an electrostatic double-layer.

The NCs capped with these photosensitive ligands are then deposited as a film and exposed selectively to light through a mask. The light irradiation triggers the decomposition of the ligands which causes the reduction in surface charge and the reduction in NC solubility, forming patterns of NCs (**Figure 2.4**).

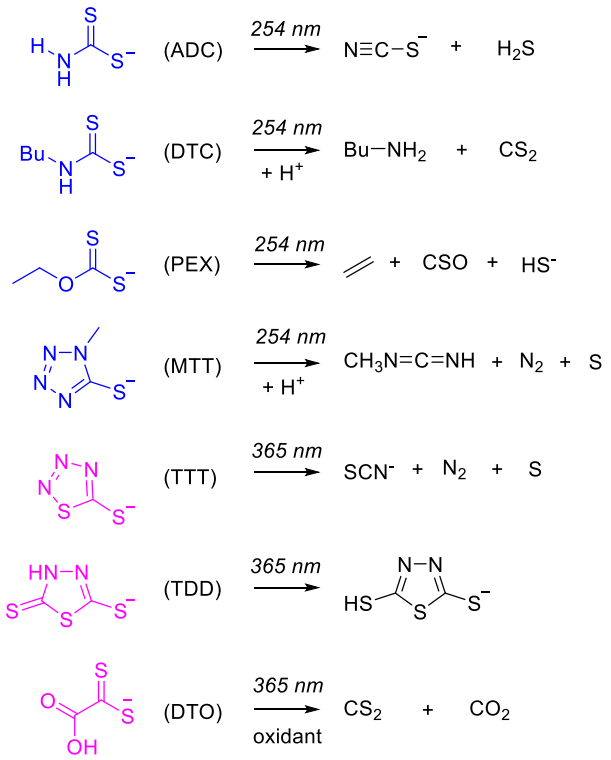

Figure 2.3. Photodecomposition reactions of the photo-sensitive stabilizing ligands explored.

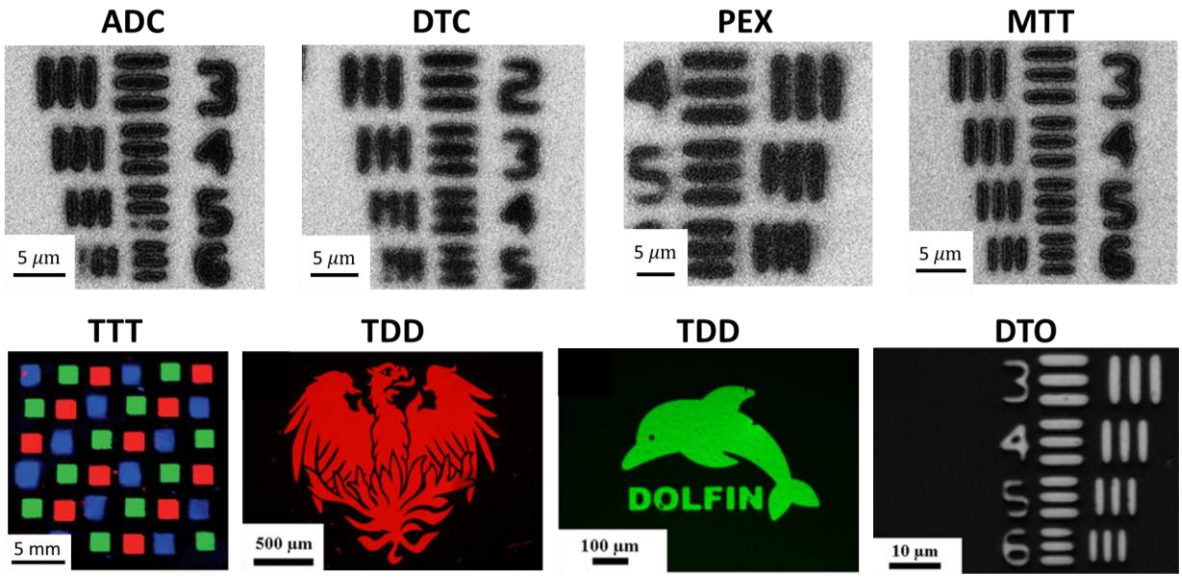

Figure 2.4. NC patterns obtained using photo-sensitive stabilizing ligands shown in **Figure 2.3**. This includes CdSe NCs capped with ADC, DTC, PEX or MTT; CdSe/ZnS (red), InP/ZnS (green), and ZnSe/ZnS (blue) NCs capped with TTT ligands;[18] CdSe/ZnS (red) and InP/ZnS (green) NC capped with TDD, CeO_2 NCs capped with DTO.

We were also interested in identifying the photodecomposition of these photosensitive stabilizing ligands. Hence, we carried out various chemical analyses to determine the chemical structures of the decomposition products.

2.4.1. Ammonium Dithiocarbamate (ADC)

FTIR and ESI-MS was used to analyze both ADC and its photodecomposition products (**Figure 2.5**). The FTIR spectra of as-synthesized ADC matched the characteristic peaks for the ammonium ion, NH_4^+ (N-H bend: 1400 cm^{-1}; N-H stretch: 3140 cm^{-1}, broad) and the dithiocarbamate anion, $H_2NCS_2^-$ (N-H primary amine bend: 1590 cm^{-1}; N-H stretch: 3402 cm^{-1}; C-N stretch: 1322 cm^{-1}).[19] Upon irradiation, the N-H and C-N peaks from the anion disappeared, which was concurrent with the appearance of the characteristic thiocyanate stretch at 2046 cm^{-1}.

This process was also corroborated with ESI-MS measurements, which showed that the dithiocarbamate anion (m/z = 92) in the ADC solution was replaced by the thiocyanate anion (m/z = 58) after DUV (254 nm) irradiation.

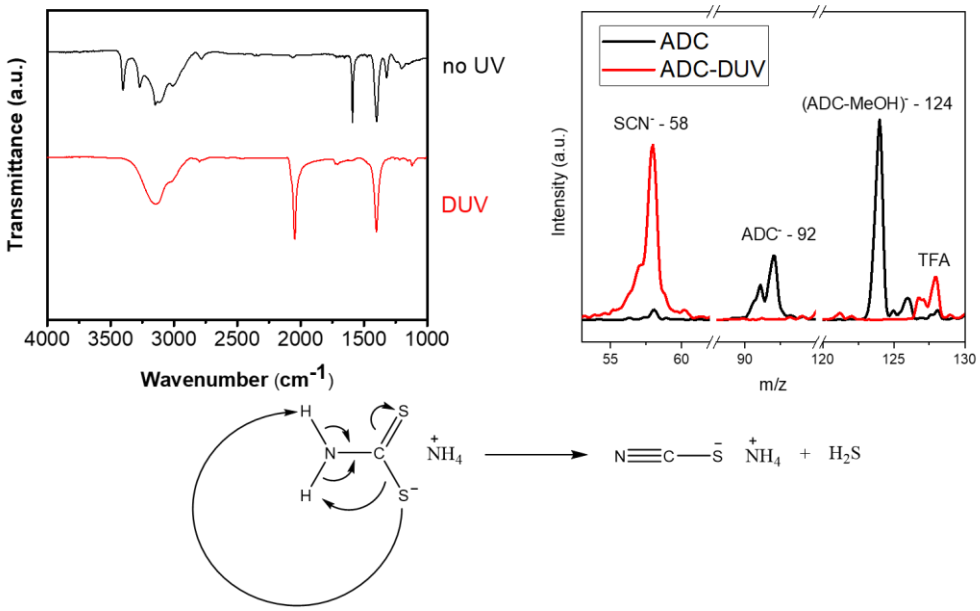

Figure 2.5. FTIR, ESI-MS and photodecomposition equation for ADC.

2.4.2. Butyldithiocarbamate (*Bu*-DTC)

From ESI-MS measurement, it was found that both the *Bu*-DTC anion ($BuNHCS_2^-$) and the butylammonium anion ($Bu\text{-}NH_3^+$) were present, which confirmed that the composition was butylammonium butyldithiocarbamate (**Figure 2.6**). Upon DUV irradiation, the *Bu*-DTC anion peaks disappeared, but the butylammonium ions remained. This was consistent with the decomposition of *Bu*-DTC into butylamine and carbon disulfide.

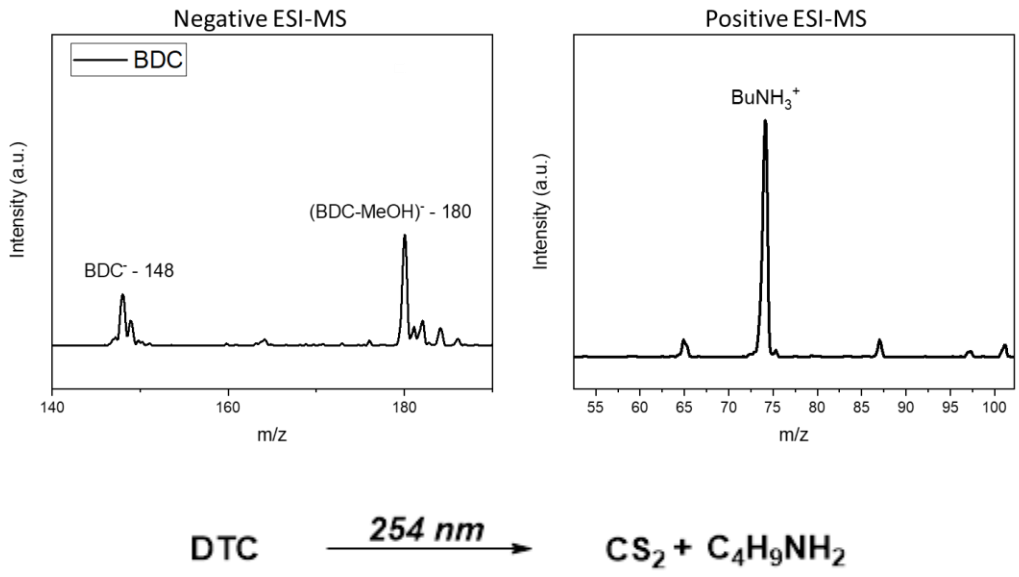

Figure 2.6. ESI-MS spectrums of *Bu*-DTC before DUV irradiation and photodecomposition equation for *Bu*-DTC.

2.4.3. Potassium Ethyl xanthate (PEX)

The ability to pattern PEX-capped NCs with much lower DUV dosages indicated a different patterning mechanism compared to the other ligands (**Figure 2.7**). Analysis with ^{1}H NMR, ESI-MS and FTIR failed to reveal any decomposition products, which was attributed to their high volatility Hence, we further pursued an investigation involving elemental analysis.

To mimic the NC-PEX surface, we synthesized cadmium ethyl xanthate, $Cd(CH_3CH_2OCS_2)_2$ or $Cd(EX)_2$, by precipitating cadmium chloride ($CdCl_2$) with PEX in H_2O. When $Cd(EX)_2$ was redissolved in DMF (50 mg/mL) and irradiated with DUV light, the precipitate that formed had a Cd:S ratio of 1:1.2 (by ICP-OES), which suggested the formation of CdS. (As a control, the Cd:S ratio in $Cd(EX)_2$ was found to be 1:3.7.) This was consistent with prior studies showing the formation of CdS upon decomposition of $Cd(EX)_2$ at temperatures as low as 160 °C[20].

Hence, we deduced the patterning mechanism as the decomposition of Cd-PEX into CdS on the NC surface, with the release of gaseous products.

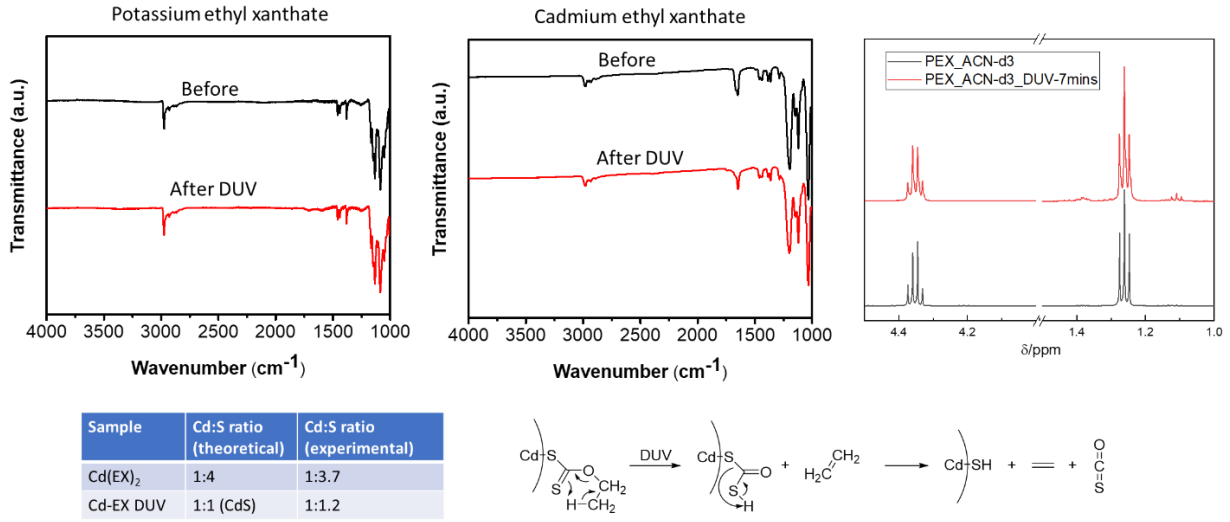

Sample	Cd:S ratio (theoretical)	Cd:S ratio (experimental)
$Cd(EX)_2$	1:4	1:3.7
Cd-EX DUV	1:1 (CdS)	1:1.2

Figure 2.7. Chemical analysis of PEX and $Cd(EX)_2$ and a proposed decomposition pathway.

2.4.4. 5-Mercapto-1-methyltetrazole (MTT)

The decomposition of the MTT ligand was investigated *via* ESI-MS and ^{13}C and ^{1}H NMR. ESI-MS results showed the presence of the m/z = 115 negative ion of the MTT compound before irradiation (**Figure 2.8**). However, after irradiation, many new peaks in positive ESI-MS appeared (m/z = 145, 173, 195, 205, 237). These peaks could be assigned to combinations of the decomposition products **a** and **b** with each other and with the original MTT molecule (table below). Further studies from NMR measurements further confirmed that the five-membered ring from the original MTT ligand disappeared right after DUV irradiation. Therefore, the photodecomposition mechanism could be deduced as the loss of N_2 to form a cyclic intermediate, followed by the release of S to form the final product. This was consistent with one of the pathways proposed previously[21].

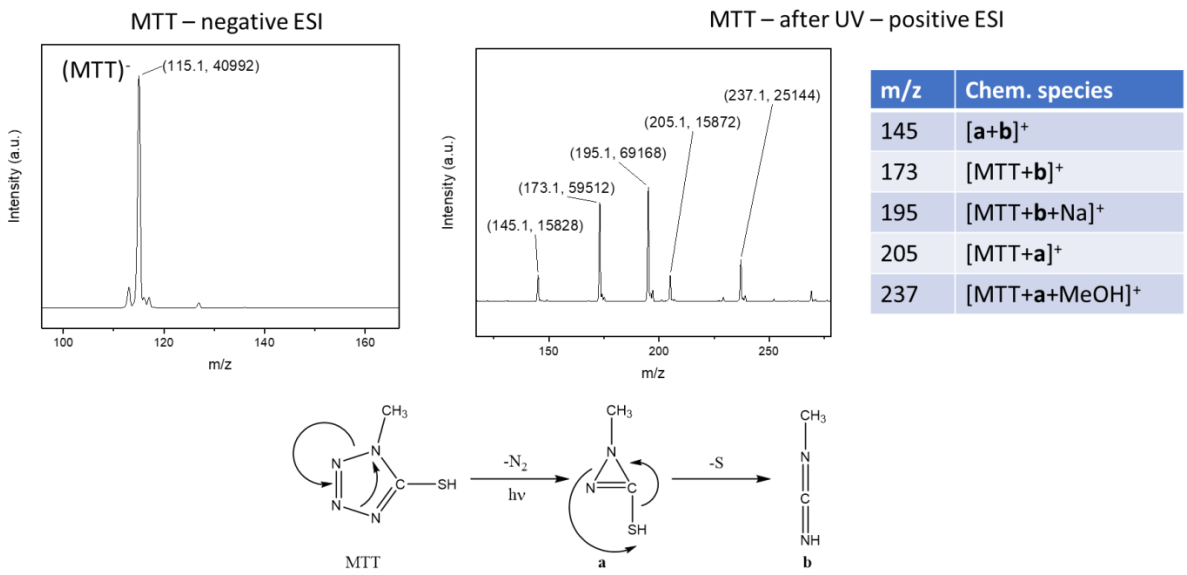

Figure 2.8. ESI-MS of MTT and its decomposition products. Below: proposed mechanism for photodecomposition.

2.4.5. 1,2,3,4-thiatriazole-5-thiolate (TTT)

The decomposition pathway of TTT into SCN^-, sulfur and nitrogen gas has been reported previously.[22] TTT molecules are quite explosive and must be handled in a solution form with special safety precautions, especially when substantial quantities of neat ligand are produced and stored. This property greatly impedes the extensively usage of TTT-based NC inks. Furthermore, we had to use DUV (254 nm) photons to trigger ligand decomposition and altered the solubility of TTT based NC inks. These challenges motivate us to explorer new ligand systems optimized for accessibility, stability, and compatibility.

1,3,4-Thiadiazole-2,5-dithiol (TDD)

Based on FTIR, ESI-MS and NMR analyses, the photopatterning mechanism with TDD did not involve photodecomposition into smaller products (**Figure 2.9**). Instead, we proposed a thiol-thione to thiol-thiol phototautomerization mechanism induced by DUV or 365 nm light,

which has been previously reported[23]. We hypothesize that this conversion of TDD into its dithiol form allows it to bind with two NCs, leading to a reduction in solubility.

When TDD was dissolved in methanol, the anions were clearly observed using ESI-MS in the negative mode (m/z = 149). ^{13}C NMR showed the presence of only one peak at 176 ppm (due to rapid conversion between tautomers) and was close to previously reported measurements (Wiley: 172 ppm, DMSO-d_6). FTIR peaks of solid TDD could be assigned with the following relevant ones: N-H (~3000 cm^{-1}: stretch, overtones, Fermi resonances; 1414 cm^{-1}: deformation), S-H (2480 cm^{-1}: stretch; 940 cm^{-1}: deformation) and thiadiazole ring stretches (1241 cm^{-1}, 1123 cm^{-1}, 1083 cm^{-1}, 1051 cm^{-1}, 716 cm^{-1}).[24-25] This was consistent with prior conclusions that TDD exists primarily in the thione-thiol form in the solid state or when dissolved in polar solvents[24]. Also, the UV-spectrum of TDD showed a peak at about 350 nm, which had been attributed to the thione form of TDD.[26]

Upon DUV or 365 nm irradiation, the 350 nm absorption peak was significantly diminished and the TDD$^-$ anions were no longer observed from ESI-MS, which could be explained by either decomposition or polymerization of TDD molecules. (Polymerizing TDD would bleach the 350 nm absorption because it would lock the molecule in the thiol form). However, both FTIR and ^{13}C NMR confirmed the later chemical transformation pathway. FTIR spectroscopy showed that after DUV irradiation, absorptions from both N-H and S-H bonds were bleached, while those from the thiadiazole ring were mostly unchanged or only slightly shifted. Furthermore, these peaks matched up with peaks from the annealing of TDD at 150 °C (slightly below its melting point), which more clearly showed S-S stretching absorption at 525 cm^{-1}. The broadening of the irradiated TDD spectrum compared to the annealed TDD spectrum could be rationalized as the higher disorder in the photo- versus the thermally induced process. Also, ^{13}C NMR showed a shift in the carbon ring

resonance to 149 ppm consistent with ChemDraw predictions of the photo-induced tautomerization. In short, TDD undergoes a photo-induced tautomerization under UV irradiation. The formation of the dithiol allows it to polymerize with one another or bridge NCs.

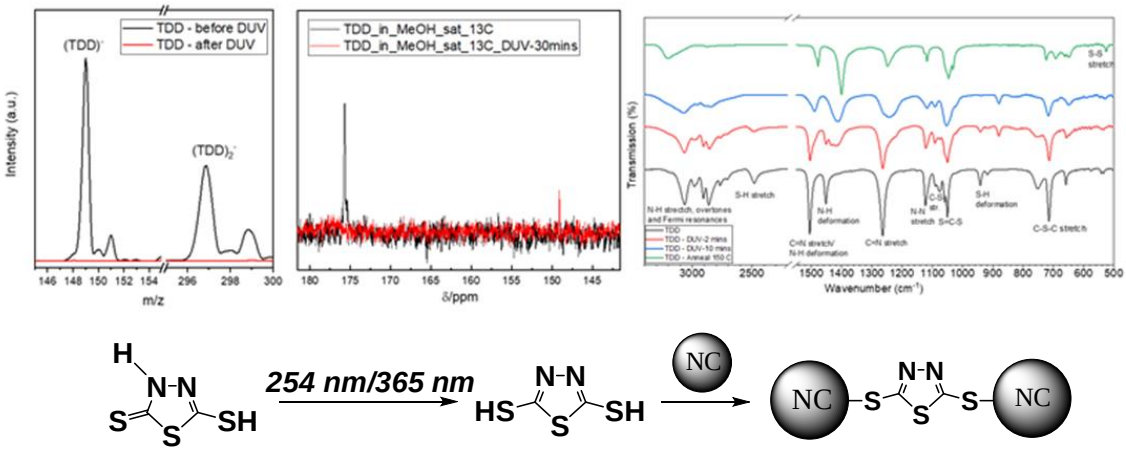

Figure 2.9. ESI-MS, ^{13}C NMR, and FTIR spectra for TDD experiments and the proposed patterning mechanism.

2.4.6. Ammonium 1,1-dithiooxalate (DTO)

The decomposition of DTO into CS_2 and CO_2 upon photolysis has been studied previously. [27]

2.5. Patterning NCs with photosensitive additives

Unlike photosensitive binding ligands that were discussed in the previous section, photosensitive additives (**Figure 2.10**) lack the ability to bind strongly to the NC surface. Hence, they are added to NCs that are already stabilized by another chemical species. In order to minimize the organic content in the film, NCs are usually stabilized electrostatically with the use of inorganic surface ions such as metal chalcogenide complexes[11] or by ligand-stripping methods.[28] Then, the

photosensitive ligand is added to this solution at an appropriate ratio and mixed thoroughly. Upon spincoating, exposure and development of this solution, patterns of NCs can be formed (**Figure 2.11**).

The photodecomposition products of these photosensitive additives have been well studied. This is due to their use as photoacid generators (PAGs) in standard polymer photolithography formulations. In these formulations, the acid formed upon light exposure is usually used to drive the polymerization, deprotection, cross-linking or depolymerization of the organic compounds in the photoresist film. [29-30] When added to NC films, these photosensitizers modulate the solubility of NCs by changing the interaction forces between the NC colloids.

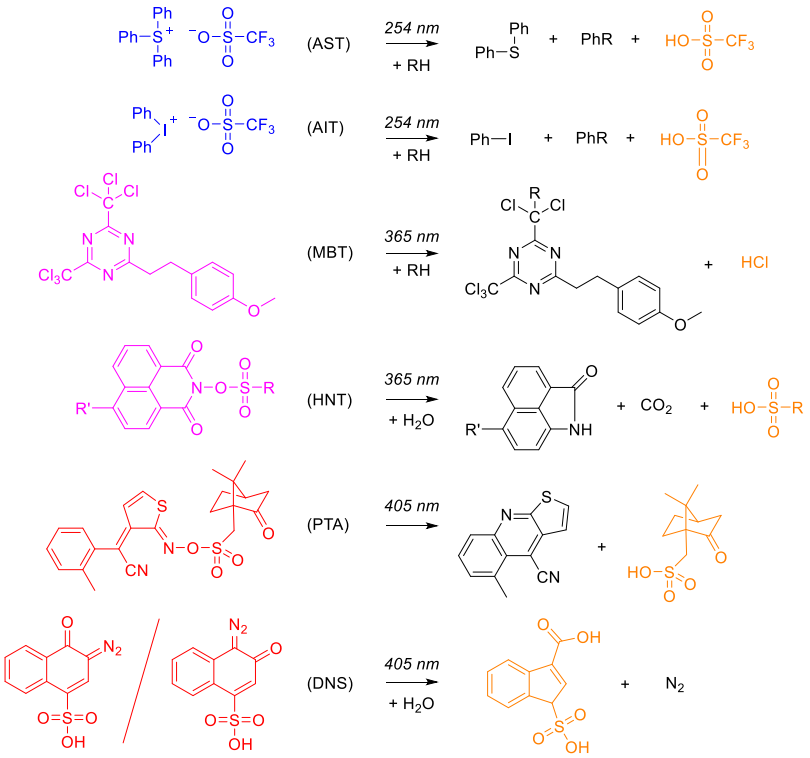

Figure 2.10. Photodecomposition of additives for NC patterning.

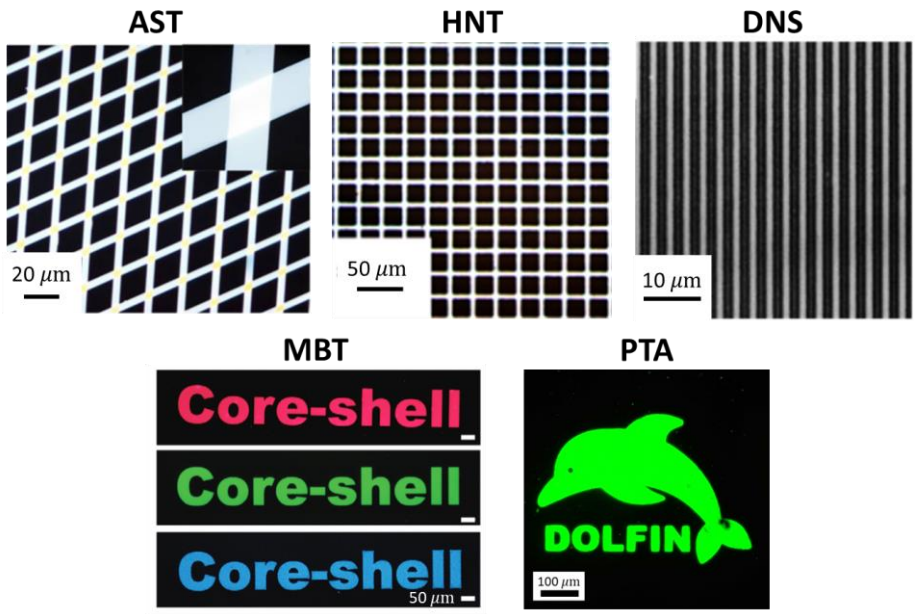

Figure 2.11. NC patterns obtained by adding a photosensitive additive to NC solutions. Chemical structures are shown in **Figure 2.10**. This includes the patterning of CeO_2-BF_4 NCs with AST, HNT or DNS, CdSe core-shell NCs with MBT,[31] and $CsPbBr_3$ NCs with PTA.

2.6. Mechanisms of solubility modulation of NCs by photosensitive ligand/additive

From a macroscopic perspective, all the photosensitive ligands and additives play the same role of reducing the NC solubility upon photoirradiation. However, the microscopic changes that occur during this process may be significantly different depending on the photosensitizer and type of NC used. In this section, we will discuss the various microscopic chemical mechanism through which the NC solubility can be changed (**Figure 2.12**). This involves photo-induced chemical reactions that affect either the electrostatic, steric, or Van der Waals interactions.

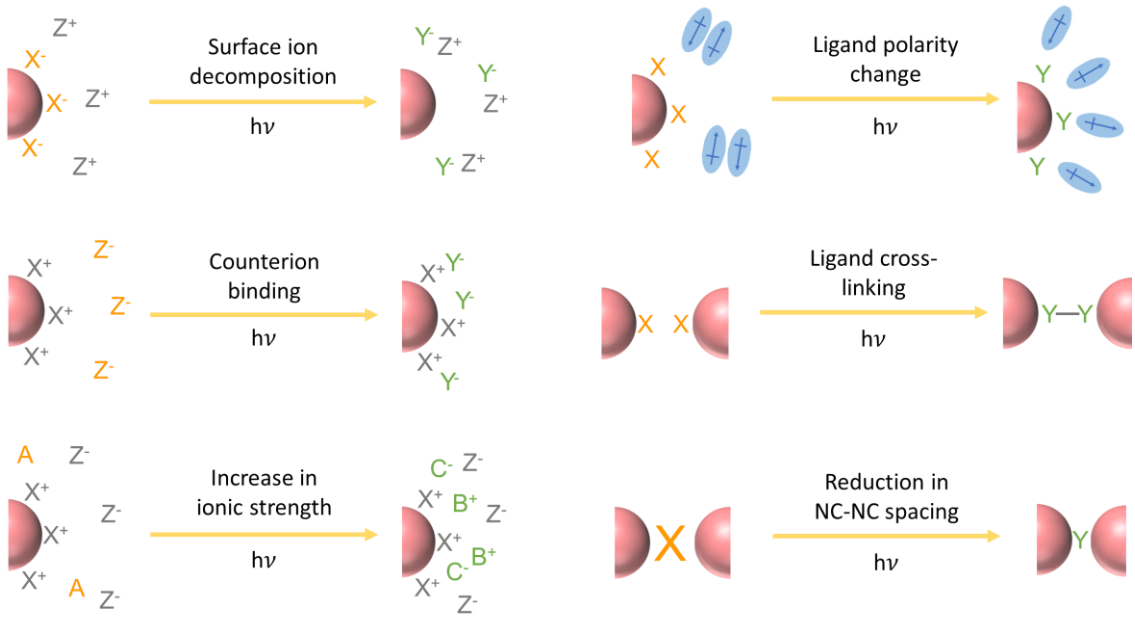

Figure 2.12. Patterning mechanisms that enable changes in NC solubility upon photodecomposition of the photosensitive ligand or additive.

For NCs that are electrostatically stabilized, its solubility in polar solvents can be reduced through the disruption of the electrostatic double layer (EDL), which can occur through several ways. For photosensitive ligands that provide surface charging, this EDL repulsion is dramatically reduced due to the reducing of the surface charge upon decomposition or desorption of the ligand. For instance, ammonium dithiocarbamate (ADC) binds strongly to the NC surface, providing a negatively charged surface that induces the formation of the EDL. Photoirradiation of ADC leads to its decomposition into the SCN^- ion, which is known to be a much weaker binder to NC surfaces.[32] Hence, the EDL collapses, leading to the insolubility of the NCs in polar solvents due to the lack or repulsive interaction to overcome the attractive van der Waals forces.

Alternatively, the EDL can be disrupted through the binding of counterions formed after photodecomposition. This binding of counterions neutralizes the surface charge and the formation of the EDL. For instance, diazonaphtholsulfonic acid (DNS) is a weakly binding negative

counterion that photo-decomposes into 3-sulfo-3H-indene-1-carboxylic acid (SICA) (**Figure 2.10**), which binds more strongly to the positively charged bare NC surface. Another example of this is photo-decomposition aryl sulfonium triflate (AST) which releases protons that bind to the negatively charged surface of NCs capped with metal chalcogenide complexes (*e.g.*, $Sn_2S_6^{4-}$).

A third way that the EDL can be photo-chemically disrupted is by increasing the ionic concentration around the NCs through the formation of ionic species from a non-ionic photosensitizer. This increase in ionic strength causes the screening of charges which compresses the thickness of the diffuse layer. This can be seen clearly from the expression for the Debye length which is inversely proportional to the square root of the ionic strength ($\kappa^{-1} \propto 1/\sqrt{I}$). An example of this patterning mechanism is the use of non-ionic photoacid generators such as HNT, which releases ions upon photodecomposition.

The patterning of sterically stabilized NCs involves disrupting the steric repulsion through changes in the interaction energy between ligands and solvent molecules. For instance, MBT can be used to pattern organically capped NCs through an *in-situ* ligand-exchange mechanism that involves the substitution of non-polar oleate ligands with polar chloride ligands released during upon photodecomposition of MBT. This increases the polarity of the NC surface which makes it insoluble in non-polar solvents like toluene. Another example is the use of PTA to pattern lead halide perovskite (LHP) NCs. PTA is a relatively non-polar molecule that binds to the LHP NC surface. Upon irradiation, PTA is photo-cleaved into two fragments, one of which is more polar and remains on the NC surface while the other is washed away. This also results in the increase in polarity of the NC surface, reducing its solubility in non-polar solvents.

Another patterning mechanism involves the photo-induced cross-linking between ligands or between NCs. For instance, the sufficient UV irradiation of semiconductor NCs capped with

oleate ligands lead to the formation of C–C cross-links between the ligands.[33] Another example of this cross-linking approach is in the case of TDD which undergoes a photo-isomerization that enables it to bind to different NCs through its two thiol binding groups.

Finally, the solubility of NCs can be modulated though changes in the NC−NC separation upon photodecomposition of the ligand/additive. We observed that depositing and drying bare NCs on their own leads to insoluble NC films, while depositing and drying NCs mixed with an appropriate additive (*e.g.*, AST) allows the NC film to be subsequently redissolved. Hence, we infer that these additives play a role of keeping NCs well-separated from one another, which prevents the van der Waals forces from irreversibly aggregating the NCs. During the patterning process, photodecomposition of this additive into smaller fragments lead to a reduction of this spacing, allowing NCs to aggregate and become insoluble in the developer.

2.7. Summary

In summary, we have developed a library of photosensitive ligands or additives that allow the NC solubility to be modulated though the exposure of various wavelengths of light. These DOLFIN photosensitizers allows the patterning of a variety of types of NCs through the use of various microscopic mechanisms that lead to changes in NC solubility.

2.8. Chapter bibliography

1. Nag, A.; Kovalenko, M. V.; Lee, J.-S.; Liu, W.; Spokoyny, B.; Talapin, D. V., Metal-free inorganic ligands for colloidal nanocrystals: S2–, HS–, Se2–, HSe–, Te2–, HTe–, TeS32–, OH–, and NH2–as surface ligands. *J. Am. Chem. Soc.* **2011,** *133* (27), 10612-10620.

2. Huang, J.; Liu, W.; Dolzhnikov, D. S.; Protesescu, L.; Kovalenko, M. V.; Koo, B.; Chattopadhyay, S.; Shenchenko, E. V.; Talapin, D. V., Surface functionalization of semiconductor and oxide nanocrystals with small inorganic oxoanions (PO43–, MoO42–) and polyoxometalate ligands. *ACS Nano* **2014,** *8* (9), 9388-9402.

3. Dolzhnikov, D. S.; Zhang, H.; Jang, J.; Son, J. S.; Panthani, M. G.; Chattopadhyay, S.; Shibata, T.; Talapin, D. V., Composition-matched molecular “solders” for semiconductors. *Science* **2015,** *347*, 425-428.

4. Zhang, H.; Kurley, J. M.; Russell, J. C.; Jang, J.; Talapin, D. V., Solution-Processed, Ultrathin Solar Cells from CdCl3−-capped CdTe Nanocrystals: The Multiple Roles of CdCl3−Ligands *J. Am. Chem. Soc.* **2016,** *138*, 7464–7467.

5. Zhang, H.; Son, J. S.; Dolzhnikov, D. S.; Filatov, A. S.; Hazarika, A.; Wang, Y.; Hudson, M. H.; Sun, C.; Chattopadhyay, S.; Talapin, D. V., Soluble Lead and Bismuth Chalcogenidometallates: Versatile Solders for Thermoelectric Materials. *Chemistry of Materials* **2017,** *29*, 6396-6404.

6. Kagan, C. R.; Lifshitz, E.; Sargent, E. H.; Talapin, D. V., Building Devices from Colloidal Quantum Dots. *Science* **2016,** *353*, aa5523-1-aa5523-9.

7. Hamaker, H. C., The London—van der Waals attraction between spherical particles. *Physica* **1937,** *4* (10), 1058-1072.

8. Israelachvili, J. N., *Intermolecular and surface forces*. Academic press: 2011.

9. Liu, L.; Neretnieks, I., Interaction between colloidal particles. Literature review. **2010**.

10. Boles, M. A.; Ling, D.; Hyeon, T.; Talapin, D. V., The surface science of nanocrystals. *Nat. Mater.* **2016,** *15* (2), 141-153.

11. Kovalenko, M. V.; Scheele, M.; Talapin, D. V., Colloidal Nanocrystals with Molecular Metal Chalcogenide Surface Ligands. *Science* **2009,** *324* (5933), 1417.

12. Carnie, S. L.; Chan, D. Y.; Stankovich, J., Computation of forces between spherical colloidal particles: nonlinear Poisson-Boltzmann theory. *J. Colloid Interface Sci.* **1994,** *165* (1), 116-128.

13. Bhattacharjee, S.; Elimelech, M.; Borkovec, M., DLVO interaction between colloidal particles: beyond Derjaguin’s approximation. *Croat. Chem. Acta* **1998,** *71* (4), 883-903.

14. Hogg, R.; Healy, T. W.; Fuerstenau, D., Mutual coagulation of colloidal dispersions. *Transactions of the Faraday Society* **1966,** *62*, 1638-1651.

15. Hoskin, N.; Levine, S., The interaction of two identical spherical colloidal particles-The interaction of two identical spherical colloidal particles. II. The free energy. *Philosophical Transactions of the Royal Society of London. Series A, Mathematical and Physical Sciences* **1956,** *248* (951), 449-466.

16. Hoskin, N.; Levine, S., The interaction of two identical spherical colloidal particles-The interaction of two identical spherical colloidal particles. I. Potential distribution. *Philosophical Transactions of the Royal Society of London. Series A, Mathematical and Physical Sciences* **1956,** *248* (951), 433-448.

17. McCartney, L.; Levine, S., An improvement on Derjaguin's expression at small potentials for the double layer interaction energy of two spherical colloidal particles. *J. Colloid Interface Sci.* **1969,** *30* (3), 345-354.

18. Wang, Y.; Fedin, I.; Zhang, H.; Talapin, D. V., Direct optical lithography of functional inorganic nanomaterials. *Science* **2017,** *357* (6349), 385-388.

19. Colthup, N., Spectra-structure correlations in the infra-red region. *JOSA* **1950,** *40* (6), 397-400.

20. Nair, P. S.; Radhakrishnan, T.; Revaprasadu, N.; Kolawole, G.; O'Brien, P., Cadmium ethylxanthate: A novel single-source precursor for the preparation of CdS nanoparticles. *J. Mater. Chem.* **2002,** *12* (9), 2722-2725.

21. Gómez-Zavaglia, A.; Reva, I.; Frija, L.; Cristiano, M.; Fausto, R., Molecular structure, vibrational spectra and photochemistry of 5-mercapto-1-methyltetrazole. *J. Mol. Struct.* **2006,** *786* (2-3), 182-192.

22. Webber, D. H.; Brutchey, R. L., Nanocrystal ligand exchange with 1, 2, 3, 4-thiatriazole-5-thiolate and its facile in situ conversion to thiocyanate. *Dalton Transactions* **2012,** *41* (26), 7835-7838.

23. Rostkowska, H.; Lapinski, L.; Nowak, M. J., UV-induced transformations of matrix-isolated 1, 3, 4-thiadiazole-2-thiones. *J. Phys. Org. Chem.* **2010,** *23* (1), 56-66.

24. Hipler, F.; Fischer, R. A.; Müller, J., Examining thermolysis reactions and tautomerism of 2-mercapto-5-methyl-1, 3, 4-thiadiazole and 2, 5-dimercapto-1, 3, 4-thiadiazole. *Journal of the Chemical Society, Perkin Transactions 2* **2002,** (9), 1620-1626.

25. Pope, J. M.; Sato, T.; Shoji, E.; Oyama, N.; White, K. C.; Buttry, D. A., Organosulfur/conducting polymer composite cathodes II. Spectroscopic determination of the protonation and oxidation states of 2, 5-dimercapto-1, 3, 4-thiadiazole. *J. Electrochem. Soc.* **2002,** *149* (7), A939-A952.

26. Thorn, G., ABSORPTION SPECTRA OF 2, 5-DIMERCAPTO-1, 3, 4-THIADIAZOLE AND ITS METHYL DERIVATIVES. *Can. J. Chem.* **1960,** *38* (9), 1439-1444.

27. Bernt, C. M.; Burks, P. T.; DeMartino, A. W.; Pierri, A. E.; Levy, E. S.; Zigler, D. F.; Ford, P. C., Photocatalytic Carbon Disulfide Production via Charge Transfer Quenching of Quantum Dots. *Journal of the American Chemical Society* **2014,** *136*, 2192-2195.

28. Dong, A.; Ye, X.; Chen, J.; Kang, Y.; Gordon, T.; Kikkawa, J. M.; Murray, C. B., A generalized ligand-exchange strategy enabling sequential surface functionalization of colloidal nanocrystals. *J. Am. Chem. Soc.* **2010,** *133* (4), 998-1006.

29. Tsuchimura, T., Recent Progress in Photo-Acid Generators for Advanced Photopolymer Materials. *J. Photopolym. Sci. Technol.* **2020,** *33* (1), 15-26.

30. Shirai, M.; Tsunooka, M., Photoacid and photobase generators: chemistry and applications to polymeric materials. *Prog. Polym. Sci.* **1996,** *21* (1), 1-45.

31. Cho, H.; Pan, J. A.; Wu, H.; Lan, X.; Coropceanu, I.; Wang, Y.; Cho, W.; Hill, E. A.; Anderson, J. S.; Talapin, D. V., Direct Optical Patterning of Quantum Dot Light-Emitting Diodes via In Situ Ligand Exchange. *Adv. Mater.* **2020,** *32* (46), 2003805.

32. Fafarman, A. T.; Koh, W. K.; Diroll, B. T.; Kim, D. K.; Ko, D. K.; Oh, S. J.; Ye, X.; Doan-Nguyen, V.; Crump, M. R.; Reifsnyder, D. C.; Murray, C. B.; Kagan, C. R., Thiocyanate-capped nanocrystal colloids: vibrational reporter of surface chemistry and solution-based route to enhanced coupling in nanocrystal solids. *J. Am. Chem. Soc.* **2011,** *133* (39), 15753-61.

33. Jun, S.; Jang, E.; Park, J.; Kim, J., Photopatterned semiconductor nanocrystals and their electroluminescence from hybrid light-emitting devices. *Langmuir* **2006,** *22* (6), 2407-2410.

Chapter 3. Direct optical lithography of colloidal metal oxide nanomaterials for diffractive optical elements with 2π phase control

Adapted with permission from J.-A. Pan *et al. J. Am. Chem. Soc.,* **2021**, *143*, 5, 2372-2383 and Y. Wang, J.-A. Pan *et al. ACS Nano*, **2019**, *13*, 12, 13917-13931. Copyright 2021/2019 American Chemical Society.

3.1. Introduction to oxide NC patterning

Metal oxide layers are widely used as dielectric, semiconducting, or conductive layers in transistors,[1] gas sensors,[2] waveguides,[3] diffractive optical elements,[4] and recently, dielectric metasurfaces.[5-6] Their widespread implementation can be attributed to thermal and mechanical robustness, coupled with desirable chemical, optical, and electronic properties such as optical transparency, high refractive index, and tunable conductivity.[7] Importantly, high-resolution patterning is often essential to fully harness these properties and to integrate the oxide layers in practical devices.

An established method to fabricate oxide patterns involves photolithography of a sacrificial polymer resist layer followed by pattern transfer via etching (e.g., by reactive ion etching, RIE) or vapor-phase deposition (e.g., by atomic layer deposition, ALD) of the oxide layer. These methods work extremely well for some applications (e.g., in nanoelectronics) but face challenges when applied to large-area substrates or thick oxide layers. Traditional ALD and RIE methods are also poorly applicable for low-cost applications (e.g., disposable radio-frequency identification tags and sensors). As an alternative, solution-based deposition techniques possess the advantages of lower costs, milder conditions, and shorter fabrication times. Various approaches have been developed to directly pattern solution-deposited oxide layers without the use of sacrificial photoresists. These include nanoimprint lithography,[8] direct ink writing,[9] dip-pen lithography,[10]

extreme-UV lithography[11], electron-beam lithography,[12] and direct optical lithography.[7] Among these, direct optical lithography through a light-induced change in solubility of a photosensitive oxide ink is particularly attractive due to its simplicity, good resolution, and high throughput. This method can also utilize established light projection systems that have already been developed extensively for microelectronics, thus facilitating its facile and widespread implementation. Furthermore, developments in the chemistry of the photosensitive inks can be further adapted for light-based 3D printing technologies such as stereolithography and two-photon lithography.[13-14]

Among the different solution-processable precursors for inorganic materials, colloidal nanoparticles (NPs) allow for high atom economy during the precursor-to-inorganic layer transformations because they already contain multiatomic units of the target phase.[15] This high atom economy translates into small volume contraction during annealing of patterned precursor layers. Colloidal oxide NPs are formed by controlled hydrolysis/condensation reactions in either aqueous or nonaqueous media. The aqueous route commonly referred to as the sol-gel process involves the hydrolysis and condensation of metal oxo complexes in either acidic or basic conditions.[16] On the other hand, nonaqueous techniques initially developed for synthesizing luminescent quantum dots have been applied to making colloidal oxide NPs.[17] This method involves the hot injection or heating of metal oxide precursors in the presence of long chain ligands (e.g., oleic acid, oleylamine, trioctylphosphine oxide) in an organic solvent.[18-19] With a large-scale industry developed around oxide NPs, a multitude of applications should benefit from the ability to directly optically pattern these NPs.[20]

Oxide NPs can be photopatterned by embedding them in a matrix of photosensitive organic monomers subsequently polymerized by light.[13, 21] A common issue with this approach is phase separation between the inorganic and organic components, which can affect properties like

transparency and porosity.[22] Alternatively, photosensitivity can be built into the NPs themselves by tailoring their ligand chemistry. Giannelis, Ober, and co-workers have systematically investigated the use of oxide NPs (e.g., HfO_2, ZrO_2, ZnO) with short chain carboxylate ligands for high-resolution deep-UV and extreme-UV lithography.[23-24] They proposed mechanisms involving photoinduced ligand desorption and ligand exchange leading to solubility changes. Other patterning methods such as cross-linking long-chain ligands,[25-27] photocleavable ligands that change polarity upon decomposition,[28] and light sensitive DNA moieties[29] have been used to pattern metal or semiconductor NPs and should be extendable to oxide NPs as well.

In the last few years, we have been developing methods for the direct optical lithography of functional inorganic nanomaterials (DOLFIN), which emphasizes minimizing the amount of organic components in the patterned layers.[30-31] Although inorganic–organic hybrid materials are appropriate even advantageous for certain applications (e.g., flexible substrates and bio interfacing), there are many important applications that have been hindered by the inclusion of organic components.[32] These include applications that require strong electronic coupling between NPs, infrared transparency, high refractive indices, and wide thermal tolerance. One instance of these requirements is the fabrication of phase-shifting diffractive optical elements (DOEs), which utilize the principle of diffraction and interference to manipulate the properties of light. These transparent DOEs shape the wavefront of light by spatial variations in the retardation of incident light. To achieve arbitrary wavefront shaping, full 2π phase retardation is required, which can be achieved through patterns of sufficiently thick films with high refractive indices. Moreover, these optical devices often require good thermal and mechanical robustness for operational longevity, which may be compromised by the inclusion of a large organic fraction.

Herein, we use DOLFIN to fabricate high-performing oxide DOEs with full 2π phase control. Such optical elements have stringent requirements such as a large thickness, high refractive index, and optical-grade smoothness of patterned layers. A photosensitive oxide ink was formulated by mixing electrostatically stabilized oxide NPs with 1–25 wt % of the diazo compound 1-diazo-2-napthol-4-sulfonic acid (DNS), which is photosensitive to UV-blue light (350–450 nm). We directly photopattern thick (> 1 μm) films of amorphous zirconia NPs, which allow for 2π phase control of visible light. These structures are highly transparent, have a high refractive index ($n \sim 1.84$), and can withstand multiple layer patterning. To demonstrate its optical capabilities, we fabricate films with structurally colored pixels as well as binary transmission gratings that show high diffraction efficiencies. We also show generalizability to various types of electrostatically stabilized oxide NPs (TiO_2, HfO_2, and ITO) made by different synthetic methods. This work showcases the capability of direct patterning methods for colloidal nanomaterials and their use in photonic applications.

3.2. Selection of diazo-2-naphthol-4-sulfonic acid (DNS) as the photosensitive compound.

To make optical elements with good diffractive capabilities, the patterning of thick oxide layers is required. This can be achieved by direct optical lithography of a thick film of oxide NPs mixed with a photosensitive additive, with the caveat that the oxide matrix needs to be highly transparent at the irradiation wavelength. This crucially allows the exposure light to penetrate deep into the film, decomposing the photosensitive compound throughout the thickness of the film. Since many oxide materials absorb in the UV, we decided to utilize a compound that is sensitive to violet (405 nm) light. One of the most well-known classes of commercial photoresists for UV-

violet lithography are the diazonaphthoquinone (DNQ) photoresists, which consist of a photosensitive DNQ sulfonate ester mixed with a transparent phenolic polymer matrix.[33] Upon irradiation, the DNQ compound decomposes into a transparent indene carboxylic acid, changing the solubility of the resist in an aqueous base developer. Although cutting-edge photolithography has moved to deep-UV and extreme-UV exposure, the DNQ photoresists are still widely used in microlithography workflows.

Inspired by the commercial success of DNQ-polymer photoresists, we investigated the use of DNQ-like compounds to directly pattern thick layers of oxide NPs. We explored several DNQ variants including 4-(1-methyl-1-phenylethyl)phenyl 3-diazo-3,4-dihydro-4-oxo-1-naphthalenesulfonate (DNQ-Ar), 2-diazo-1-naphthol-4-sulfonyl chloride (DNQ-Cl), 2-diazo-1-naphthol-4-sulfonic acid (2-DNS) and 1-diazo-2-naphthol-4-sulfonic acid (1-DNS). All these compounds decompose into 3-sulfo-3H-indene-1-carboxylic acid (SICA) upon photoirradiation. The chemical structures of these compounds are shown in **Table 3.1**. We first tested the use of DNQ-Ar, a typical sulfonate ester variant used in commercial photoresists. Unfortunately, it did not significantly change the solubility of oxide NPs upon photoirradiation (i.e., low contrast), which we attribute to the interference of the phenol reaction products. On the other hand, DNQ variants with no phenol adducts (DNQ-Cl, 2-DNS, 1-DNS) were found to appreciably alter NP solubility after photoirradiation. However, we did not further investigate the use of DNQ-Cl due to its highly reactive sulfonyl chloride moiety which is easily hydrolyzed, releasing H^+ and Cl^- ions that can prematurely destabilize NPs by perturbing the pH or by binding to NP surfaces. [34]

Table 3.1. Chemical structures of SICA and different DNQ variants investigated.

Chemical structure	Chemical name
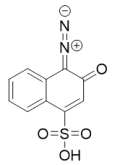	1-Diazo-2-naphthol-4-sulfonic acid **(1-DNS** or **DNS)**
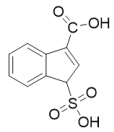	3-Sulfo-3H-inden-1-carboxylic acid **(SICA)**
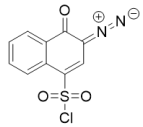	2-Diazo-1-naphthol-4-sulfonyl chloride **(DNQ-Cl)**
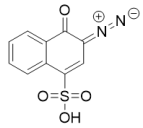	2-Diazo-1-naphthol-4-sulfonic acid **(2-DNS)**
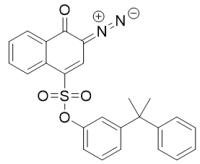	4-(1-Methyl-1-phenylethyl)phenyl 3-Diazo-3,4-dihydro-4-oxo-1-naphthalenesulfonate **(DNQ-Ar)**

We obtained the best and most reproducible results with the sulfonic acid variants of DNQ, such as 1-DNS and 2-DNS. These two compounds are regioisomers (the diazo and oxo positions on the ring are swapped), but they both photodecompose into SICA due to an intermediate Wolff rearrangement step (**Figure 3.1**). In this report, we primarily utilize 1-DNS as it is commercially available, but have found 2-DNS to perform equivalently. For simplicity, we will henceforth use DNS to refer to 1-DNS.

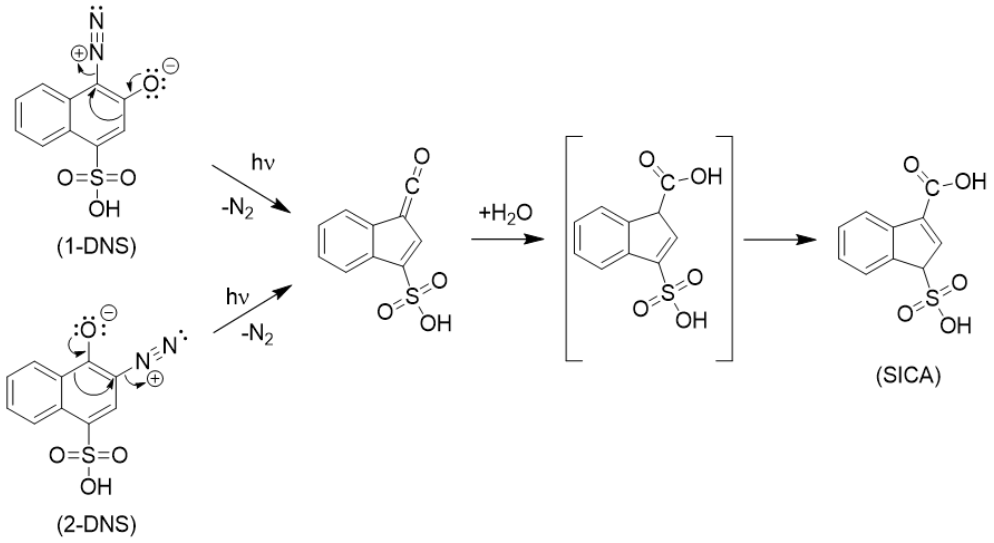

Figure 3.1. Mechanism of conversion of 1-DNS and 2-DNS into SICA.[33]

We first characterized the photochemical properties of DNS on its own before implementing it in a NP ink. **Figure 3.2** shows the absorption spectra of DNS before and after its photodecomposition into SICA. DNS absorbs 405 nm light strongly with an absorption coefficient of $\epsilon_{405\ \mathrm{nm}} = 4.23 \times 10^3\ \mathrm{M^{-1}cm^{-1}}$. Upon photoirradiation, it decomposes into SICA, which has an absorption coefficient at 405 nm that is five orders of magnitude smaller ($\epsilon_{405\ \mathrm{nm}} = 4.42 \times 10^{-2}\ \mathrm{M^{-1}cm^{-1}}$). This shows that the photodecomposition process is highly sensitive and efficient. The pronounced photobleaching of DNS also contributes to the ability of light to penetrate deep into a film, facilitating the pattering of thick NP layers.

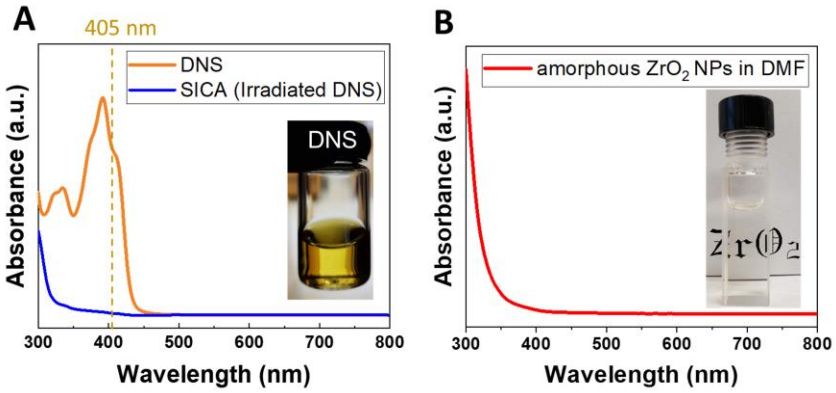

Figure 3.2. Optical properties of the sensitizer and NCs.Absorption spectra of (A) diazo-2-naphthol-4-sulfonic acid (DNS) before and after its photodecomposition into 3-sulfo-3H-indene-1-carboxylic acid (SICA) and (B) amorphous ZrO_2 NPs after solvent exchange from water into DMF. Insets: photographs of the DNS and ZrO_2 NP solutions.

3.3. Photochemically active oxide NP inks

To prepare the photosensitive colloidal dispersion of NPs, both the DNS compound and the NPs must be highly soluble in a suitable solvent. *N*,*N*-dimethylformamide (DMF) was chosen as the solvent because it solubilizes both DNS and electrostatically charged NPs.[35] DMF also has an acceptably low boiling point (153 °C), which facilitates the spin coating of thick films.

Depending on the method of NP synthesis, different approaches were employed to obtain stable colloids of NPs in DMF (**Figure 3.3**). NPs synthesized by aqueous sol–gel methods are already electrostatically stabilized and can be dispersed in DMF by a simple solvent exchange procedure from H_2O. We found that the complete removal of water was necessary due to the insolubility of DNS in water. However, since the dielectric constant of DMF is significantly lower than that of H_2O (36.7 versus 80.1), this procedure only works for reasonably small sized NPs (<20 nm) with highly noncoordinating anions (e.g., NO_3^-). On the other hand, a different process is used for NPs capped with long chain organic ligands (e.g., oleic acid). For these NPs, a stripping

agent (e.g., $NOBF_4$) is used to remove the organics and replace it with noncoordinating anions, rendering them soluble in DMF.[35]

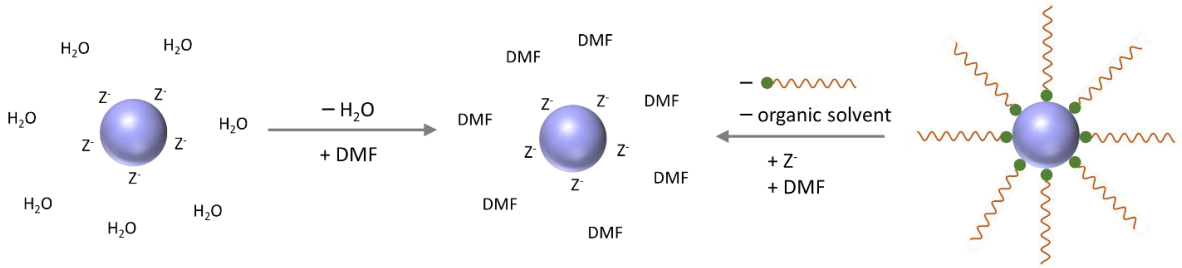

Figure 3.3. The two methods of obtaining colloidal NPs in DMF involving either a solvent exchange or a ligand stripping procedure (Z^- is a noncoordinating anion).

The photosensitive oxide NP ink is then obtained by simply adding DNS to the colloidal oxide NP solution in DMF. The percentage dry mass of DNS to NPs was optimized for each type of NP, typically ranging between 1–25 wt %. In this report, we frequently utilize amorphous ZrO_2 NPs with positively charged surface and nitrate counterions as a convenient material system to demonstrate concepts applicable to a broad class of oxide NPs. After solvent exchange into DMF, these ZrO_2 NPs remain well-dispersed as indicated by their small hydrodynamic size (~6 nm) and large positive zeta potential (+45 mV) (**Figure 3.4**). The particles are stable to aggregation on the timescale of weeks. The colloidal solution is visibly clear without any cloudiness and is highly transparent to visible light, including 405 nm radiation (**Figure 3.2B**). The addition of DNS only slightly perturbs the NP colloidal stability by causing a small reduction in the zeta potential (+45 mV to +32 mV) upon the addition of an excess of DNS (100 wt % of DNS to NPs), which we attribute to the increase in ionic strength from the dissociation of DNS in DMF (**Figure 3.4B**). We thus infer that DNS only interacts weakly with the NC surface by contrasting this behavior with the drastic changes of zeta potential observed during the addition of strongly coordinating ionic ligands.[36-37] The highly charged NPs allow us to make highly concentrated amorphous ZrO_2 NP

solutions (e.g., 250 mg/mL ZrO_2 NPs + 62.5 mg/mL DNS in DMF) that remained colloidally stable and transparent.

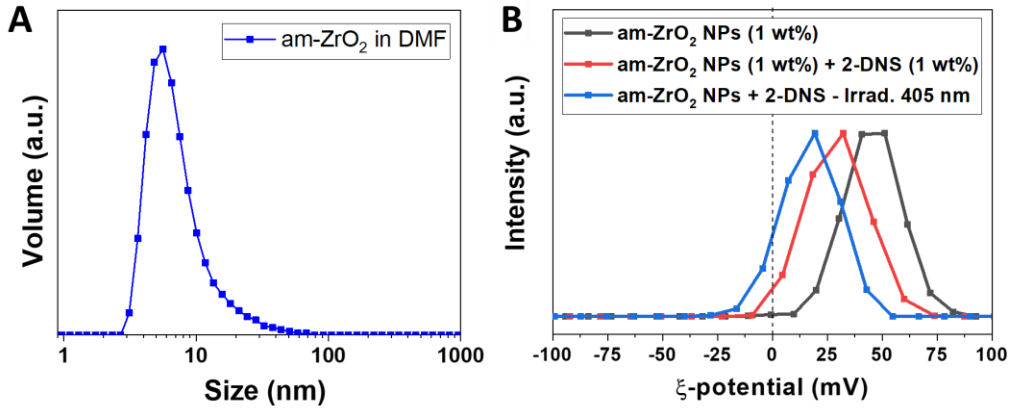

Figure 3.4. Size of the NPs and changes in zeta potential during the patterning process (A) Hydrodynamic size of amorphous ZrO_2 NPs after solvent change from water into DMF, measured by dynamic light scattering (DLS). (B) Changes in zeta potential of amorphous ZrO_2 NPs upon addition of DNS and after photoirradiation.

This method is generalizable to several other oxide NP solutions obtained by either the solvent exchange method (e.g., anatase TiO_2 NPs) or by the $NOBF_4$ ligand stripping method[35] (e.g., tetragonal phase ZrO_2 NPs, monoclinic HfO_2 NPs, and cubic phase ITO NPs), but with nuances in terms of the ultimate concentrations achievable and percentage of DNS required for patterning. For instance, NPs obtained from the ligand stripping method usually require less DNS for patterning (as low as 1 wt % of DNS to NPs). We attribute this to their better monodispersity and higher crystallinity, which lead to a smaller percolation threshold for 3D aggregation and a steeper van der Waals attractive potential, respectively.

3.4. Insights into the mechanism of patterning oxide NPs with DNS

The direct photopatterning process of oxide NPs with DNS is shown in **Figure 3.5**. First, the ink is spincoated on a substrate to form a smooth layer of NPs (step 1). As the solvent evaporates, the DNS molecules begin to interact more with the charged NPs and condense around them. Even prior to its photodecomposition, the DNS molecules serve an important role as spacers for the NPs, preventing them from aggregating irreversibly due to van der Waals forces. Hence, without light exposure, we found that the NP–DNS films can be redissolved in DMF. In contrast, oxide NPs deposited *without* DNS were found to be irreversibly insoluble in DMF upon drying. In this case, we hypothesize that NPs fall into the primary wells of their DLVO pair potentials, preventing any further manipulation of their solubilities.

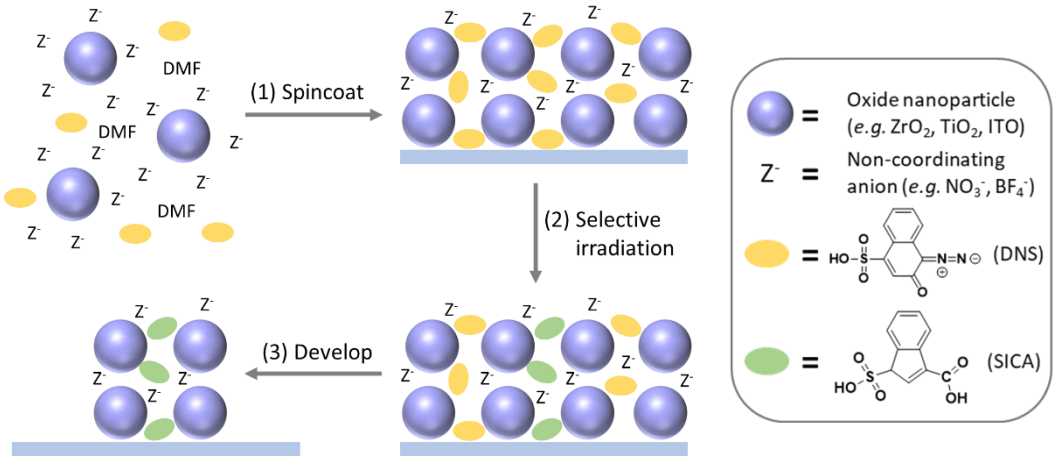

Figure 3.5. Direct photolithography process of oxide nanoparticles with DNS.

Area-selective photoirradiation of the NP–DNS film leads to the decomposition of DNS into SICA in those regions (step 2 in **Figure 3.5**). This is confirmed with Fourier transform infrared (FTIR) spectroscopy (**Figure 3.6**) by disappearance of the C=N=N and C–N≡N stretching peaks (2110 cm^{-1} and 2164 cm^{-1}, respectively)[38] and the appearance of carboxylic acid peaks (1710 cm^{-1}, 1426 cm^{-1}). This is also corroborated by electrospray ionization mass spectroscopy (ESI-MS) in

the negative ion mode (**Figure 3.7A**), which shows the molecular mass change from 2-DNS (m/z = 249) to SICA (m/z = 239). This molecular mass change is consistent with the release of N_2 and the reaction with adventitious water in DMF. This photodecomposition significantly reduces the solubility of the film in the regions that were irradiated, while unexposed areas remain highly soluble in DMF (step 3 in Scheme 1). Hence, oxide NP patterns are revealed upon development with DMF.

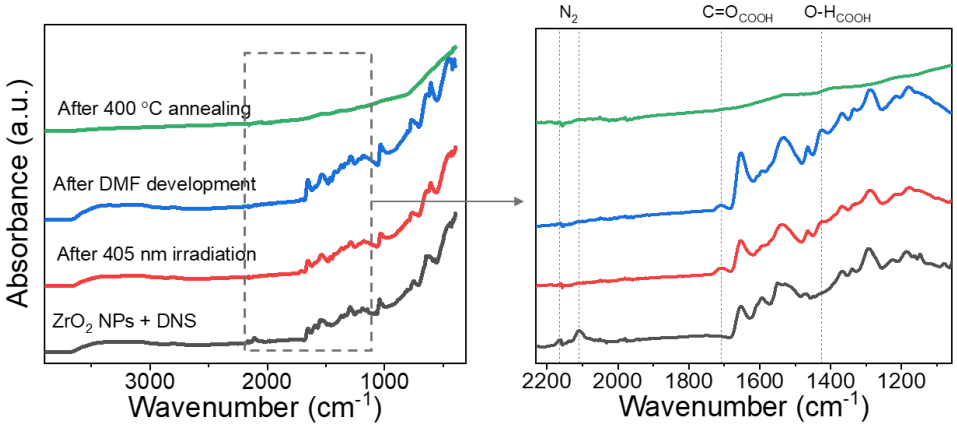

Figure 3.6. FTIR spectra of ZrO_2-DNS films before irradiation, after irradiation, after development, and after annealing at 400 °C.

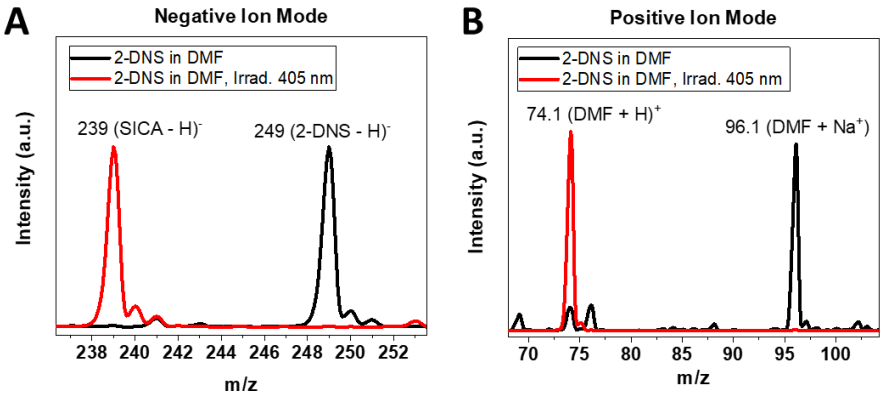

Figure 3.7. Electrospray ionization mass spectroscopy (ESI-MS) of 2-DNS in DMF before and after irradiation. (A) Negative and (B) positive ion mode spectra.

To understand how the photoconversion of DNS to SICA decreases NP film solubility, we further investigated the chemical and physical changes that occur during this process. It is well-known that the photodecomposition of DNQ-4-sulfonate esters results in a significant increase in acidity.[33] In the case of DNS, ESI-MS measurements in the positive mode revealed a significant increase in the $(DMF\text{-}H)^+$ to $(DMF\text{-}Na)^+$ ratio after irradiation of 2-DNS (**Figure 3.7B**). Na^+ ions leached from glassware and present in solvents are commonly detected in ESI-MS. This appreciable increase in the protonation of DMF means that the acidity of the solution has increased. In other words, SICA is a stronger Brønsted–Lowry acid than DNS, which allows it to protonate DMF. Based on the calculation of pK_a values using the ARChem SPARC software,[39-40] we found that the increase in acidity can be attributed to the ring hydrogen in SICA, which has a significantly lower pK_a value than both sulfonic and carboxylic acid hydrogens (**Figure 3.8**).

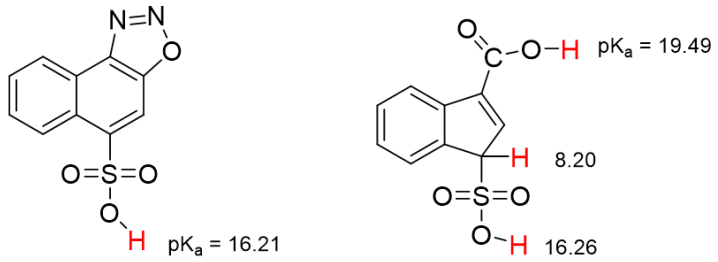

Figure 3.8. Calculated microscopic pK_a values of acidic protons of DNS-like compound (left) and SICA (right) in a solvent of DMF. Calculation was done using the SPARC online calculator[39-40].

Although our experimental and theoretical results support an increase in acidity upon photodecomposition of DNS into SICA, they do not prove that this acidity change is primarily responsible for the solubility change of the NPs. To probe this link, we carried out control experiments with two commercial photoacid generators (PAGs)—an ionic PAG and a nonionic PAG—that decompose under 365 nm light to produce strong acids (**Figure 3.9**). When either of these two PAGs were used in replacement of DNS (at the same molar concentration), areas of the

film that were exposed to light increase in solubility, which is distinctively different than the behavior of NP–DNS films. Thus, we infer that although the DNS to SICA conversion increases the acidity of the film, this effect is probably not the primary reason for the solubility reduction of the oxide NPs.

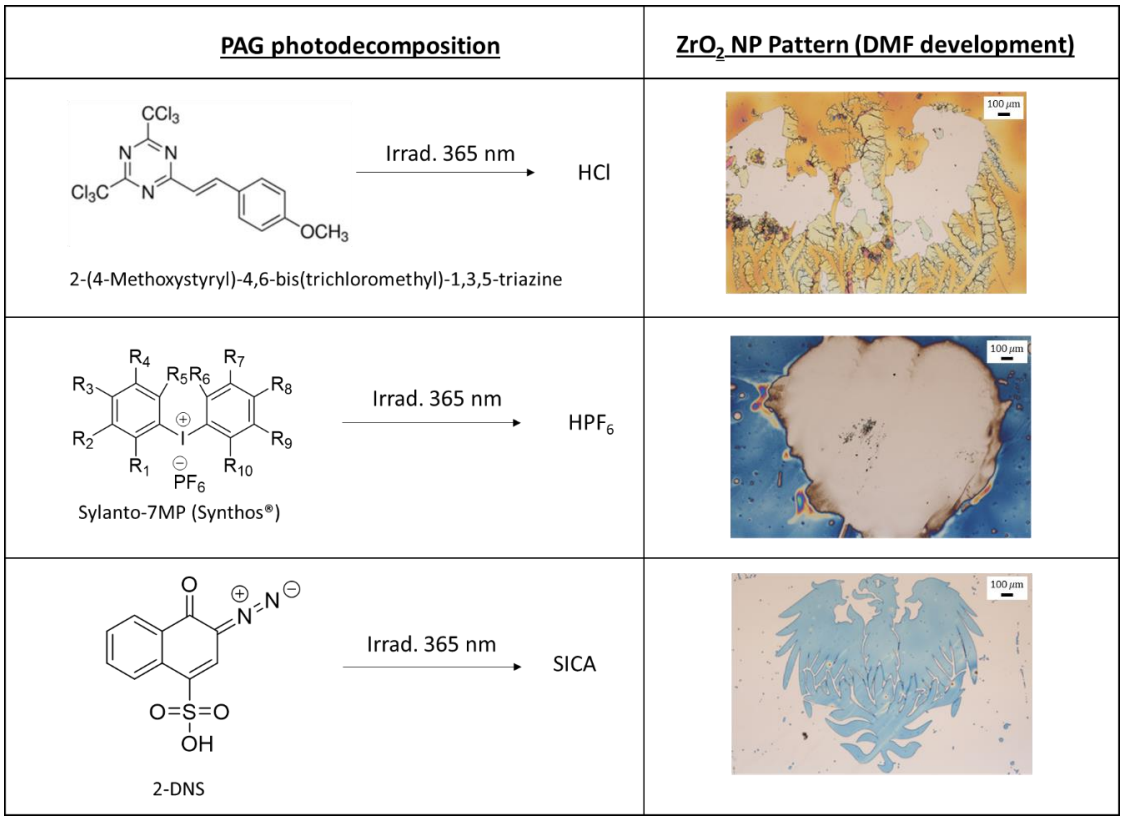

Figure 3.9. Patterns formed by mixing ZrO_2 NPs with two other photoacid generators in comparison with 2-DNS.

Another patterning mechanism which we considered involves the release of heat during the conversion of DNS into SICA. This conversion includes a highly exothermic Wolff rearrangement (−65 kcal/mol) that has been predicted to increase the local temperature up to 200 °C.[41] Such highly localized hot spots could promote chemical reactions in the film, such as the condensation of surface hydroxyl groups into Zr-O-Zr interparticle bonds that reduce film

solubility. To determine the importance of this effect, we carried out a control experiment by adding pre-irradiated DNS (i.e. SICA) to a solution of NPs (**Figure 3.10**). This resulted in an immediate gelation of the NP solution, which means that the heat release is not essential for pattern formation. However, this heat release may affect the diffusion rate of SICA, which has implications for the line edge roughness and ultimate resolution of this patterning approach.

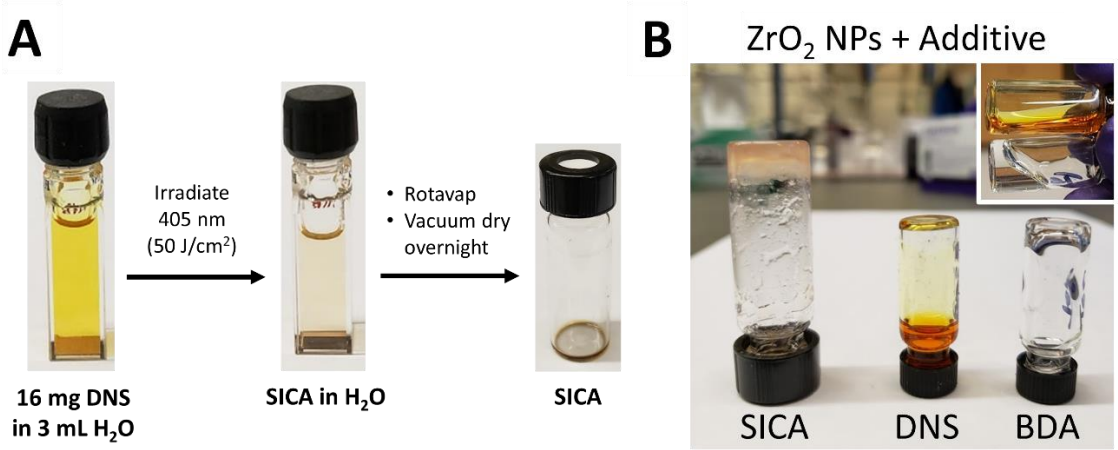

Figure 3.10. Control mechanism studies with pre-irradiated DNS (SICA) and benzene-1,4-dicarboxylic acid (BDA). (A) Process of obtaining SICA. (B) Photographs of amorphous ZrO_2 NP solutions (13.7 wt%) upon the addition of SICA, DNS or BDA (0.136 M). Inset: NP solutions with DNS and BDA showing the much higher viscosity (slow flow) of the BDS-NP solution.

Finally, we considered the differences in the way DNS and SICA interacts with the NP surface. The decomposition of DNS into SICA involves a conversion of diazo and oxo groups into a carboxylic acid group, which has strong affinity to NP surfaces acting as an X-type ligand. This causes SICA to bind more strongly to NP surfaces, inhibiting the formation of electrostatic double-layer repulsive interactions upon reintroduction of the DMF solvent. This effect is supported by a significant decrease in the zeta potential of the NPs upon photoirradiation of DNS (**Figure 3.4B**). Furthermore, the presence of two potential binding sites (the sulfonic and carboxylic acid groups) in SICA allows it to serve as a crosslinker between two NPs, further cementing the NPs in place.

As a control, we added an equimolar of benzene-1,4-dicarboxylic acid (BDA) to a solution of NPs and observed that the solution had a significantly higher viscosity than a DNS-NP solution, but did not gel like the SICA-NP solution (**Figure 3.10B**). Hence, our studies support a patterning mechanism involving the significant increase in binding and cross-linking ability when DNS photo-decomposes into SICA.

3.5. Direct optical lithography of oxide NPs with DNS.

The direct patterning of oxide NPs with DNS was found to be generalizable across various types of NPs, provided that the NPs have good colloidal stability and form smooth films upon spincoating. **Figure 3.11** shows optical microscope images of direct optically patterned amorphous and tetragonal ZrO_2 NPs, anatase TiO_2 NPs, monoclinic HfO_2, and cubic ITO NPs (the X-ray diffraction spectra of lab synthesized NCs are shown in **Figure 3.12**). All these patterns result from a pronounced decrease in NP solubility in regions that were exposed to 405 nm light. We also demonstrated the patterning of other non-transparent and semiconducting NCs such as CeO_2 and CdSe NCs (**Figure 3.13**). **Figure 3.13B** compares the absorption spectra of CdSe-Sn_2S_6 NCs before and after they were mixed with DNS. The first excitonic peak shows almost no changes indicating the CdSe NCs retain their mean size and monodispersity.

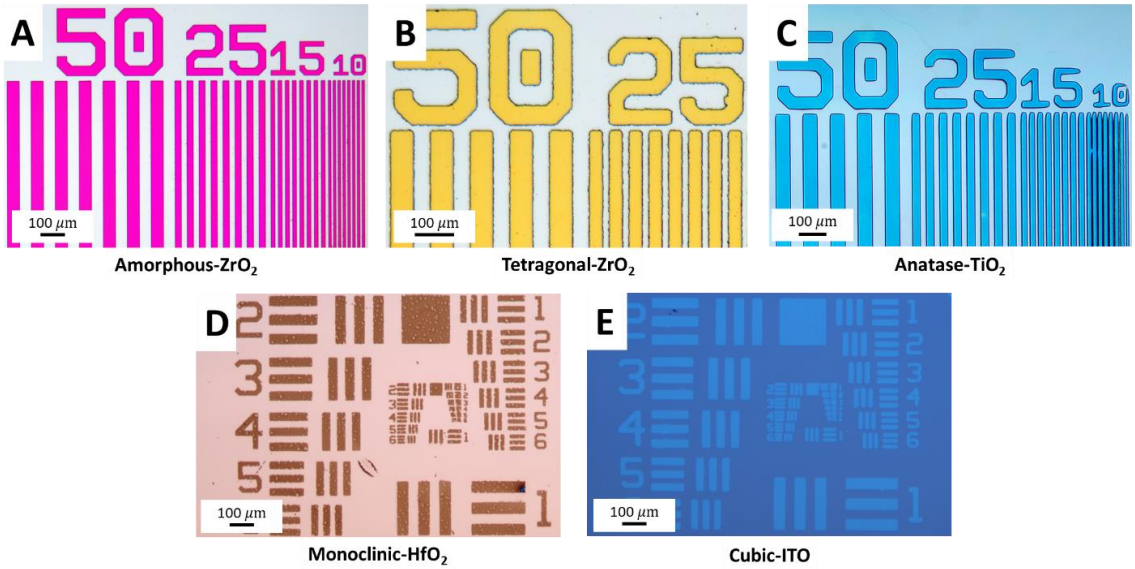

Figure 3.11. Optical microscope images of various oxide NPs optically patterned using DNS. (A) Amorphous ZrO_2 NPs, (B) tetragonal phase ZrO_2 NPs, (C) anatase TiO_2 NPs, (D) monoclinic HfO_2 NPs, and (E) cubic phase indium tin oxide NPs.

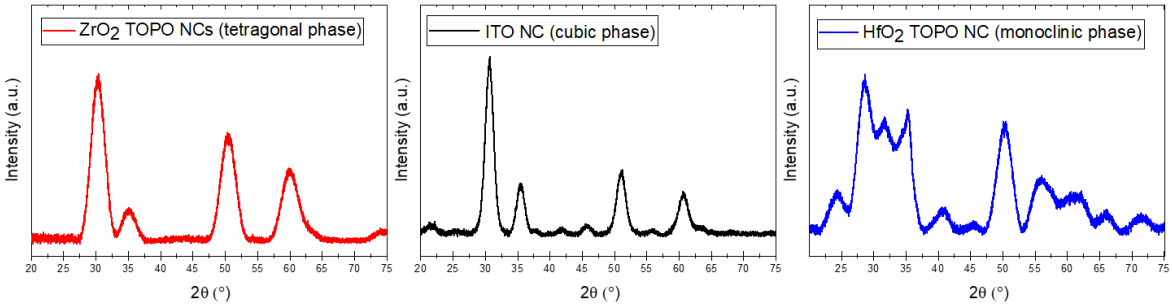

Figure 3.12. Powder XRD data of the synthesized ZrO_2, ITO and HfO_2 NCs.

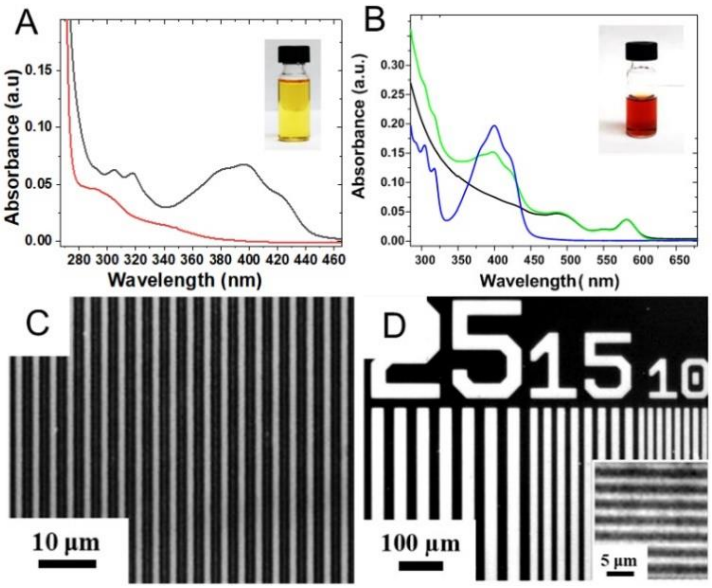

Figure 3.13. DOLFIN patterning with 405 nm photons. Absorption spectra of (A) DNS ligands in DMF before (black) and after photodecomposition (red), and (B) Wz-CdSe- Sn_2S_6 NCs before (black) and after (green) mixing with DNS. Inset: (A) DNS salts and (B) DNS based CdSe-Sn_2S_6 NCs ink in DMF. Optical microscopy images of equal spacing strips patterns obtained from DNS based "bare" CeO_2 NCs ink (C) and CdSe-Sn_2S_6 NCs ink (D) using 405 nm photons.

For more in-depth studies, we chose amorphous ZrO_2 NPs as our model system due to ease of processability and pattern robustness across a variety of parameters. The NPs can be patterned on glass or silicon wafers using a variety of exposure wavelengths (365 nm, 375 nm, 405 nm, and 450 nm) and exposure systems (LED light through a chrome mask, maskless laser writer, and LED display). We carried out resolution and thickness tests of the amorphous ZrO_2 NP patterns (**Figure 3.14**). The smallest pattern feature size was 1.2 μm lines (**Figure 3.14A**), limited by the resolution of our direct laser writer. The exposure doses were comparable to those used for commercial DNQ resists,[42] with a 500 nm thick film of ZrO_2 NPs requiring a minimum dose of <100 mJ/cm^2.

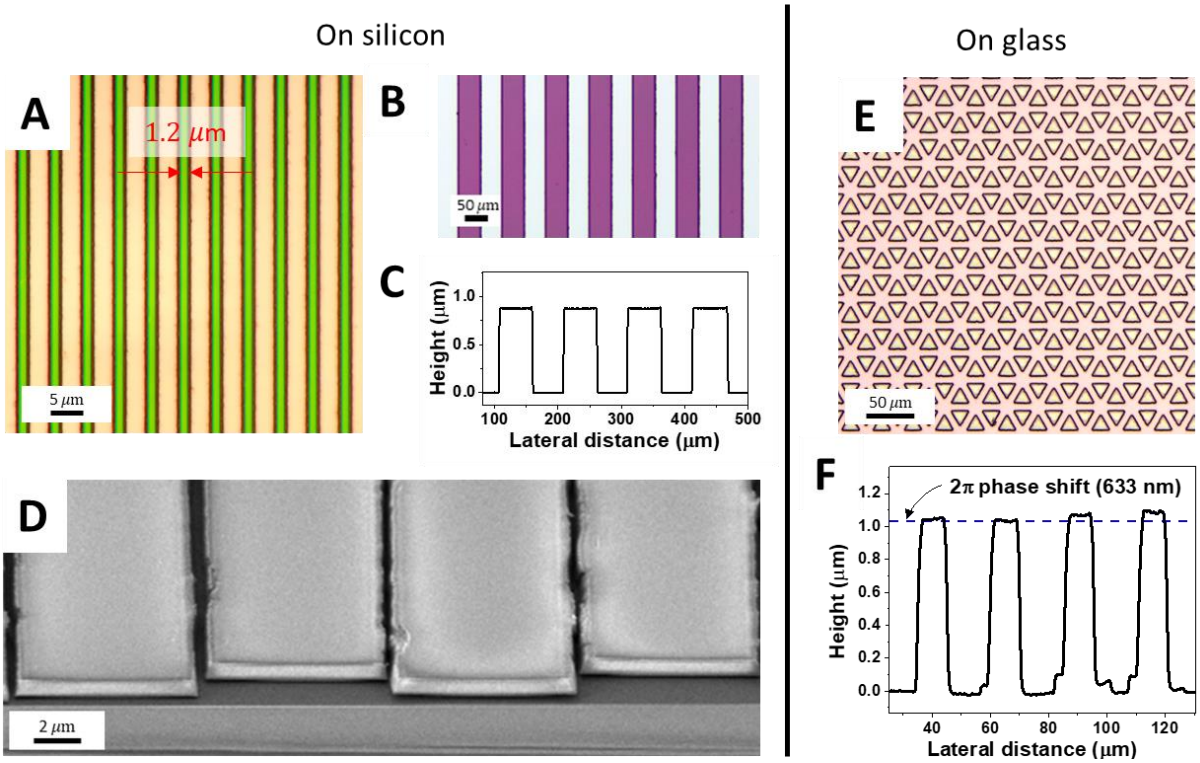

Figure 3.14. Resolution and thickness tests of single-layer amorphous ZrO_2 NPs patterns on silicon and glass substrates. Optical microscope images (A, B, E) and profilometer heights (C, F) of the patterns. The dotted line in (F) indicates the height required for a material with $n = 1.61$ to induce a 2π delay in the phase of 633 nm light. (D) Tilted SEM image of thick (overexposed) patterns.

With regards to thickness, we patterned structures that are sufficiently thick to allow for 2π phase delay of visible light. The thickness, t, required to shift the phase of incident light by 2π is given by $t = \lambda/(n-1)$, where n is the refractive index of the material and λ is the light wavelength in vacuum.[43] With an ellipsometer, we determined the refractive index of an amorphous ZrO_2 film to be around $n = 1.6$ at $\lambda = 633$ nm, which gives a thickness requirement of about 1 μm. With that in mind, we successfully deposited and patterned amorphous ZrO_2 NP layers that were routinely thicker than 800 nm and even beyond 1 μm (**Figure 3.14B,C,F**). The patterns on glass surpass the requirement for 2π phase control in the visible (dotted line **Figure**

3.14F), demonstrating the viability of this approach for the fabrication of diffractive optical elements with full control over the phase of light.

The deposition of thick NP layers in a single step is often found to be challenging due to internal stresses during film drying which leads to cracking.[44] Still, there have been reports showing the deposition of smooth NP films that are several micrometers thick.[45] To prepare patterns of thick NP films, we optimized both the NP solution processing and the deposition parameters. One straightforward way to increase film thickness is by increasing NP concentration. However, this needs to be done while maintaining good colloidal stability. We found that higher NP concentrations were attainable by introducing a hexane washing step before the final dispersion of NPs in DMF. This additional washing step extracts the residual toluene that was previously added as a nonsolvent to precipitate the NPs. Since hexane is immiscible with DMF and the NPs, it simply evaporates away after the final dissolution of NPs in DMF. This allows significantly higher NP concentrations to be formulated. Also, we found that infrared heating during spincoating helped in the formation of smooth and thick NP films. Besides increasing the solvent evaporation rate, the increased temperature may also relax the internal stresses in the film, reducing its susceptibility to cracking.

We also evaluated the capability of our approach for multilayer patterning (**Figure 3.15**). The process of deposition, irradiation, and development can be done repeatedly on the same substrate in a layer-by-layer fashion (**Figure 3.15**). Using inks with different NP concentrations for each layer, oxide patterns of varying heights should be attainable. Layers can even be deposited on top of each other, allowing a total of $(2^n - 1)$ height variations to be obtained after n number of patterned layers. As proof of this concept, we patterned a multicolored parrot image by depositing pixels of three different heights with only two deposition steps (**Figure 3.15B–D**). The

height of each pixel was chosen such that thin-film interference produced the desired color (magenta ~ 420 nm, green ~ 350 nm, and blue ~ 70 nm, measured by profilometry). This should be extendable to many more layers, allowing it to be used for devices with variations in topography, such as blazed diffraction gratings or colored printing.

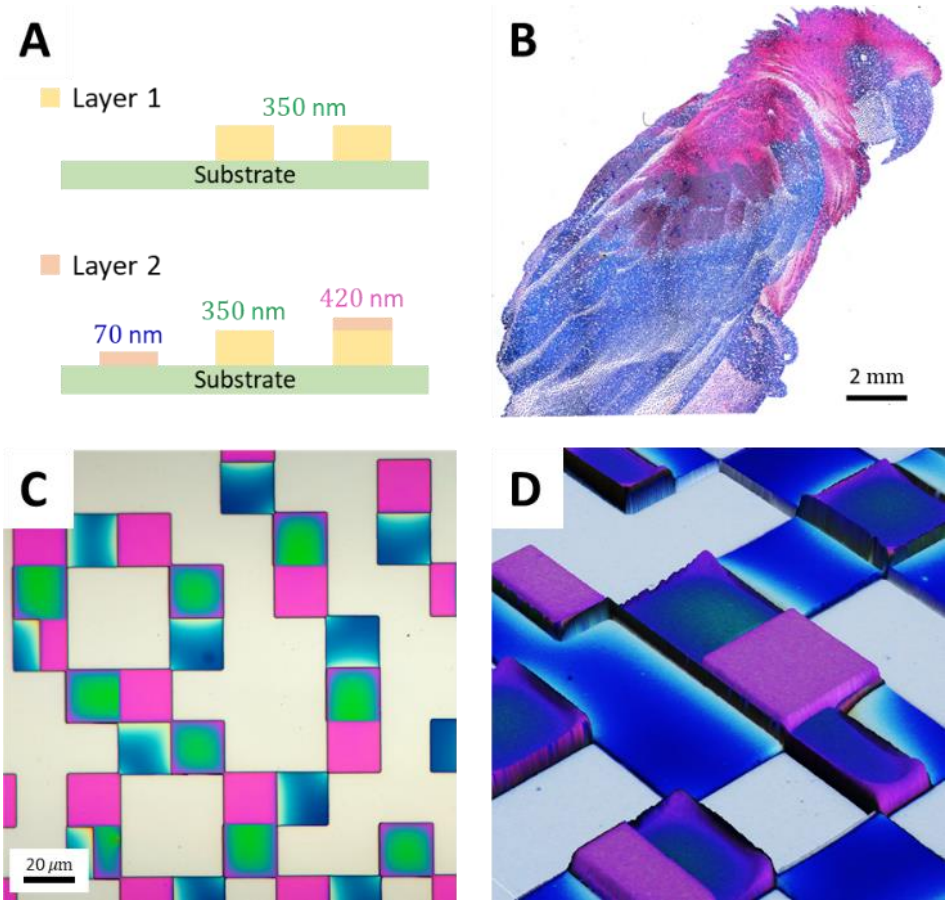

Figure 3.15. Multilayer direct patterning of oxide NPs. (A) Schematic of two-layer direct patterning process to obtain pixels with three different heights. (B–D) Fabrication of a colored parrot image by patterning two layers of amorphous ZrO_2 NPs. Low-magnification (B) and high-magnification (C) optical microscope images. (D) Three-dimensional height profile from a confocal optical microscope.

3.6. Characterization of amorphous ZrO_2 NP-SICA films.

We evaluated the chemical, thermal and optical properties of ZrO_2 NP–SICA films. After deposition and irradiation with 405 nm light, the films have good transparency in the visible and near-IR regions (**Figure 3.16A**, red). However, there are strong mid-IR absorbing peaks due to SICA (1710 cm^{-1}, 1426 cm^{-1}) and Zr–OH (3370 cm^{-1}, 1370 cm^{-1}), which remain even after DMF development (**Figure 3.16B**, red and **Figure 3.6**). Annealing at 400 °C decomposes most of the SICA from the film and condenses the Zr–OH groups into new Zr–O–Zr bonds (500–1000 cm^{-1}, broad). Nevertheless, annealing is insufficient to induce crystallization of the ZrO_2 as indicated by purely amorphous powder X-ray diffraction (XRD) peaks (**Figure 3.17**).

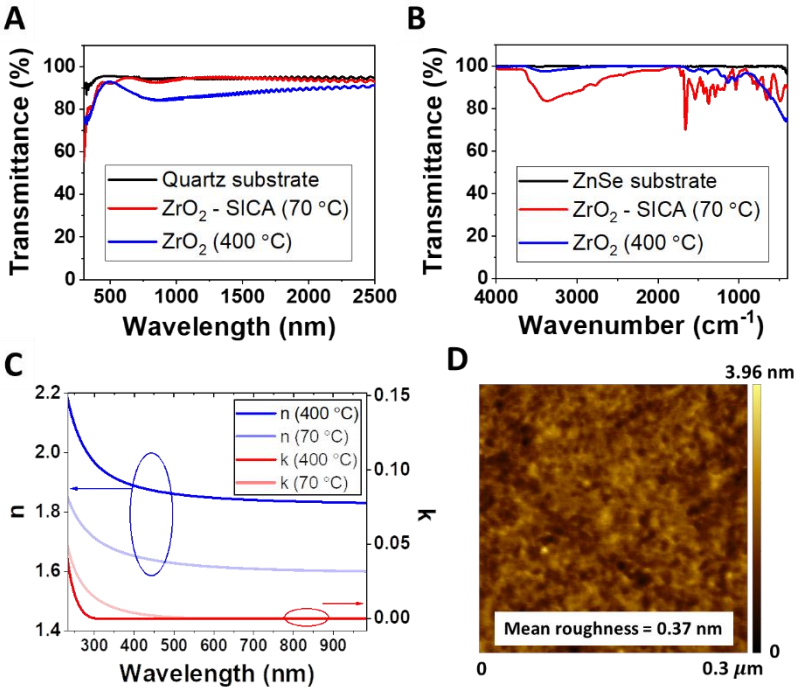

Figure 3.16. Optical and surface roughness characterization of amorphous ZrO_2 NP–SICA films. Film transmission spectra in the visible and near-IR regions (A) and in the mid-IR region (B). (C) Real and imaginary parts of the refractive index obtained by fitting spectroscopic ellipsometry data to a Tauc–Lorentz model. (D) Atomic force microscopy image after annealing the film at 400 °C.

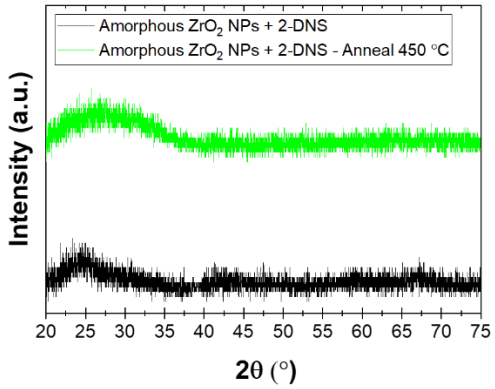

Figure 3.17. Powder XRD data of amorphous ZrO_2 NPs mixed with 2-DNS before and after annealing at 450 °C.

The result of the thermal treatment is an oxide layer that is highly transparent across a broad range of wavelengths, from 300 nm to 10 μm (**Figure 3.16A,B**, blue). The oscillations in the transmittance spectrum of the annealed film (e.g., the dips around 300 nm and 750 nm) can be attributed to thin-film interference effects, which is supported by good agreement of the measured transmission data with optical modeling using the transfer matrix method (**Figure 3.18**).

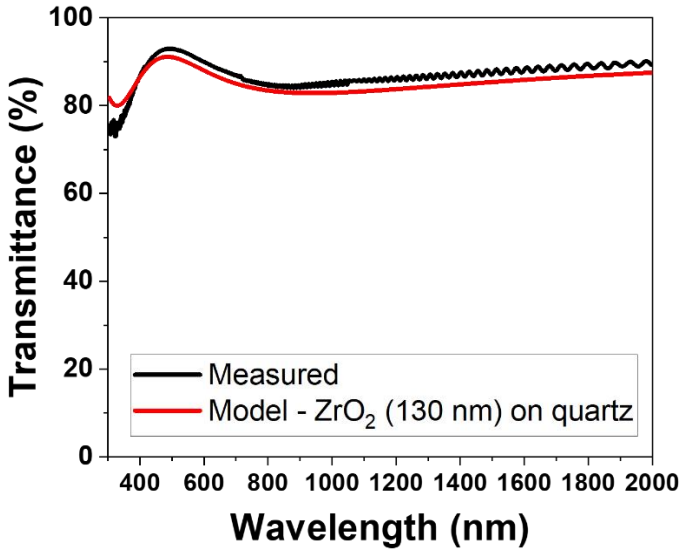

Figure 3.18. Measured and modeled data of a ZrO_2 film on a quartz substrate. The optical constants (n and k) for the ZrO_2 layer were obtained from our spectroscopic ellipsometry measurements (**Figure 3.16C**). The modeling used the transfer-matrix method with MATLAB code originally written by the McGehee group, which is freely available.[46-47]

The optical n and k constants of ZrO_2 NP films before and after annealing were obtained by spectroscopic ellipsometry, with the oxide layer modeled by the Tauc–Lorentz dispersion formula showing good fits with low χ^2 values between the model and experimental data (**Figure 3.16C** and **Figure 3.19**). The results show that annealing at 400 °C increases the refractive index of the film by about $\Delta n = 0.2$ throughout the visible region. The refractive index of the annealed ZrO_2 layer is still lower than that of ZrO_2 deposited by atomic layer deposition (n = 1.84 *vs.* n = 2.1 @ 633 nm),[48] which shows that the NP film is not fully densified. This is common for solution-deposited oxides, but methods such as high-pressure annealing can be used to achieve full densification.[49] We also measured the mean surface roughness of the annealed ZrO_2 film to be 0.37 nm by atomic force microscopy (AFM) (**Figure 3.16D**). This should allow for minimal scattering loses, which further reinforces the suitability of our patterned films for high-efficiency optical applications.

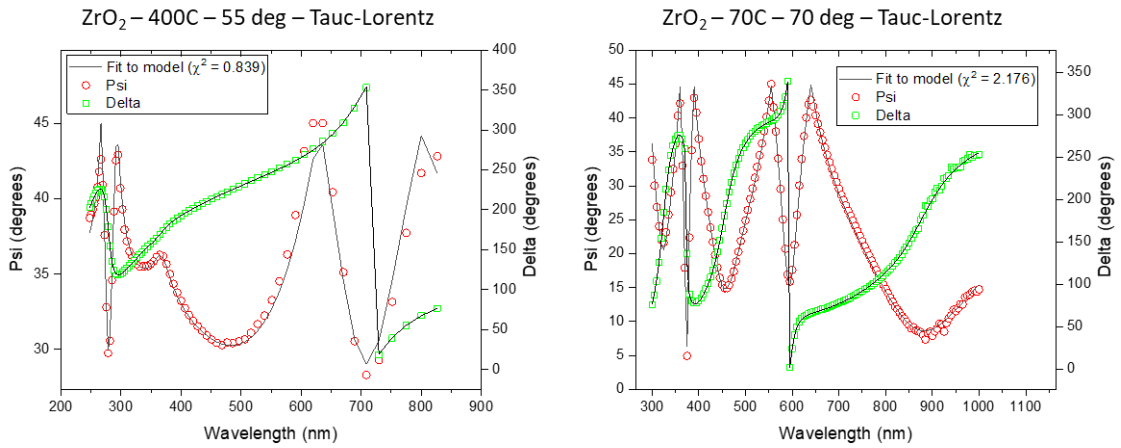

Figure 3.19. Fits of the spectroscopic ellipsometry data to a Tauc–Lorentz model for the oxide layer.

3.7. Fabrication and testing of oxide NP gratings

As a proof-of-concept, we fabricated and tested diffractive optical elements (DOEs) made with patterned ZrO_2 NPs. DOEs are optical devices that spatially shape the wavefront of propagating light. One of the simplest DOEs is the one-dimensional diffraction grating, which consists of a periodic pattern of stripes that either block light (amplitude gratings) or retard its phase (phase gratings). These changes lead to constructive and destructive interference in the far-field and the formation of bright spots on a screen (**Figure 3.20A**). Phase gratings are attractive due to their higher diffraction efficiencies, η_n, defined as the ratio of the power channeled into the n-th order diffraction peak to the incident light power. Without considering Fresnel reflections, an ideal binary (two-level) phase grating can channel 40.5% of the incident power into each of the ± 1 diffraction order.[50] This is achieved when the grating has exactly equal stripe and spacing widths, with each stripe retarding the phase of light by exactly π.

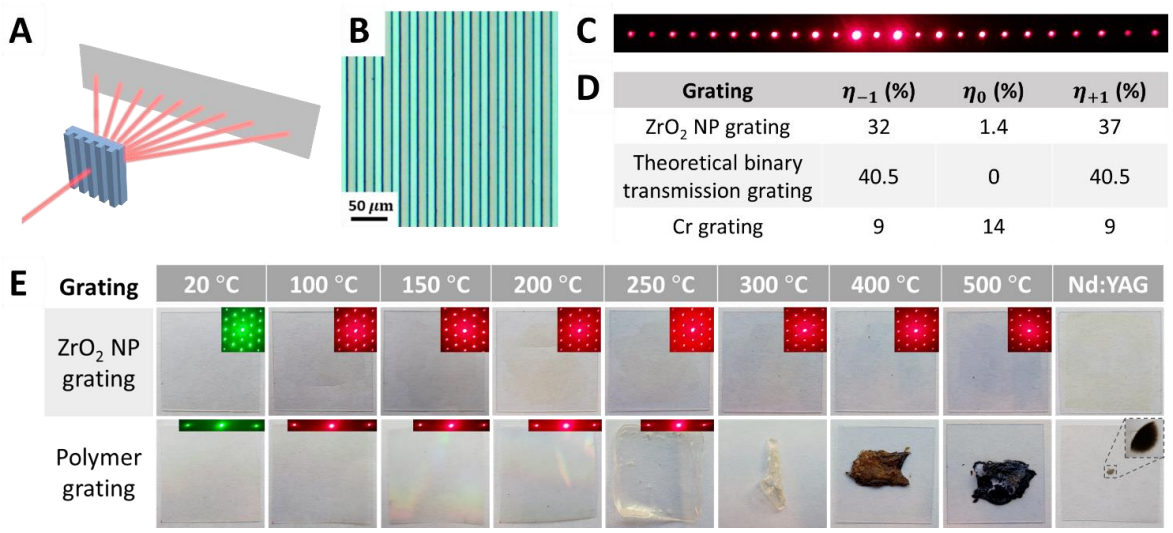

Grating	η_{-1} (%)	η_0 (%)	η_{+1} (%)
ZrO_2 NP grating	32	1.4	37
Theoretical binary transmission grating	40.5	0	40.5
Cr grating	9	14	9

Figure 3.20. Characterization of diffraction gratings made by patterning amorphous ZrO_2 NPs. (A) Schematic showing the diffraction of a laser beam through a one-dimensional (1D) grating. Optical microscope image of a 1D ZrO_2 NP grating (B) along with its diffraction pattern (C) and grating efficiencies (D). The efficiencies of an ideal binary phase grating (theoretical) and a chromium grating are shown for comparison. (E) Thermal stability and laser tolerance of a ZrO_2 NP grating compared to a polymer grating. Thermal stability tests involved 10 minutes of heating on a hot plate, while the laser test involved a 5 second exposure to the second harmonic generation (532 nm) of a pulsed Nd:YAG laser (10 Hz, ~25 mJ/pulse). Insets: Diffraction patterns produced by the gratings.

We patterned ZrO_2 NPs stripes with 25 μm line and spacing widths on a glass cover slip (**Figure 3.20B**). Upon illumination with a red laser light ($\lambda = 650$ nm), a diffraction pattern with many visible diffraction orders was produced (**Figure 3.20C**). To obtain quantitative diffraction efficiencies, we measured the zeroth and first order spots with a silicon detector and found that the $+1$ and -1 orders contain 37% and 32% of the incident light power respectively (the difference can be attributed to a small, nonzero angle of incidence), while the zeroth order spot contained less than 2% of the incident power (**Figure 3.20D**). These metrics are significantly better than that of a chromium amplitude mask (9% efficiencies for $+1$ and -1 diffraction orders) and should be improvable with further finetuning of the film thickness.

We also carried out thermal stability and laser tolerance tests on a ZrO_2 NP grating and compared its behavior to a commercial polymer grating (**Figure 3.20E**). The ZrO_2 NP grating was found to have good thermal stability up to the highest tested temperature of 500 °C, as shown by good optical transparency and clear diffraction patterns. It also was not visibly damaged upon irradiation upon a 5 s exposure to the second harmonic generation of a pulsed Nd:YAG laser at its maximum power. In contrast, the polymer grating began to warp around 150 °C and was completely unusable beyond 300 °C. It also visibly blackened upon exposure to the Nd:YAG laser. Thus, these ZrO_2 NP DOEs have good tolerance to high temperatures and high-powered lasers, which make them an appealing choice for applications that require such tolerance (e.g., gratings for distributed feedback lasers).

Besides that, we also fabricated diffraction gratings made of bare CeO_2 NCs that were patterned by the addition of the photosensitizer *N*-hydroxy-naphthalimide triflate (**Figure 3.21**). We demonstrate that both 1D and 2D diffraction gratings can be fabricated with good fidelity and showing many high-order diffraction spots.

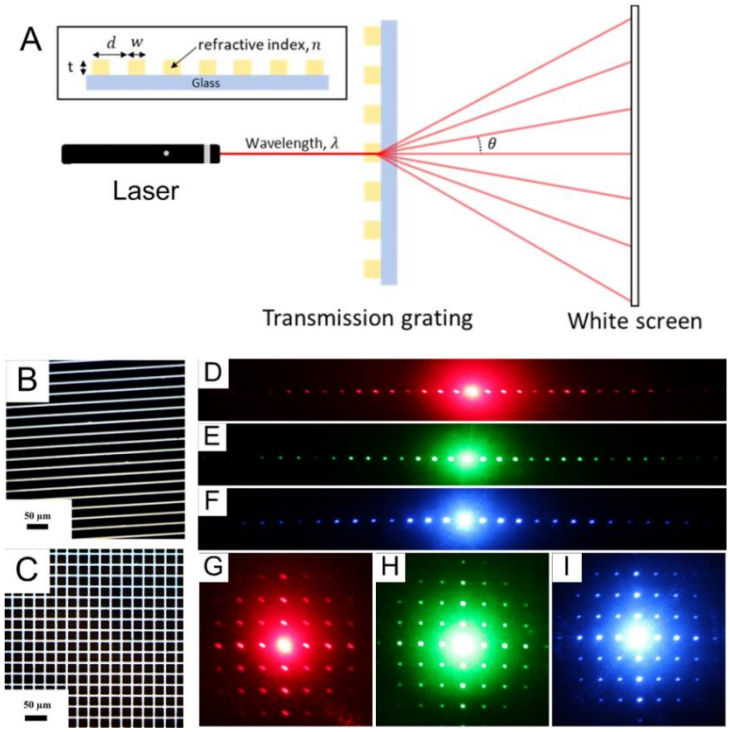

Figure 3.21. Patterning diffraction gratings made of CeO_2 NCs. (A) Diffraction grating scheme (Note: figures not drawn to scale). (B) Optical microscopy images of CeO_2 NCs in a 1D pattern. (D-F) Diffraction patterns obtained by illuminating 1D grating patterns with red, green, and blue CW laser. (C) Optical microscopy images of CeO_2 NCs in a 2D pattern. (G-I) Diffraction patterns obtained by illuminating 2D grating patterns with red, green, and blue CW lasers.

The direct photopatterning of oxide NPs should also find utility in many other applications besides the fabrication of DOEs. The facile patterning of ITO NPs will facilitate their usage as transparent conducting electrodes in optoelectronic devices. Recent advances have shown that the conductivity of solution-deposited ITO can approach that of films deposited by vapor deposition techniques.[51-52] Moreover, doped ITO NPs with their optical properties tunable by NP size and doping concentration are actively investigated for applications using localized surface plasmon resonance (LSPR).[53-54] Similarly, the ability to pattern TiO_2 NPs can have implications for photovoltaic, photocatalytic, and electrochromic applications by allowing the deposition of optimal patterns that allow for better performance and interfacing.[55-56]

3.8. Tunability and miscibility of oxide NPs for compositional and microstructural control.

A significant advantage in utilizing solution-phase NPs is the access to a large library of NPs with various optical, electrical, chemical, and thermal properties. Even NPs with the same chemical composition can have nuances in terms of their crystal phase, shape, and surface chemistries which influence their properties. For instance, highly crystalline NPs are already highly compacted, and their atoms do not significantly rearrange or further densify upon annealing. Thus, we found that patterns of tetragonal ZrO_2 NPs undergo no measurable shrinkage upon annealing at 390 °C (**Figure 3.22A**). During this process, the refractive index of the film does not significantly change ($n \sim 1.73$ @ 633 nm). Assuming the refractive index of ZrO_2 NPs is $n = 2.15$ and the gaps between them is air ($n = 1$), this gives a solid fraction of $\phi_{\mathrm{ZrO_2}} = 0.65$ by the symmetric Bruggeman effective medium approximation (or $\phi_{\mathrm{ZrO_2}} = 0.63$ by the volume-weighted index method),[57] which is close to the expected volume fraction of random closely packed spheres. In contrast, amorphous ZrO_2 NP patterns shrank by about 33% upon annealing at 400 °C (**Figure 3.22B**), along with a refractive index increase from $n = 1.61$ to $n = 1.84$ at 633 nm, as discussed previously. This increased refractive index can be attributed to rearrangement and condensation of Zr and O atoms, which allows the gaps between NPs to be filled. Besides differences in the crystal phases, various NP shapes can also be explored in the future, such as mesoporous ZrO_2 nanoframes.[58]

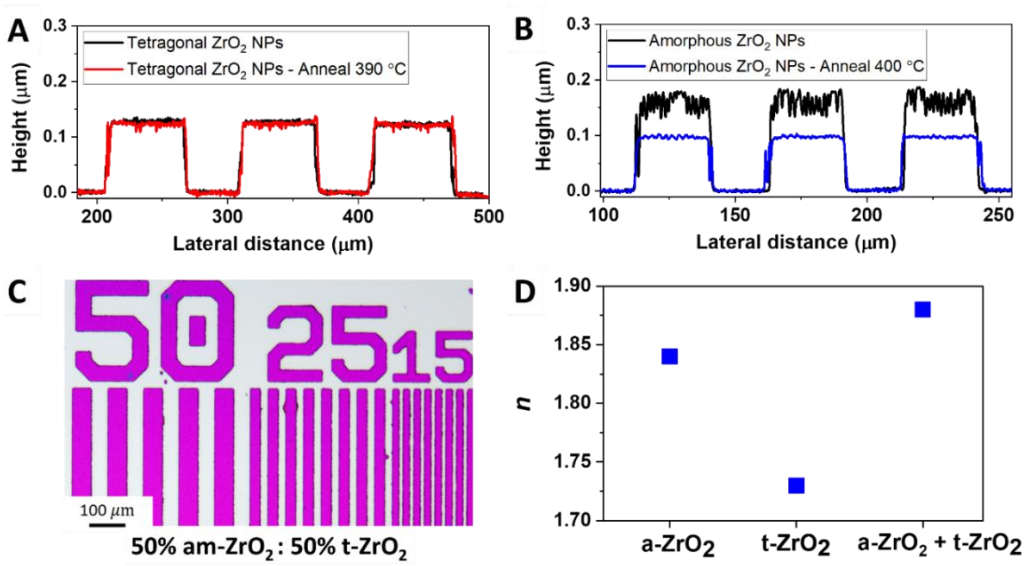

Figure 3.22. Pattering mixtures of NCs and NPs. Profilometer heights of patterned tetragonal phase ZrO_2 NPs (A) and amorphous ZrO_2 NPs (B) before and after annealing. (C) Patterns of a 50:50 mixture of amorphous ZrO_2 NPs and tetragonal ZrO_2 NPs. (D) Refractive indices, *n*, of films made from amorphous ZrO_2 NPs, tetragonal phase ZrO_2 NPs, and a 40:60 mixture of amorphous and tetragonal phase ZrO_2 NPs (all annealed at 450 °C).

Further tuning of the patterned oxide layers can be done using mixtures of NPs. This modular, "mix-and-match" approach can be used to synergistically combine the properties of two or more NPs in a way that leads to better performance than each individual component. To illustrate this concept, we patterned a mixture of amorphous ZrO_2 NPs and tetragonal phase ZrO_2 NPs (**Figure 3.22C**). We found that after annealing at 450 °C, layers containing a mixture of these two NPs have a higher refractive index ($n = 1.88$) compared to layers of tetragonal ZrO_2 NPs ($n = 1.73$) and amorphous ZrO_2 NPs ($n = 1.84$) on their own (**Figure 3.22D**). We hypothesize that this is due to the amorphous ZrO_2 filling in the gaps between the crystalline ZrO_2, forming what is commonly referred to as a "glass-ceramic".[59-60] Traditional approaches for the fabrication of glass-ceramic composites typically rely upon carefully controlled nucleation of crystals in a glassy matrix at high temperatures (often >1500 °C).[60] In contrast, our method allows for each

oxide component to be synthesized separately, mixed together in desired ratios and finally patterned directly under mild conditions. Thus, our approach utilizes the versatility and convenience of colloidal NPs in the facile fabrication of increasingly sophisticated metal oxide patterns. It is also worth mentioning that multiple components can be reliably co-integrated within individual NPs, e.g., in from of core-shell or dumbbell nano-heterostructures.[61-62]

3.9. Discussion on NPs that require more optimization.

Some oxide NPs require further optimizations of their ink formulation. For instance, NPs in basic aqueous solutions (e.g., with NH_4^+ counterions) or acidic NPs with stronger coordinating anions (e.g., Cl^-, acetate) do not easily form colloidal solutions in DMF upon solvent exchange. This could be attributed to the either a decrease in the dielectric constant (from 80 for water to 38 for DMF) or changes in the Hansen solubility parameters (i.e., dispersion, dipolar and hydrogen bonding forces) when exchanging H_2O for DMF. Also, since this pattering approach relies on DNS (about 1 nm in size) acting as a spacer between NPs, larger colloids (>50 nm) that are often formed in less controlled sol-gel syntheses would probably not work due to the significant increase in van der Waals attractive forces at small separations (**Figure 3.23**).

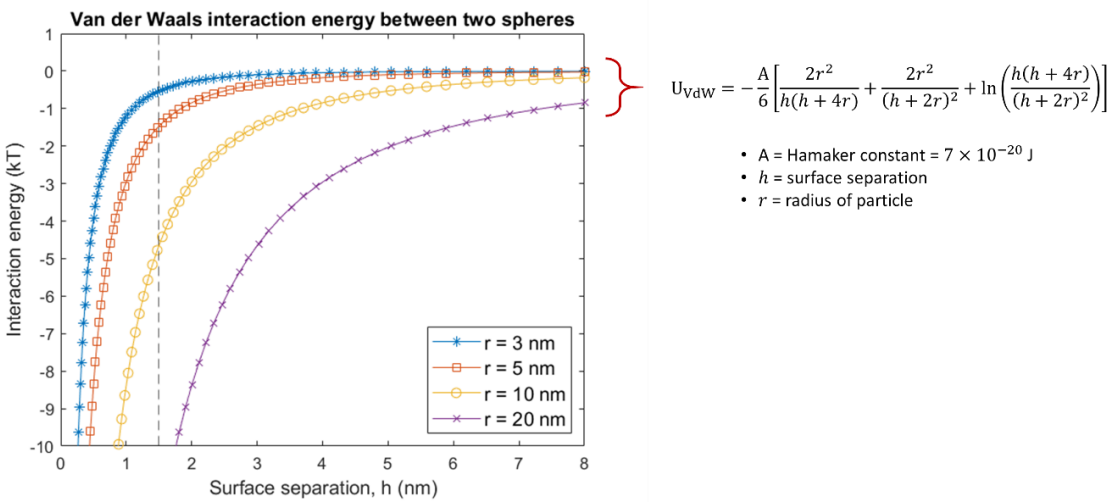

Figure 3.23. Plots of van der Waals interaction energy between two spheres. The size of two DNS molecules is roughly approximated to be 1.5 nm (from Chem3D) and is shown as a dotted line.

In other cases, NPs were successfully ligand-stripped with $NOBF_4$ and stabilized in DMF, but were not compatible with DNS. This leads to either the precipitation of NPs when DNS is added, or phase separation during spincoating (producing bad quality films that are not patternable). These effects occurred for TOPO-capped TiO_2 NPs, oleylamine-capped HfO_2 NPs, and oleylamine-capped ZrO_2 NPs. We attribute this to low surface charge densities leading to insufficient colloidal stability. In addition, we determined that residue long-chain organic ligands on the NP surface can also interfere with the pattern formation. We found that residue pyrophosphate after $NOBF_4$ stripping of TOPO-capped ZrO_2 NPs caused the NPs to remain soluble even after DNS to SICA photoconversion (**Figure 3.24**). By using harsher washing conditions which removed the bound pyrophosphate ligands, these NPs could be successfully patterned.

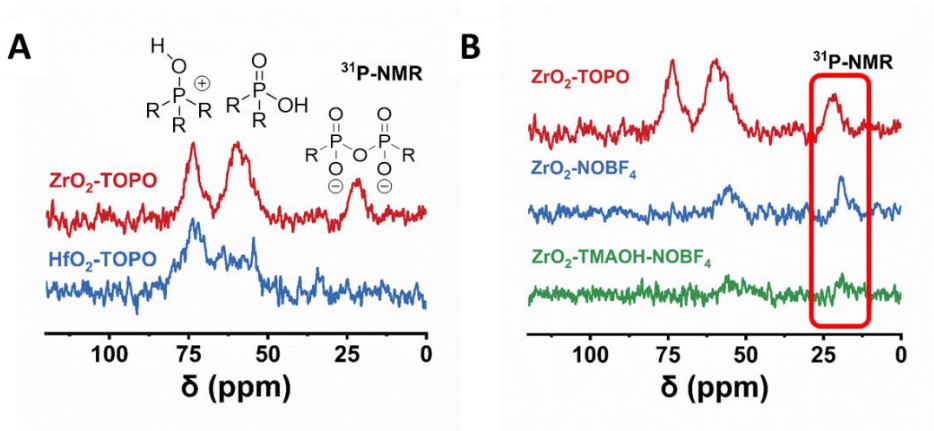

Figure 3.24. (A) ^{31}P-NMR spectra of ZrO_2-TOPO NPs and HfO_2-TOPO NPs as synthesized. (B) ^{31}P-NMR spectra of ZrO_2-TOPO NPs after different surface treatment procedures.

3.10. Conclusion

In summary, we developed a general approach for direct optical patterning of metal oxide NPs that is polymer-free and uses minimal organics, thus circumventing the limitations of inorganic–organic hybrid patterning methods. The photosensitive oxide inks were formulated by mixing various electrostatically stabilized oxide NPs with the photosensitive 1-diazo-2-naphthol-4-sulfonic acid in DMF. Thick layers (>1 μm) of amorphous ZrO_2 NPs can be patterned, allowing for 2π phase control of visible light. The oxide films have a high refractive index, good transparency across a wide wavelength range ($300\ \text{nm} - 10\ \mu\text{m}$), and low mean surface roughness. Multilayer patterning was also shown through the fabrication of a structurally colored parrot image by depositing pixels of different thickness. We then used this patterning platform to make efficient diffractive optical elements (e.g., diffractive gratings) that are thermally and optically robust. Finally, we demonstrated the ability to pattern mixtures of NPs, which allow for increased compositional variability and complexity.

3.11. Materials and methods.

Sources/syntheses of oxide nanoparticles. Amorphous ZrO_2 NPs with nitrate counterions (Zr10/15) were obtained as aqueous dispersions from Nyacol Nano Technologies, Inc. Titanium oxide NPs (Anatase, 15 wt %, 30 nm) were obtained from Nanostructured and Amorphous Materials, Inc.

Tin-doped indium oxide NPs capped with oleic acid/oleylamine were synthesized using a procedure by Lounis *et al*.[63] Briefly, In(acetate)$_3$ (1.02 mmol), Sn(ethylhexanoate)$_2$ (0.18 mmol), octanoic acid (3.6 mmol), and oleylamine (10 mmol) were mixed with 10 mL of octyl ether and degassed at 80 °C for 30 minutes. The temperature was then increased to 150 °C under N_2 and held there for 1 hour. The temperature was then further increased to 280 °C and held there for another 2 hours. The NCs were purified several times by ethanol and toluene.

Tetragonal zirconia NPs capped with TOPO were synthesized by a procedure by Joo *et al*.[18] Briefly, trioctylphosphine oxide (30 g) was degassed at 80 °C for 1 hour in a 3-neck round-bottom flask. The flask was sealed, brought into a glove box and Zr(O-iPr)$_4$·(IPA) (2.34 g, 6 mmol) and $ZrCl_4$ (1.75 g, 7.5 mmol) was added. The mixture was then degassed again at 70 °C for 30 mins. Under nitrogen, the solution was heated to 340 °C and held there for 2 hours. The NCs were purified several times by acetone and toluene.

Monoclinic HfO_2 NPs capped with TOPO were synthesized by a procedure by Tirosh et al.[64] Briefly, trioctylphosphine oxide (30 g) was degassed at 80 °C for 1 hour in a 3-neck round-bottom flask. The flask was sealed, brought into a glove box and Hf(O-iPr)$_4$·(IPA) (2.85 g. 6 mmol) and $HfCl_4$ (1.95 g, 6 mmol) was added. The mixture was then degassed again at 70 °C for 30 mins. Under nitrogen, the solution was heated to 360 °C and held there for 2 hours. The NCs were purified several times by acetone and toluene.

Preparation of NP-DNS ink

Nanoparticles in aqueous solution. For NPs colloidally stabilized by electrostatic interactions in water, a solvent exchange procedure to disperse NPs in DMF was developed. Using amorphous ZrO_2 NPs from Nyacol Nanotechnologies, Inc as an example, acetone (41 mL) was added to precipitate the ZrO_2 NP solution (13.4 wt %, 4 mL). The suspension was centrifuged and the pellet redispersed in DMF (8 mL), which was left to equilibrate overnight. The NPs were precipitated with the addition of toluene (17 mL) followed by centrifugation. The pellet was washed with hexane (15 mL) to remove residue toluene and then centrifuged. Finally, the pellet was dissolved in DMF at the desired concentration (>300 mg/mL achievable), with the help of vortexing, sonication and stirring. The NP solution was aged overnight before subsequent steps.

Organic-capped nanoparticles in nonpolar solvents. Organic-capped NPs were stripped of their native ligands by a modified $NOBF_4$ stripping method, by adding $NOBF_4$ in DMF (0.1 mL, ∼20 mg/mL) to NP solution (1 mL, ∼10 mg/mL). Flocculation of NPs was observed within a few seconds. The suspension was then vortexed and centrifuged. The supernatant was discarded and the pellet redispersed in DMF (0.1 mL), forming a clear solution. Toluene (1 mL) was added to precipitate NPs and the suspension was centrifuged. The redispersion, precipitation and centrifugation were repeated one more time. The pellet was vortexed with hexane (1 mL) to extract residual toluene and the formed suspension was centrifuged. Finally, the pellet was dispersed in DMF at the desired concentration (>100 mg/mL typically achievable).

Mixing nanoparticles with DNS. To obtain the photosensitive oxide ink, DNS was mixed (either directly as a solid or predissolved in DMF) with NP solution in DMF. The NP concentration was first determined by measuring the residue solid weight after drying about 100 μL of solution in a vacuum oven at 60 °C overnight. An amount of DNS between 1 and 25 wt % relative to the

dried NP weight was used depending on the type of NPs. The mixture needs to be aged for several hours to work properly in subsequent steps.

Direct photolithography using nanoparticle-DNS ink

Silicon substrates and glass cover slips were first cleaned by sonication in acetone (10 mins) and then in IPA (10 mins). They were then treated with O_2 plasma (> 10 mins) immediately prior to usage. The nanoparticle-DNS ink was then spincoated on a substrate with a rotation speed between 300 and 8,000 rpm. Then, selective-area light exposure was carried out by one of two methods: (1) a home-made contact lithography setup which involves clamping the substrate with a chrome mask using two binder clips and exposing with an LED light source (M405LP-C1-405 nm, Thorlabs, measured power density ∼30 mJ/cm^2) or (2) a maskless direct-write laser system (MLA150, 405/375 nm, Heidelberg Instruments) in a cleanroom. After exposure, the patterns were developed by immersing the substrate into the DMF developer solvent, rinsed with IPA, and blow dried with a N_2 gun.

For multilayer patterning, the above procedure was followed by a brief annealing step (e.g., 70 °C, 2 mins), followed by an O_2 plasma treatment before the next deposition step. For samples that required precise alignment between the first and second pattern steps, five crosshair alignment marks were patterned in the first step and used for the alignment during the second step using the MLA150 software.

There are several modifications of this procedure depending on the NPs used. For amorphous ZrO_2 NPs, a postexposure bake step (70 °C, 30s) is necessary, particularly for thick films. In some cases, immersing the substrate into a 2-methoxyethanol, 2-ME (for ∼10 s) prior to DMF development helps to reduce cracking of the patterned film.

3.12. Chapter bibliography.

1. Fortunato, E.; Barquinha, P.; Martins, R., Oxide semiconductor thin-film transistors: a review of recent advances. *Adv. Mater.* **2012,** *24* (22), 2945-2986.

2. Dai, J.; Ogbeide, O.; Macadam, N.; Sun, Q.; Yu, W.; Li, Y.; Su, B.-L.; Hasan, T.; Huang, X.; Huang, W., Printed gas sensors. *Chem. Soc. Rev.* **2020,** *49* (6), 1756-1789.

3. Kip, D., Photorefractive waveguides in oxide crystals: fabrication, properties, and applications. *Appl. Phys. B* **1998,** *67* (2), 131-150.

4. Yamada, I.; Ikeda, Y., Sol-gel zirconia diffraction grating using a soft imprinting process. *Appl. Opt.* **2017,** *56* (17), 5054-5059.

5. Devlin, R. C.; Khorasaninejad, M.; Chen, W. T.; Oh, J.; Capasso, F., Broadband high-efficiency dielectric metasurfaces for the visible spectrum. *Proc. Natl. Acad. Sci. U. S. A.* **2016,** *113* (38), 10473-10478.

6. Park, J.-S.; Zhang, S.; She, A.; Chen, W. T.; Lin, P.; Yousef, K. M. A.; Cheng, J.-X.; Capasso, F., All-Glass, Large Metalens at Visible Wavelength Using Deep-Ultraviolet Projection Lithography. *Nano Lett.* **2019,** *19* (12), 8673-8682.

7. Yeh, C. C.; Zan, H. W.; Soppera, O., Solution-Based Micro- and Nanoscale Metal Oxide Structures Formed by Direct Patterning for Electro-Optical Applications. *Adv. Mater.* **2018,** *30* (50), 1800923.

8. Kothari, R.; Beaulieu, M. R.; Hendricks, N. R.; Li, S.; Watkins, J. J., Direct Patterning of Robust One-Dimensional, Two-Dimensional, and Three-Dimensional Crystalline Metal Oxide Nanostructures Using Imprint Lithography and Nanoparticle Dispersion Inks. *Chem. Mater.* **2017,** *29* (9), 3908-3918.

9. Duoss, E. B.; Twardowski, M.; Lewis, J. A., Sol-Gel Inks for Direct-Write Assembly of Functional Oxides. *Adv. Mater.* **2007,** *19* (21), 3485-3489.

10. Su, M.; Liu, X.; Li, S.-Y.; Dravid, V. P.; Mirkin, C. A., Moving beyond Molecules: Patterning Solid-State Features via Dip-Pen Nanolithography with Sol-Based Inks. *J. Am. Chem. Soc.* **2002,** *124* (8), 1560-1561.

11. Jiang, J.; Chakrabarty, S.; Yu, M.; Ober, C. K., Metal oxide nanoparticle photoresists for EUV patterning. *J. Photopolym. Sci. Technol.* **2014,** *27* (5), 663-666.

12. Saifullah, M.; Subramanian, K.; Tapley, E.; Kang, D.-J.; Welland, M.; Butler, M., Sub-10 nm electron beam nanolithography using spin-coatable TiO2 resists. *Nano Lett.* **2003,** *3* (11), 1587-1591.

13. Kotz, F.; Arnold, K.; Bauer, W.; Schild, D.; Keller, N.; Sachsenheimer, K.; Nargang, T. M.; Richter, C.; Helmer, D.; Rapp, B. E., Three-dimensional printing of transparent fused silica glass. *Nature* **2017,** *544* (7650), 337.

14. Yee, D. W.; Lifson, M. L.; Edwards, B. W.; Greer, J. R., Additive Manufacturing of 3D-Architected Multifunctional Metal Oxides. *Adv. Mater.* **2019,** *31* (33), 1901345.

15. Jiang, C.; Lee, J.-S.; Talapin, D. V., Soluble Precursors for CuInSe2, CuIn1−xGaxSe2, and Cu2ZnSn(S,Se)4 Based on Colloidal Nanocrystals and Molecular Metal Chalcogenide Surface Ligands. *J. Am. Chem. Soc.* **2012,** *134* (11), 5010-5013.

16. Hench, L. L.; West, J. K., The sol-gel process. *Chem. Rev.* **1990,** *90* (1), 33-72.

17. Park, J.; Joo, J.; Kwon, S. G.; Jang, Y.; Hyeon, T., Synthesis of Monodisperse Spherical Nanocrystals. *Angew. Chem. Int. Ed.* **2007,** *46* (25), 4630-4660.

18. Joo, J.; Yu, T.; Kim, Y. W.; Park, H. M.; Wu, F.; Zhang, J. Z.; Hyeon, T., Multigram scale synthesis and characterization of monodisperse tetragonal zirconia nanocrystals. *J. Am. Chem. Soc.* **2003,** *125* (21), 6553-6557.

19. Kanehara, M.; Koike, H.; Yoshinaga, T.; Teranishi, T., Indium Tin Oxide Nanoparticles with Compositionally Tunable Surface Plasmon Resonance Frequencies in the Near-IR Region. *J. Am. Chem. Soc.* **2009,** *131* (49), 17736-17737.

20. Rodríguez, J. A.; Fernández-García, M., *Synthesis, properties, and applications of oxide nanomaterials*. John Wiley & Sons: 2007; p 379-713

21. Liu, J.-g.; Nakamura, Y.; Ogura, T.; Shibasaki, Y.; Ando, S.; Ueda, M., Optically transparent sulfur-containing polyimide− TiO2 nanocomposite films with high refractive index and negative pattern formation from poly (amic acid)− TiO2 nanocomposite film. *Chem. Mater.* **2007,** *20* (1), 273-281.

22. Loste, J.; Lopez-Cuesta, J.-M.; Billon, L.; Garay, H.; Save, M., Transparent polymer nanocomposites: An overview on their synthesis and advanced properties. *Prog. Polym. Sci.* **2019,** *89*, 133-158.

23. Trikeriotis, M.; Bae, W. J.; Schwartz, E.; Krysak, M.; Lafferty, N.; Xie, P.; Smith, B.; Zimmerman, P.; Ober, C.; Giannelis, E., *Development of an inorganic photoresist for DUV, EUV, and electron beam imaging*. SPIE: 2010; Vol. 7639.

24. Li, L.; Liu, X.; Pal, S.; Wang, S.; Ober, C. K.; Giannelis, E. P., Extreme ultraviolet resist materials for sub-7 nm patterning. *Chem. Soc. Rev.* **2017,** *46* (16), 4855-4866.

25. Jun, S.; Jang, E.; Park, J.; Kim, J., Photopatterned semiconductor nanocrystals and their electroluminescence from hybrid light-emitting devices. *Langmuir* **2006,** *22* (6), 2407-2410.

26. Wei, Y.; Li, X.; Chen, Y.; Cheng, Z.; Xiao, H.; Li, X.; Ding, J.; Lin, J., In Situ Light-Initiated Ligands Cross-Linking Enables Efficient All-Solution-Processed Perovskite Light-Emitting Diodes. *J. Phys. Chem. Lett.* **2020,** *11* (3), 1154-1161.

27. Hahm, D.; Park, J.; Jeong, I.; Rhee, S.; Lee, T.; Lee, C.; Chung, S.; Bae, W. K.; Lee, S., Surface Engineered Colloidal Quantum Dots for Complete Green Process. *ACS Appl. Mater. Interfaces* **2020,** *12* (9), 10563-10570.

28. Kim, W. J.; Kim, S. J.; Lee, K.-S.; Samoc, M.; Cartwright, A. N.; Prasad, P. N., Robust microstructures using UV photopatternable semiconductor nanocrystals. *Nano Lett.* **2008,** *8* (10), 3262-3265.

29. Zhu, J.; Lin, H.; Kim, Y.; Yang, M.; Skakuj, K.; Du, J. S.; Lee, B.; Schatz, G. C.; Van Duyne, R. P.; Mirkin, C. A., Light-Responsive Colloidal Crystals Engineered with DNA. *Adv. Mater.* **2020,** *32* (8), 1906600.

30. Wang, Y.; Fedin, I.; Zhang, H.; Talapin, D. V., Direct optical lithography of functional inorganic nanomaterials. *Science* **2017,** *357* (6349), 385-388.

31. Wang, Y.; Pan, J.-A.; Wu, H.; Talapin, D. V., Direct Wavelength-Selective Optical and Electron-Beam Lithography of Functional Inorganic Nanomaterials. *ACS Nano* **2019,** *13* (12), 13917-13931.

32. Talapin, D. V.; Lee, J.-S.; Kovalenko, M. V.; Shevchenko, E. V., Prospects of Colloidal Nanocrystals for Electronic and Optoelectronic Applications. *Chem. Rev.* **2010,** *110* (1), 389-458.

33. Dammel, R., *Diazonaphthoquinone-based resists*. SPIE press: 1993; Vol. 11.

34. Zhang, H.; Jang, J.; Liu, W.; Talapin, D. V., Colloidal nanocrystals with inorganic halide, pseudohalide, and halometallate ligands. *ACS Nano* **2014,** *8* (7), 7359-7369.

35. Dong, A.; Ye, X.; Chen, J.; Kang, Y.; Gordon, T.; Kikkawa, J. M.; Murray, C. B., A generalized ligand-exchange strategy enabling sequential surface functionalization of colloidal nanocrystals. *J. Am. Chem. Soc.* **2010,** *133* (4), 998-1006.

36. Nag, A.; Kovalenko, M. V.; Lee, J.-S.; Liu, W.; Spokoyny, B.; Talapin, D. V., Metal-free inorganic ligands for colloidal nanocrystals: S2–, HS–, Se2–, HSe–, Te2–, HTe–, TeS32–, OH–, and NH2–as surface ligands. *J. Am. Chem. Soc.* **2011,** *133* (27), 10612-10620.

37. Huang, J.; Liu, W.; Dolzhnikov, D. S.; Protesescu, L.; Kovalenko, M. V.; Koo, B.; Chattopadhyay, S.; Shenchenko, E. V.; Talapin, D. V., Surface functionalization of semiconductor and oxide nanocrystals with small inorganic oxoanions (PO43–, MoO42–) and polyoxometalate ligands. *ACS Nano* **2014,** *8* (9), 9388-9402.

38. Rodionova, G.; Yablokova, V.; Tuchin, Y. G.; Partalla, N.; Érlikh, R., Absorption spectra and structures of some o-naphthoquinone diazides. *J. Appl. Spectrosc.* **1989,** *51* (4), 1068-1071.

39. The ARChem SPARC Calculator. http://www.archemcalc.com/sparc-web/calc (accessed 3/2020).

40. Hilal, S. H.; Karickhoff, S. W.; Carreira, L. A., A Rigorous Test for SPARC's Chemical Reactivity Models: Estimation of More Than 4300 Ionization pKas. *Quant. Struct.-Act. Relat.* **1995,** *14* (4), 348-355.

41. Reiser, A.; Huang, J. P.; He, X.; Yeh, T. F.; Jha, S.; Shih, H. Y.; Kim, M. S.; Han, Y. K.; Yan, K., The molecular mechanism of novolak–diazonaphthoquinone resists. *Eur. Polym. J.* **2002,** *38* (4), 619-629.

42. Ellman, M.; Rodríguez, A.; Pérez, N.; Echeverria, M.; Verevkin, Y. K.; Peng, C. S.; Berthou, T.; Wang, Z.; Olaizola, S. M.; Ayerdi, I., High-power laser interference lithography process on photoresist: Effect of laser fluence and polarisation. *Appl. Surf. Sci.* **2009,** *255* (10), 5537-5541.

43. Khorasaninejad, M.; Capasso, F., Metalenses: Versatile multifunctional photonic components. *Science* **2017,** *358* (6367), eaam8100.

44. Prosser, J. H.; Brugarolas, T.; Lee, S.; Nolte, A. J.; Lee, D., Avoiding cracks in nanoparticle films. *Nano Lett.* **2012,** *12* (10), 5287-5291.

45. Lin, Q.; Yun, H. J.; Liu, W.; Song, H.-J.; Makarov, N. S.; Isaienko, O.; Nakotte, T.; Chen, G.; Luo, H.; Klimov, V. I., Phase-transfer ligand exchange of lead chalcogenide quantum dots for direct deposition of thick, highly conductive films. *J. Am. Chem. Soc.* **2017,** *139* (19), 6644-6653.

46. Burkhard, G. F.; Hoke, E. T.; McGehee, M. D., Accounting for Interference, Scattering, and Electrode Absorption to Make Accurate Internal Quantum Efficiency Measurements in Organic and Other Thin Solar Cells. *Adv. Mater.* **2010,** *22* (30), 3293-3297.

47. Hoke, E. T. Transfer Matrix https://github.com/erichoke/Stanford/blob/master/TransferMatrix_Matlab/TransferMatrix.m (accessed 11/23/2020).

48. Hausmann, D. M.; Kim, E.; Becker, J.; Gordon, R. G., Atomic layer deposition of hafnium and zirconium oxides using metal amide precursors. *Chem. Mater.* **2002,** *14* (10), 4350-4358.

49. Kim, S. J.; Yoon, D. H.; Rim, Y. S.; Kim, H. J., Low-temperature solution-processed ZrO2 gate insulators for thin-film transistors using high-pressure annealing. *Electrochem. Solid-State Lett.* **2011,** *14* (11), E35-E37.

50. Magnusson, R.; Gaylord, T. K., Diffraction efficiencies of thin phase gratings with arbitrary grating shape. *J. Opt. Soc. Am.* **1978,** *68* (6), 806-809.

51. Kim, B. H.; Staller, C. M.; Cho, S. H.; Heo, S.; Garrison, C. E.; Kim, J.; Milliron, D. J., High Mobility in Nanocrystal-Based Transparent Conducting Oxide Thin Films. *ACS Nano* **2018,** *12* (4), 3200-3208.

52. Lee, J.; Lee, S.; Li, G.; Petruska, M. A.; Paine, D. C.; Sun, S., A facile solution-phase approach to transparent and conducting ITO nanocrystal assemblies. *J. Am. Chem. Soc.* **2012,** *134* (32), 13410-13414.

53. Staller, C. M.; Gibbs, S. L.; Saez Cabezas, C. A.; Milliron, D. J., Quantitative Analysis of Extinction Coefficients of Tin-Doped Indium Oxide Nanocrystal Ensembles. *Nano Lett.* **2019,** *19* (11), 8149-8154.

54. Agrawal, A.; Cho, S. H.; Zandi, O.; Ghosh, S.; Johns, R. W.; Milliron, D. J., Localized Surface Plasmon Resonance in Semiconductor Nanocrystals. *Chem. Rev.* **2018,** *118* (6), 3121-3207.

55. Chen, X.; Mao, S. S., Titanium Dioxide Nanomaterials: Synthesis, Properties, Modifications, and Applications. *Chem. Rev.* **2007,** *107* (7), 2891-2959.

56. Zhang, S.; Cao, S.; Zhang, T.; Lee, J. Y., Plasmonic Oxygen-Deficient TiO2-x Nanocrystals for Dual-Band Electrochromic Smart Windows with Efficient Energy Recycling. *Adv. Mater.* **2020**, 2004686.

57. Cook, K. T.; Tettey, K. E.; Bunch, R. M.; Lee, D.; Nolte, A. J., One-step index-tunable antireflection coatings from aggregated silica nanoparticles. *ACS Appl. Mater. Interfaces* **2012,** *4* (12), 6426-6431.

58. Wang, H.; Chen, H.; Ni, B.; Wang, K.; He, T.; Wu, Y.; Wang, X., Mesoporous ZrO2 Nanoframes for Biomass Upgrading. *ACS Appl. Mater. Interfaces* **2017,** *9* (32), 26897-26906.

59. Fu, L.; Xie, L.; Fu, W.; Hu, S.; Zhang, Z.-B.; Leifer, K.; Engqvist, H.; Xia, W., Ultra-strong translucent glass ceramic with nanocrystalline, biomimetic structure. *Nano Lett.* **2018,** *18* (11), 7146-7154.

60. Beall, G. H.; Duke, D. A., Transparent glass-ceramics. *J. Mater. Sci.* **1969,** *4* (4), 340-352.

61. Hines, M. A.; Guyot-Sionnest, P., Synthesis and Characterization of Strongly Luminescing ZnS-Capped CdSe Nanocrystals. *The Journal of Physical Chemistry* **1996,** *100* (2), 468-471.

62. Yu, H.; Chen, M.; Rice, P. M.; Wang, S. X.; White, R. L.; Sun, S., Dumbbell-like Bifunctional Au−Fe3O4 Nanoparticles. *Nano Lett.* **2005,** *5* (2), 379-382.

63. Lounis, S. D.; Runnerstrom, E. L.; Bergerud, A.; Nordlund, D.; Milliron, D. J., Influence of dopant distribution on the plasmonic properties of indium tin oxide nanocrystals. *J. Am. Chem. Soc.* **2014,** *136* (19), 7110-7116.

64. Tirosh, E.; Markovich, G., Control of defects and magnetic properties in colloidal HfO2 nanorods. *Adv. Mater.* **2007,** *19* (18), 2608-2612.

Chapter 4. Direct optical lithography of $CsPbX_3$ nanocrystals via photoinduced ligand cleavage with post-patterning chemical modification and electronic coupling

Adapted with permission from J.-A. Pan *et al. Nano Lett.*, **2021**, *21*, 18, 7609-7616. Copyright 2021 American Chemical Society.

4.1. Introduction

Colloidal lead halide perovskite (LHP) nanocrystals (NCs) have been intensely investigated due to their facile solution-phase syntheses, defect tolerance, and fascinating optoelectronic properties.[1-4] LHP NCs have been researched for use in light emitting diodes (LEDs),[5-7] color conversion filters,[8] lasers,[9-11] solar cells,[12-13] visible-light photodetectors,[14] X-ray scintillators,[15-16] and quantum emitters.[17] As the library of LHP NCs and perovskite-related nanomaterials continue to expand toward increased complexity, there is a need to develop methods for integrating LHP NCs in practical devices. In particular, the NCs need to be controllably deposited as a two-dimensional pattern for proper interfacing with other electronic and photonic components. This patterning process is also required for the integration of LHP NCs in many display technologies.

Various approaches to patterning perovskite nanomaterials have been reported including micro/nano-imprinting,[18-19] ink jet printing,[20-21] X-ray lithography,[22] electron-beam lithography,[23] and photolithography. Among these techniques, photolithography is a particularly attractive route due to its high resolution, high throughput, and wide availability. Unfortunately, the ionic nature of LHP NCs typically makes them incompatible with traditional photolithography workflows that use polar solvents. To overcome this issue, modifications to either the NCs or the photolithography process have been explored such as using silica-encapsulated LHP NCs,[8] orthogonal fluorinated photoresist and developer,[24] and adding a self-healing recrystallization step.[9]

Alternatively, LHP NCs can be photopatterned directly by including a photosensitive component into the LHP NC solution (or LHP NC precursor solution). This can be done by using cross-linkable ligands,[25-28] embedding the LHP NCs in a monomer matrix that can be photo-polymerized,[29] or *in situ* crystallization of LHP NCs in an oxide/polymer matrix with a pulsed laser.[30-31] These approaches typically result in a patterned nanocomposite consisting of LHP NCs dispersed in an insulating matrix, which can be helpful for increasing the chemical stability of the LHP NCs. However, this process prevents electrical contact with the NCs, which is crucial for devices such as LEDs and photodetectors. Furthermore, the NCs in these nanocomposites are sealed off from further chemical manipulations such as ligand and ion exchanges. Also, the large separation between LHP NCs in a matrix would preclude any coherent coupling effects such as superfluorescence.[32-33]

We recently introduced a patterning approach for colloidal nanomaterials which we call direct optical lithography of functional inorganic nanomaterials (DOLFIN).[34-35] The DOLFIN approach involves the use of small-molecule photosensitizers that interact with the NC surface upon light exposure, allowing the solubility of the NCs to be modulated, forming micropatterns. We have used this framework to develop a library of photosensitive ligand chemistry for patterning semiconductor, dielectric, metallic and magnetic NCs. In parallel, we have demonstrated the fabrication of various high-performing patterned devices such as transistors, LEDs, and diffractive optical elements.[35-37] However, these methods typically involve polar solvents such as DMF and/or ligand-exchange reactions, both of which degrade LHP NCs.

Here, we explore the direct optical lithography of $CsPbBr_3$ and $CsPbBr_{3-x}Cl_x$ LHP NCs through a light-induced ligand cleavage mechanism. A photosensitive oxime sulfonate ester (–C=N–OSOO–) is first mixed with the NCs to displace some of the native ligands. Upon

irradiation of 405 nm light through a mask, the photosensitive ligand cleaves, rendering the NCs insoluble in toluene and resulting in micro-scale patterns. Post-patterning ligand exchange replaces the sulfonate ligand with more appropriate ligands that can better passivate the NC surfaces, increasing the absolute photoluminescence quantum yield (PLQY) of patterned films up to 76%. Furthermore, post-patterning anion exchange allows the emission wavelength to be tuned across the visible spectrum. Finally, we demonstrate that the patterned NC layer behaves as a photoconductor when illuminated with visible light. Together our results demonstrate a versatile process for patterning LHP NCs which are chemically and electronically accessible.

4.2. Direct optical patterning of $CsPbX_3$ NCs with oxime sulfonate esters

$CsPbBr_3$ NCs capped with oleic acid (OAc) and oleylamine (OAm) were prepared using a modified benzoyl halide hot injection method.[38] These NCs were then mixed with a solution of a photosensitive oxime sulfonate ester such as PA-480, which partially replaced the native ligands (**Figure 4.1**). This solution was then spin-coated to form a film, which was then irradiated with 405 nm light through a mask. This light exposure decomposes the photosensitive PA-480, reducing the solubility of the NCs in the toluene developer and results in a patterned film. Finally, the patterned films can be treated with a variety of solutions that allow for ligand and/or anion exchange.

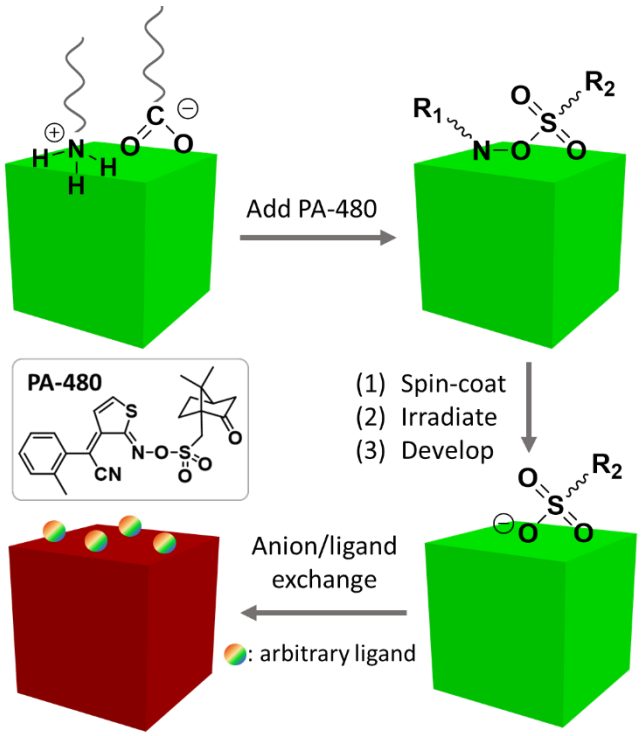

Figure 4.1. Outline of the processing steps for direct photolithography of $CsPbX_3$ LHP NCs with the photosensitive oxime sulfonate ester.

The patterned $CsPbBr_3$ NC films were visibly luminescent as viewed under a fluorescence optical microscope with features sizes as small as 1 µm (**Figure 4.2A–C**). However, the PLQY immediately after development with toluene was low (< 5%), which we attribute to the poor ability of the sulfonate ligand to passivate surface defects, combined with partial removal of labile surface ligands by excess toluene. Hence, we investigated the use of several solution-phase treatments to further improve the PLQY. Many chemical treatments to improve the PLQY of LHP NCs have been reported,[39-44] but we had to adapt these methods as a film-based treatment. We found that film-treatments had to be carried out in a non-solvent such as ethyl acetate to prevent redissolution of the patterned films. After screening several combinations of ligands and other additives, we found that two successive spin-coating treatments with an ethyl acetate solution of $PbBr_2$, octanoic acid (OctAc) and butylamine (BuAm) increased the film PLQY to 79% (**Figure 4.2E**). The PL

lifetime after this $PbBr_2$/OctAc/BuAm treatment was also longer (τ_{avg} = 7.3 ns) compared to the as-synthesized $CsPbBr_3$ OAm/OAc NCs (τ_{avg} = 4.8 ns), as shown in **Figure 4.3**. OcAc and BuAm react to form butylammonium octanoate, which binds to the NC surface as X-type ligands similar to oleylammonium oleate.[45] However, butylammonium octanoate is significantly smaller than oleylammonium oleate which should allow it to better penetrate through the nano-porous film. At the same time, $PbBr_2$ has been reported to introduce excess Br^- anions which also help passivate the NC surface.[40] We also investigated the effect of adding trifluoroacetate (TFA) ions, which has been found to bind stronger to the surface lead ions, leading to better passivation.[39] TFA is also smaller than OctAc and should increase the electronic contact between the NCs. When a treatment of $PbBr_2$/OctAc/BuAm/TFA was used, the PLQY was roughly the same (76%), but the PL lifetime was slightly reduced (τ_{avg} = 3.5 ns), which is consistent with an increase in electronic coupling. Finally, we note that the PLQY values attained through this film treatment method is still lower than the reported >95% obtained by solution-phase treatment,[40] which could be due to inaccessibility of a small amount of unpassivated surface sites after film deposition.

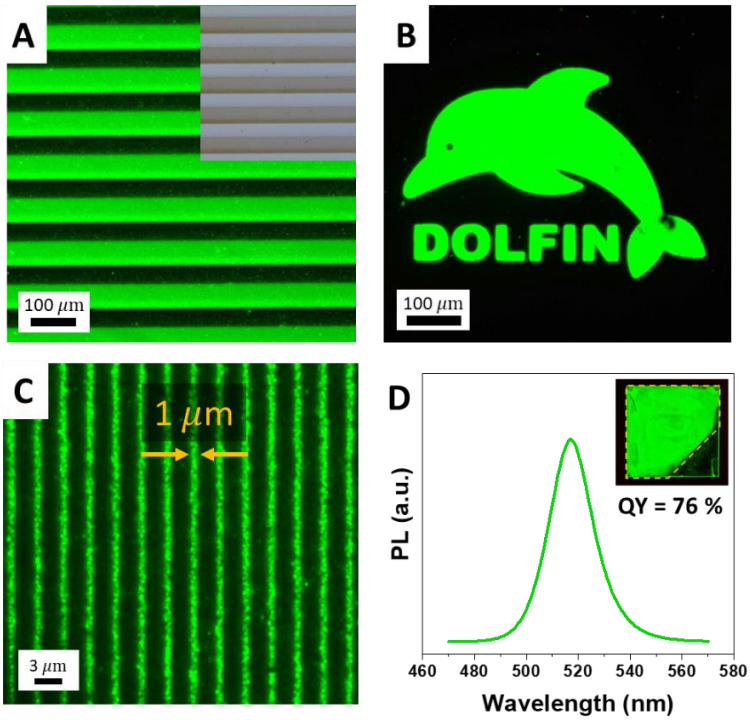

E

Treatment on patterned film	PLQY $\pm \sigma$ (%)
No treatment	< 5
Trifluoroacetic acid + butylamine	37 ± 3
$PbBr_2$ + octanoic acid + butylamine	79 ± 2
$PbBr_2$ + octanoic acid + butylamine + trifluoroacetic acid	76 ± 3

Figure 4.2. Patterns of $CsPbBr_3$ NCs changes to their PLQY with various treatments. (A-C) Fluorescence optical microscope images of micro-patterned films of $CsPbBr_3$ NCs with the PA-480 photosensitizer. Inset in (A): Bright-field optical microscope image. (D) Photoluminescence (PL) spectrum of a CsPbBr3 film (PLQY = 76%) after patterning with PA-480 followed by treatment with a mixture of $PbBr_2$, octanoic acid, butylamine and trifluoroacetic acid in ethyl acetate. Inset: Photograph of the film under ultraviolet light. The dotted orange line indicates the region exposed to 405 nm light during the patterning process. (E) Table showing the PLQY of patterned $CsPbBr_3$ films with various of post-patterning treatments.

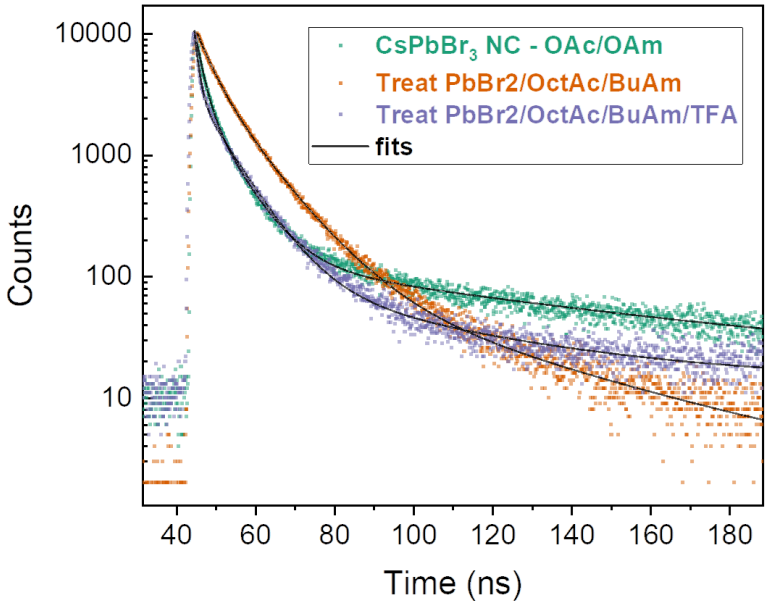

Film sample	A_1 (%)	τ_1 (ns)	A_2 (%)	τ_2 (ns)	A_3 (%)	τ_3 (ns)	τ_{Avg} (ns)	PLQY (%)	τ_{rad} (ns)	$\tau_{non-rad}$ (ns)
$CsPbBr_3$ NCs – OAc/OAm	26.2	1.9	48.8	7.2	25.1	78.3	4.8	58	8.3	11.4
Treat $PbBr_2$/OctAc/ BuAm	23.1	3.9	63.8	10.2	8.1	43.1	7.3	78 (70 after lifetime mea.)	9.4	33.2
Treat $PbBr_2$/OctAc/ BuAm/TFA	19.9	1.0	67.8	7.8	12.3	44.0	3.5	70 (63 after lifetime mea.)	5.0	11.7

Figure 4.3. PL lifetime of $CsPbBr_3$ NC films after different treatments compared to $CsPbBr_3$ OAc/OAm NCs. The table shows the fitting parameters to a triexponential decay as well as calculation of the radiative and non-radiative lifetimes.

4.3. Patterning mechanism of $CsPbX_3$ NCs with oxime sulfonate esters

To elucidate the patterning mechanism, we investigated the changes that occur during each step of the patterning process (**Figure 4.4**). First, we measured the absorption and PL spectra of solutions and films containing LHP NCs and PA-480 (**Figure 4.4A** and **Figure 4.5**) and found that the absorption onset of the LHP NCs (~510 nm) does not change appreciably at each step of the process. Also, the shape of the PL peak at 512 nm does not change upon the addition of PA-480 and red-shifts by only 1 nm (to 513 nm) after irradiation in solution. The solution PLQY drops

from 31% to 19% after addition of PA-480 but recovers to 23% after irradiation (**Figure 4.6**). For films, the PL spectra further red-shifts by about 5 nm (to about 517 nm) after patterning and treatment (**Figure 4.2D**), which is consistent with coupling between the NCs. On the other hand, the absorption peak of PA-480 at ~400 nm (superimposed on the absorption spectrum of LHP NCs) clearly changes upon photoirradiation with 405 nm light. Since similar absorption changes were observed when PA-480 was irradiated in the absence of LHP NCs (**Figure 4.7**), we infer that the photodecomposition process of PA-480 (**Figure 4.8**) is not significantly affected by the presence of the LHP NCs.

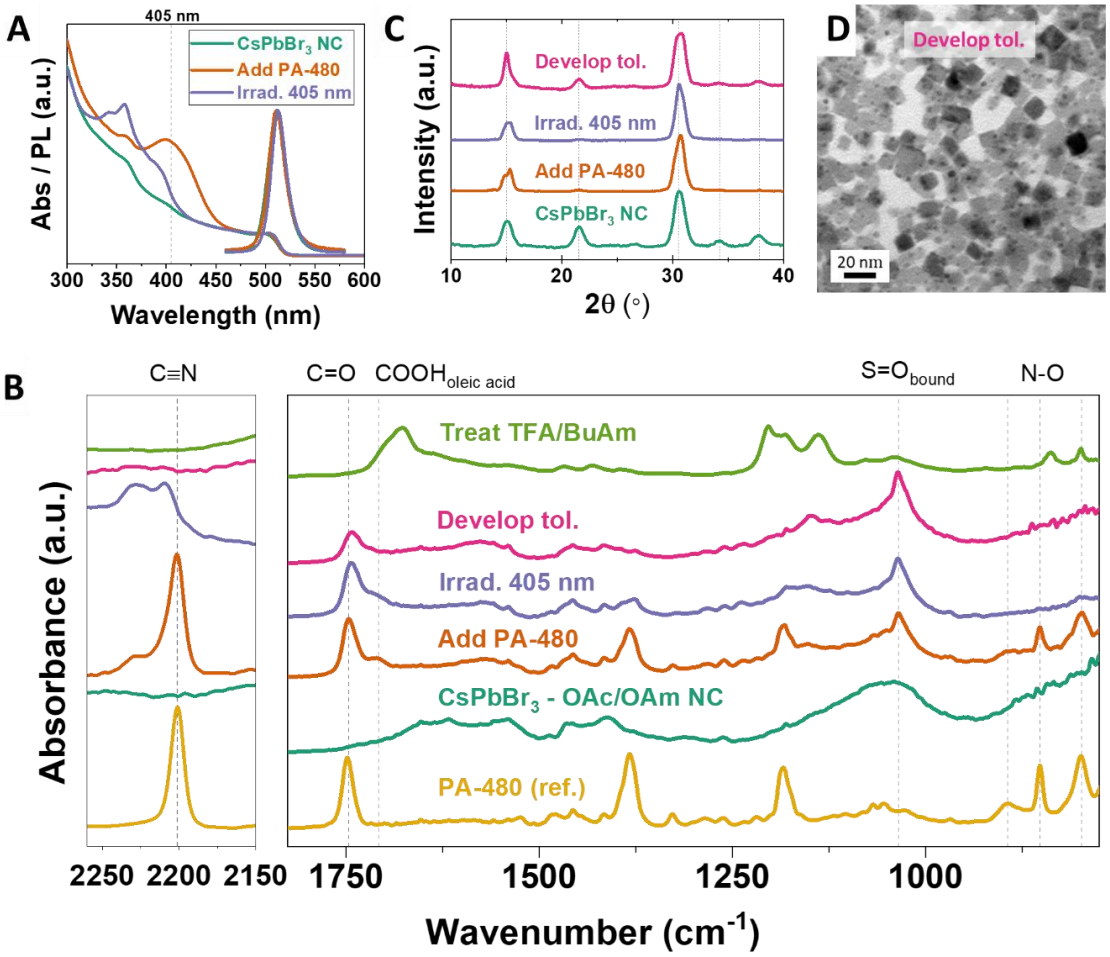

Figure 4.4. Investigation of the $CsPbBr_3$ NCs and their ligands after each step of the DOLFIN patterning process. (A) Solution-phase absorption and photoluminescence spectra of $CsPbBr_3$ NCs as synthesized, after the addition of PA-480, and after irradiation with 405 nm light. (B) FTIR absorption spectra of $CsPbBr_3$ NCs as synthesized, after the addition of PA-480, irradiation with 405 nm light, development with toluene, and post-patterning treatment with a trifluoroacetic acid/butylamine (TFA/BuAm) mixture in ethyl acetate. The spectra of a PA-480 film is also plotted for reference. (C) Powder X-ray diffraction (XRD) spectra as synthesized, after the addition of PA-480, irradiation with 405 nm light and development with toluene. (D) Transmission electron microscope (TEM) images of the $CsPbBr_3$ NCs after development.

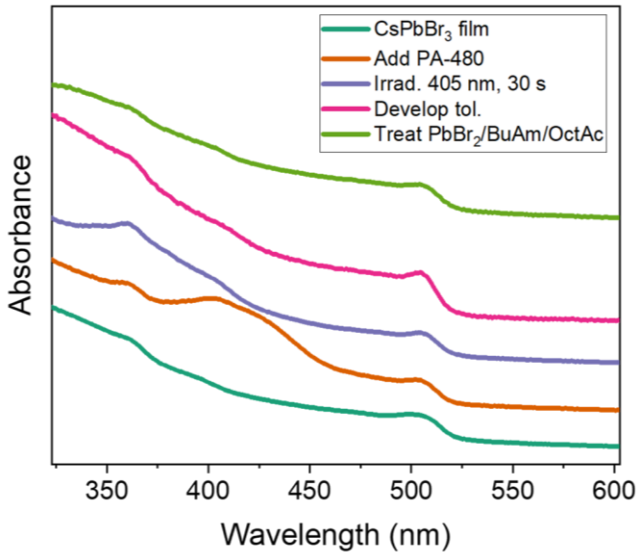

Figure 4.5. Film absorption spectra of $CsPbBr_3$ NCs as synthesized, after the addition of PA-480, irradiation with 405 nm light, development with toluene and treatment with octanoic acid/butylamine/$PbBr_2$.

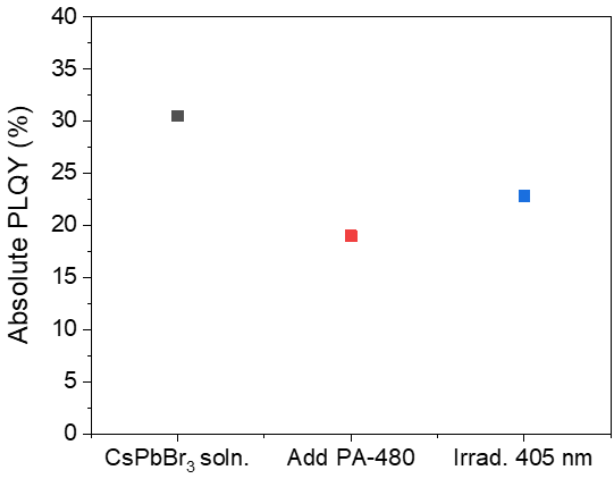

Figure 4.6. Changes to the PLQY of $CsPbBr_3$ NC solutions. PLQY measurements of a dilute $CsPbBr_3$ OAc/OAm NC solution (no excess ligands added), after adding PA-480, and after irradiation with 405 nm light. The PLQY after adding PA-480 was calculated by a relative method with 475 nm excitation (to avoid absorption by PA-480), while the other two measurements were obtained with an integrating sphere and a 405 nm laser.

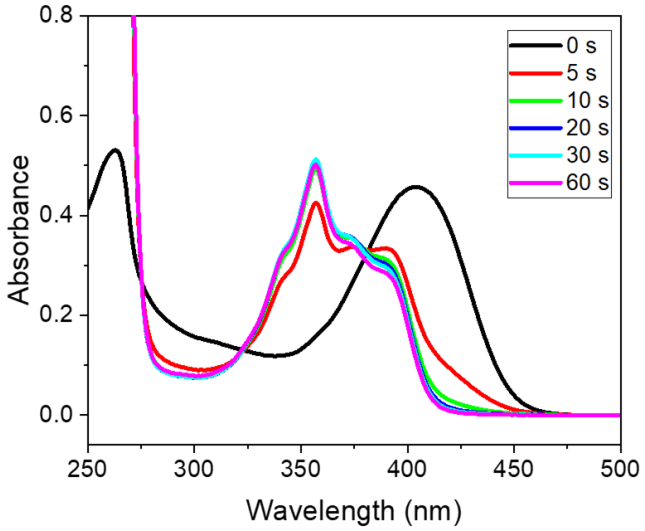

Figure 4.7. Absorption spectra of a solution of PA-480 upon irradiation with 405 nm light.

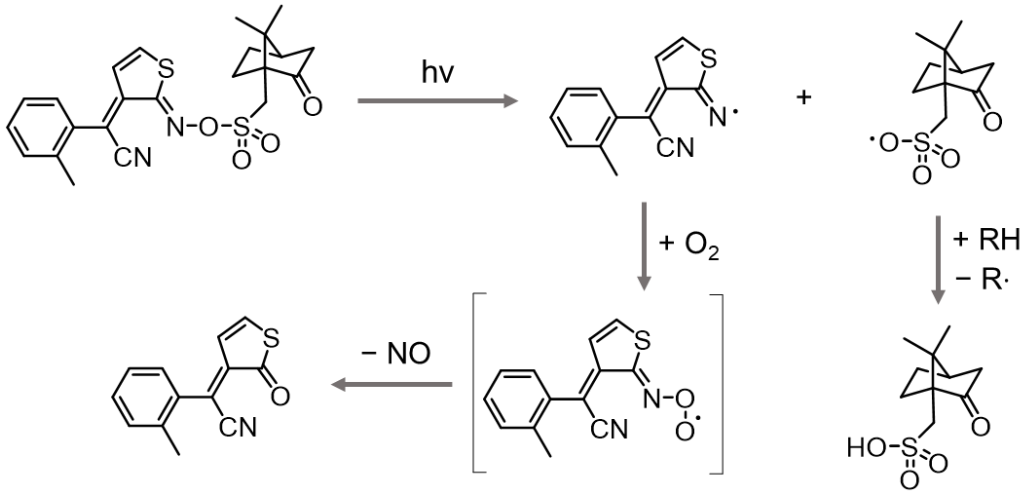

Figure 4.8. Decomposition pathway of PA-480 in air.[36, 46-47]

Next, to better understand the photopatterning chemistry, we carried out film FTIR spectroscopy to probe changes in the ligand shell of the LHP NCs (**Figure 4.4B** and **Figure 4.9**). Conveniently, PA-480 has several distinct IR absorption peaks: C≡N (2201 cm^{-1}), C=O (1746 cm^{-1}), S=O (1068 cm^{-1}, 1054 cm^{-1}) and N–O (894 cm^{-1}, 852 cm^{-1}, 798 cm^{-1}). The N–O peaks were assigned based on previous reports and on the observation that these peaks completely disappear upon photoirradiation (Figure S6).[48-49] The as-synthesized $CsPbBr_3$ NCs have mostly broad

absorption peaks in the 1750–940 cm^{-1} region, which can be assigned to bound oleylammonium and oleate ligands. Upon addition of PA-480 to the NCs, the resulting FTIR spectrum looks similar to a superposition of the PA-480 and the NC spectra aside from two important changes: (1) the appearance of a peak at 1708 cm^{-1} which can be distinctively assigned to free oleic acid (indicating that it has been displaced),[1, 50] and (2) the red-shift of the S=O peaks to 1035 cm^{-1}, which has been previously assigned to a surface-bound sulfonate group.[51] To preserve charge neutrality, we believe that oleylammonium ligands are also displaced together with the oleate, although the bound or unbound state of oleylammonium is harder to verify by FTIR due to interfering peaks. In other words, we hypothesize that the X-type oleylmmonium oleate ion pair has been replaced by the neutral L-type PA-480 ligand, which binds through the sulfonate oxygen atoms. Upon irradiation, the N–O peaks vanish, indicating the complete cleavage of PA-480. After development with toluene, the C=O and S=O peaks remain strongly present, which means that the sulfonate fragment (that contains the ketone group) stays attached to the NC surface. In contrast, the C≡N peaks are no longer present, which implies that the cyanide fragment has been washed away during this step. Finally, treatment of the film with trifluoroacetic acid/butylamine dissolved in ethyl acetate reveals that all the peaks of the sulfonate ligand (C=O and S=O) are replaced by bound trifluoroacetate peaks (COO^-: 1676 cm^{-1}, C–F: 1220–1110 cm^{-1}). Hence, although the sulfonate group resists dissolution in the toluene developer, it can still be substituted by other surface ligands that have an even stronger affinity for the NC surface. This allows for further tunability of the ligand shell, which is important to achieve good material performance.

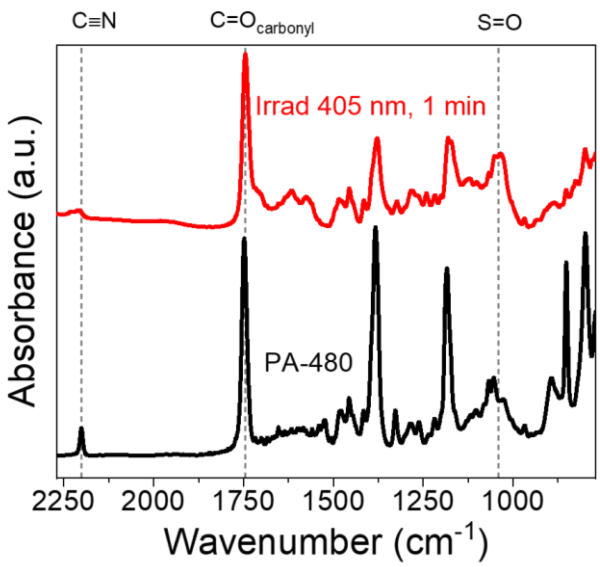

Figure 4.9. FTIR spectra of a film of PA-480 before and after irradiation with 405 nm light.

Additionally, we used powder X-ray diffraction (XRD) and transmission electron microscopy (TEM) to explore how our patterning chemistry affects the inorganic LHP nanostructure. XRD analysis shows that the orthorhombic $CsPbBr_3$ diffraction peaks are retained throughout the patterning process with no new crystalline phases (**Figure 4.4C**). Careful examination of the pseudo-cubic (100) peaks (2θ ~ 15°) reveal subtle differences in the peak splitting profile at each step. One possibility is the splitting of the (100) peak can be attributed to interference effects from superlattice formation. This has been recently explained using a multilayer diffraction model.[52] We obtained a reasonable fit the (100) and the (200) peaks (2θ ~ 30.5°), which shows that the differences in the peak profile can be accounted for by variations in the NC ordering (**Figure 4.10**). Based on this, the differences observed in the XRD patterns during the patterning treatments likely are not a result of changes to the inorganic core of the nanocrystal. This is further supported by a UV-vis absorption of the developed films which do not contain sharp features in the 300–350 nm range, which is where several LHP decomposition products can appear (**Figure 4.5**).[53-54] Transmission electron microscopy (TEM) reveals that the average size of the

LHP NCs remains constant at about 10 $\pm$ 2 nm throughout the entire patterning process (**Figure 4.11**). The NCs were found to be well separated after the addition of PA-480 and irradiation but had significant necking upon development with toluene (**Figure 4.4D**).

Sample	Atomic periodicity, d (Å)	Interparticle spacing, L (Å)	σ_L (Å)	Number of scattering planes, N (planes)	σ_N (planes)
$CsPbBr_3$ OAm/OAc	5.8066	36.4747	2.9251	14.1523 (82.2 Å thick)	1.002
Add PA-480	5.8159	38.6175	1.5521	16.5232 (96.1 Å thick)	1.6382
Irrad. 405 nm	5.8295	38.3672	2.0269	16.0274 (93.4 Å thick)	3.2688
Develop tol.	5.7881	35.4142	1.4207	14.4881 (83.9 Å thick)	3.5734

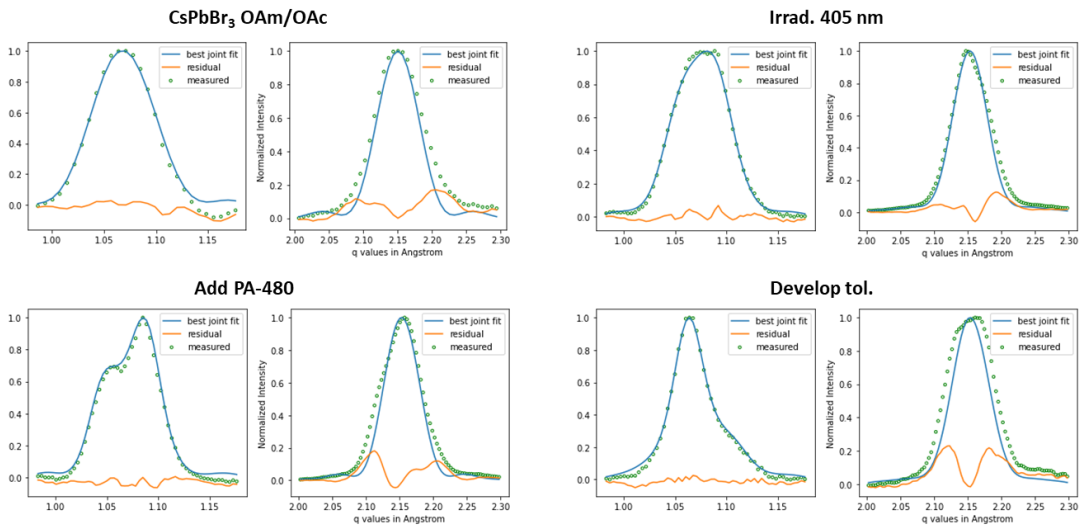

Figure 4.10. Fitting of the (100) and (200) XRD peaks at each point of the patterning process with a multilayer diffraction fitting algorithm.[52]

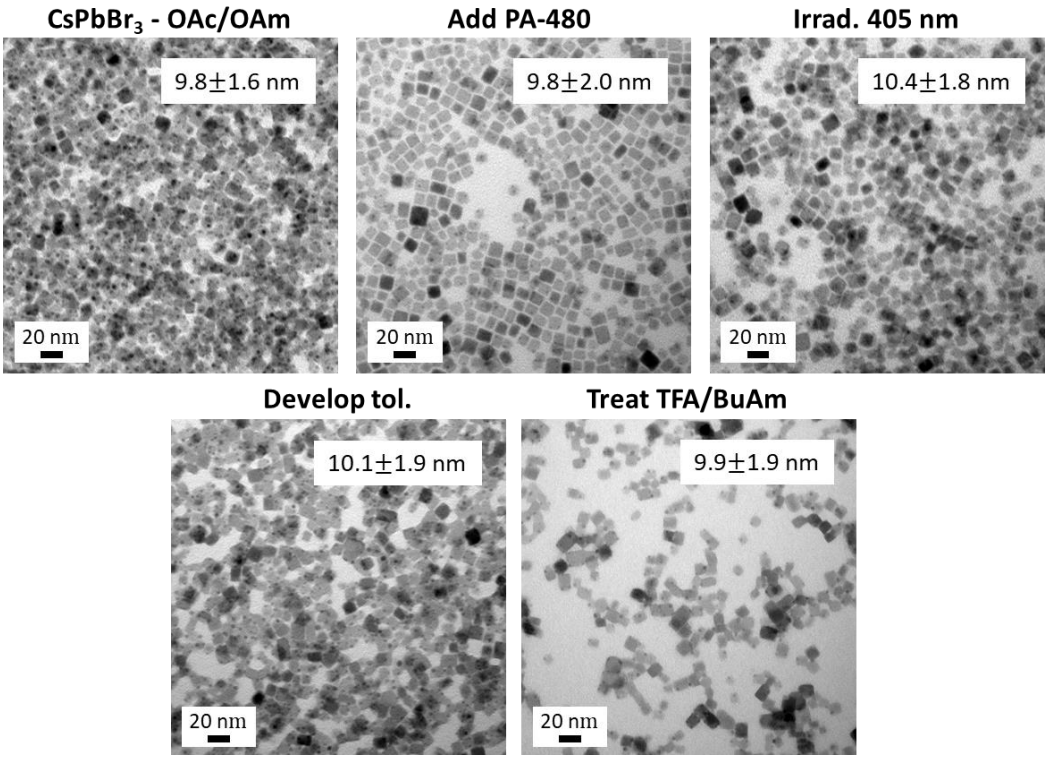

Figure 4.11. Transmission electron microscope images of $CsPbBr_3$ NCs at each point of the patterning process. We note that these films were much thinner than those prepared via spin coating to facilitate TEM characterization. Also, note that the image after TFA/BuAm treatment is for a sparser region and does not indicate that NCs are removed.

To summarize our mechanistic studies, we obtained results consistent with a patterning mechanism involving the photoinduced cleavage of a bound oxime sulfonate ligand. The binding of the sulfonate ligand is supported both by the detection of free oleic acid and bound sulfonate signals. Photoirradiation and development result in the cleavage of the ligand, leaving behind a bound sulfonate group that reduces the LHP NC solubility in toluene. This solubility change is likely due to the increase in the polarity of the ligands after decomposition: a relatively large, non-polar, aryl ligand is cleaved into a shorter, polar ketone ligand. In addition, this mechanism is also supported by the successful patterning of LHP NCs using an imido sulfonate ester (ILP-110N) which has the same cleavable –N–OSOO– motif but with different side groups (**Figure 4.12**). The

patterns formed with ILP-110N also had good contrast but was more prone to cracking, which we attribute to limited substrate adhesion of the perflorinated butyl chain.

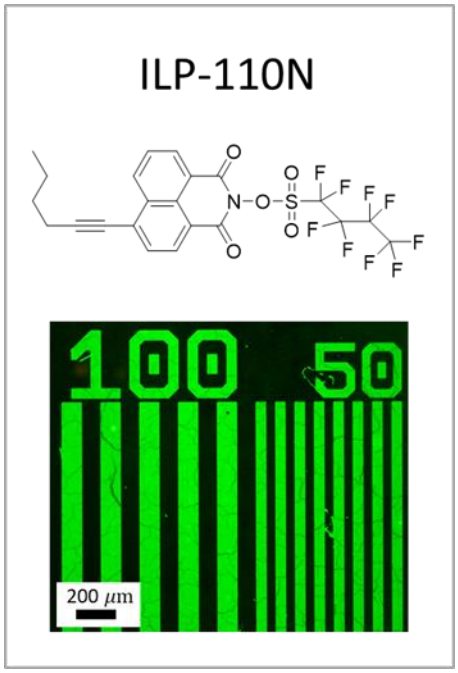

Figure 4.12. Optical microscope image of $CsPbBr_3$ NCs patterns using ILP-110N.

4.4. Emission color tuning of the LHP NC patterns

The emission wavelength of the LHP NC patterns can also be tuned across the visible spectrum by modifying its halide composition (**Figure 4.13**).[55-56] This can be done by synthesizing LHP NCs with different halide compositions, or through a post-patterning anion-exchange step. For instance, we synthesized and patterned $CsPbBr_{3-x}Cl_x$ NCs emitting at 447 nm, with x ~ 1.5 (**Figure 4.13A,F**). Alternatively, patterned $CsPbBr_3$ NCs can be transformed into $CsPbBr_{3-x}I_x$ NCs by treating the film with a solution of PbI_2/oleic acid/oleylamine in ethyl acetate (**Figure 4.13C–D**). Depending on the solution concentration and treatment time, various degrees of anion exchange occurred (**Figure 4.13E**). With this approach, $CsPbBr_3$ NCs emitting at 522 nm can be red-shifted to $CsPbBr_{3-x}I_x$ NCs emitting up to 653 nm, with x ~ 2 (**Figure 4.13F**). Although this

anion-exchange process also improves the PLQY, a subsequent ligand exchange with trifluoracetic and butylamine can be included to further increase the PLQY. Chloride exchange was also attempted, but only a small (~10 nm) blue-shift was observed due to the low solubility of $PbCl_2$ in ethyl acetate (**Figure 4.14**).

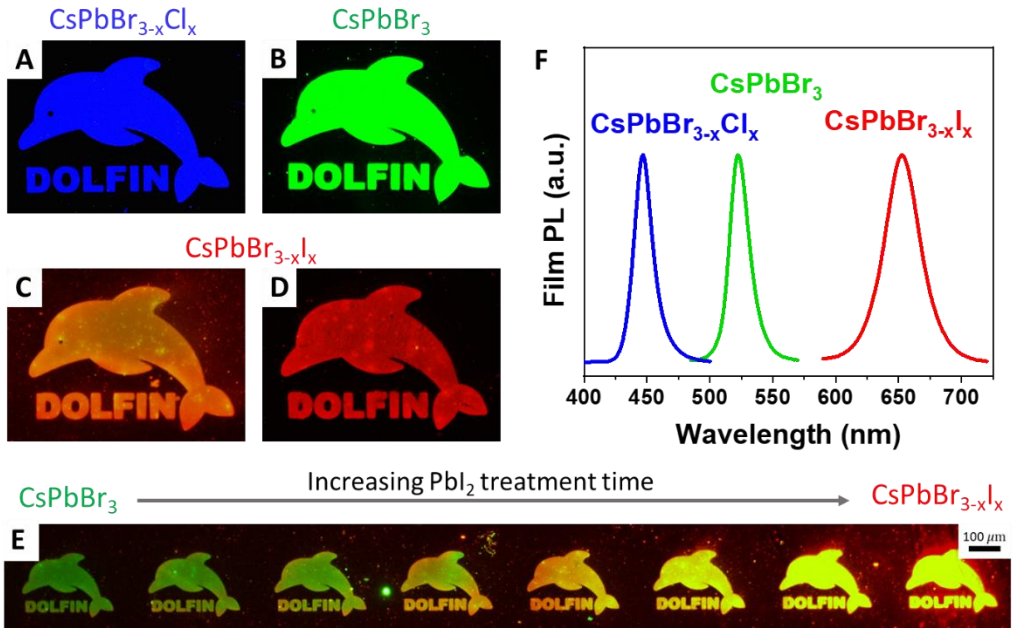

Figure 4.13. Modulating the emission color of NC films changing the halide composition. Fluorescence optical microscope images of micro-patterned films of $CsPbBr_{3-x}Cl_x$ (A), $CsPbBr_3$ (B) and $CsPbBr_{3-x}I_x$ (C&D). (E) Fluorescence image of a patterned $CsPbBr_3$ film that was slowly pulled out from a solution of PbI_2/oleic acid/oleylamine in ethyl acetate showing the progress of the anion exchange. (F) Film PL spectra of the $CsPbBr_{3-x}Cl_x$, $CsPbBr_3$, and $CsPbBr_{3-x}I_x$ NCs. The $CsPbBr_{3-x}I_x$ NCs were obtained by post-patterning anion exchange, while the $CsPbBr_{3-x}Cl_x$ NCs were synthesized directly.

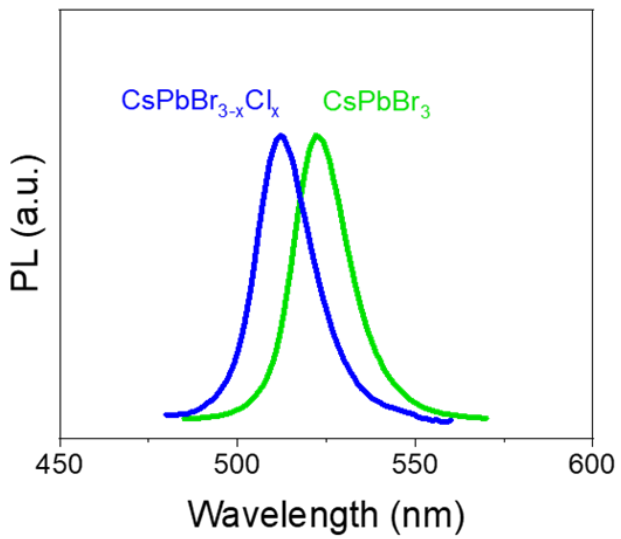

Figure 4.14. PL shift after chloride exchange of a patterned $CsPbBr_3$ NC film by treating with a solution of $PbCl_2$/oleic acid/oleylamine in ethyl aceate.

We also explored the patterning of multiple layers of LHP NCs. **Figure 4.15** shows patterning of a layer of $CsPbBr_{3-x}I_x$ NCs, followed by a second layer of $CsPbBr_3$ NCs. Anion exchange between the two layers was prevented by an intermediate layer of poly(methyl methacrylate) (PMMA) before the deposition of the second layer. Deposition of the PMMA layer did not appear to affect the optical properties of the LHP NCs. Without this layer of PMMA, significant anion exchange was observed, resulting in changes of the PL emission wavelength (**Figure 4.16**).[55]

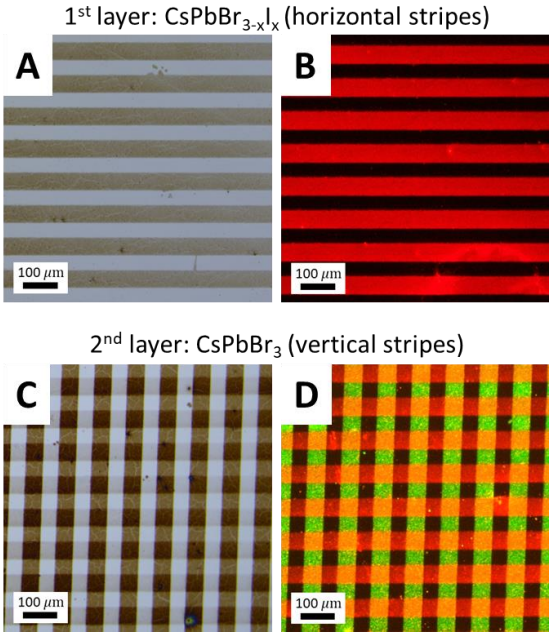

Figure 4.15. Multiple pattern layers of LHP NCs. Bright-field (A & C) and fluorescence (B & D) optical microscope images after the patterning one or two layers of $CsPbX_3$ NC. A layer of PMMA was spin-coated on top of the red-emitting $CsPbBr_{3-x}I_3$ layer before the deposition and patterning of the second green-emitting $CsPbBr_3$ layer. The red channel in image (D) was boosted during image processing for ease of visibility.

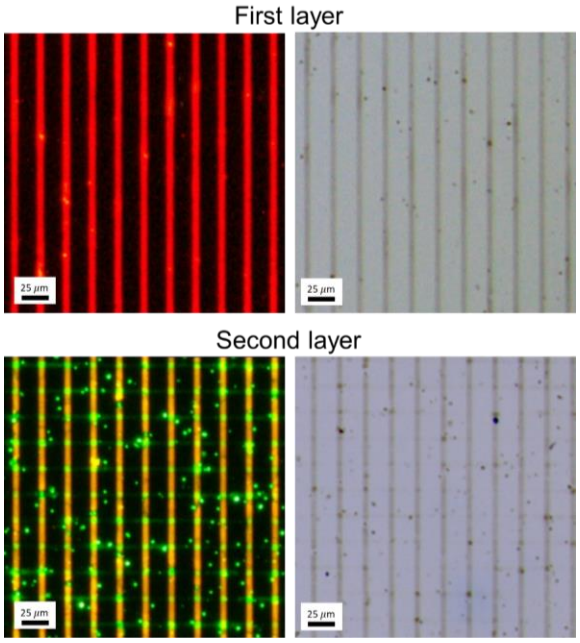

Figure 4.16. PL and optical microscope images after one and two layers of LHP NC patterns without any intermediate layer.

4.5. Photoconductivity of patterned $CsPbBr_3$ NC films

An important advantage of this ligand-cleavage patterning approach over other polymer-based approaches is the short distance between the NCs which enables electronic communication and is important for applications such as LEDs, photodetectors, and other optoelectronic devices. As a proof of concept, we fabricated and tested simple photoconductor devices by depositing and patterning $CsPbBr_3$ NCs on top of an interdigitated gold electrode (**Figure 4.17A–B**). After treating the NCs with a trifluoracetic/butylamine solution, the devices exhibit a distinct photo-response to violet light (**Figure 4.17C**), demonstrating the capability for charge injection or extraction into our NC layers. Although the performance of the photodetector shown here is lower than prior reports of optimized $CsPbBr_3$ films,[57-58] we believe that it can be improved with further optimization of the film thickness, NC packing density and ligand chemistry. In the future, more sophisticated ligand exchanges and surface treatments can be explored for the fabrication of high-efficiency patterned LED.[5-6]

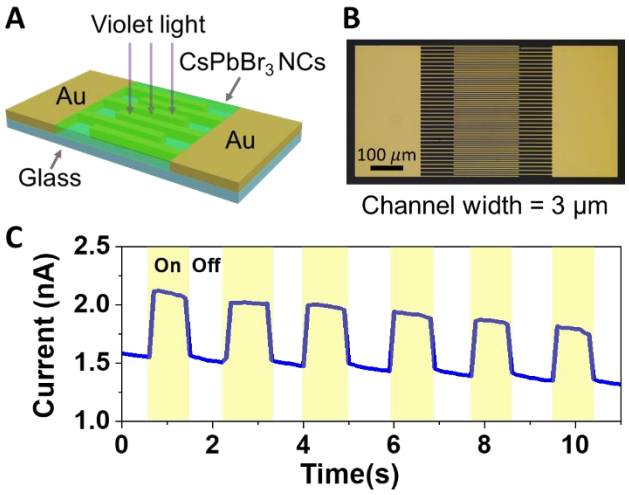

Figure 4.17. Photoconductivity of patterned $CsPbBr_3$ NCs after treatment with trifluoroacetic acid/butylamine. (A) Schematic of the device structure and testing condition. (B) Optical microscope image of the gold electrodes used. (C) Photocurrent–time response in the dark and under illumination with violet light (395 nm) with an applied voltage of 20 V.

4.6. Conclusion

In summary, we have demonstrated the patterning of $CsPbX_3$ NCs via the photoinduced cleavage of a bound oxime sulfonate ester (PA-480). The photosensitive PA-480 binds to the NC surface and cleaves at the N–O bond upon irradiation with 405 nm light, resulting in a change in the NC solubility in toluene allowing for pattern development. The patterned LHP NCs can be further treated to exchange the sulfonate ligands with more suitable ones such as trifluoroacetate, which allows for the improvement in the film PLQY up to 76%. The emission wavelength of the patterns can also be tuned across the visible by an on-film anion exchange or by using pre-synthesized alloyed NCs. Further, multilayer patterning of NC layers with different colors was also demonstrated. Finally, we fabricated simple photoconductive devices to show that patterned NC layers are amenable to electrical contact, which is an important prerequisite for various optoelectronic applications. This approach shows the capability of carefully designed photosensitive ligands for patterning fragile nanomaterials such as the LHP NCs.

4.7. Materials and methods

Chemicals. PA-480 (Benzeneacetonitrile, α-[2-[[[[(7,7-dimethyl-2-oxobicyclo[2.2.1] hept-1-yl)methyl]sulfonyl]oxy]imino]-3(2H)-thienylidene]-2-methyl-) and ILP-110N (1-Butanesulfonic acid, 1,1,2,2,3,3,4,4,4-nonafluoro-, 6-(1-hexyn-1-yl)-1,3-dioxo-1H-benz[de] isoquinolin-2(3H)-yl ester) were obtained from Heraeus Epurio. Cesium carbonate (99%), lead(II) acetate trihydrate (>99.99%), oleic acid (technical grade, 90%), oleylamine (technical grade, 70%) and octadecene (technical grade, 90%), benzoyl chloride (>99%), ethyl acetate (99.8%), toluene (99.8%), chlorobenzene (99.8%), trifluoroacetic acid (99%), octanoic acid (>99%), butylamine

(99.5%), lead(II) iodide (99.999%) were purchased from Millipore Sigma. Benzoyl bromide (97%) was purchased from Acros Organics. Lead(II) bromide (99.999%) was purchased from Alfa Aesar.

Synthesis of $CsPbX_3$ NCs. $CsPbBr_3$ NCs were synthesized by a modified benzoyl halide hot injection method.[38] Briefly cesium carbonate (16 mg, 0.049 mmol), lead acetate trihydrate (76 mg, 0.20 mmol), oleic acid (0.3 mL, 0.95 mmol), oleylamine (1 mL, 3.0 mmol) and octadecene (10 mL) were loaded into a 25 mL 3-neck round-bottom flask and dried under vacuum for 1 h at 115 °C. Subsequently, the temperature was increased to 170 °C under N_2 and benzoyl bromide (50 µL, 0.46 mmol) dissolved in 0.5 mL octadecene was swiftly injected. The reaction mixture was immediately cooled down with an ice-water bath. To purify the NCs, 1 mL of toluene was added to the crude solution followed by 40 mL of ethyl acetate. The resulting mixture was centrifuged (7 krpm, 6574 g-force) for 10 min with the temperature set at 0 °C. The supernatant was discarded, and the precipitate was brought into a N_2 glovebox and redispersed in 3 mL of toluene at a concentration of about 2.5 wt%. The solution was then centrifuged (4 krpm, 2213 g-force) for 1 min at room temperature to remove any insoluble contaminants. This stock NC solution was stored in the glovebox and used within 1-2 weeks. To synthesize $CsPbBr_{3-x}Cl_x$ NCs, a similar procedure was used except that a mixture of benzoyl bromide (25 µL) and benzoyl chloride (25 µL) dissolved in 0.5 mL of octadecene was used as the injection solution.

Patterning of LHP NCs. In air, 500 µL of ethyl acetate was added to 200 µL of the LHP NC stock solution to induce flocculation of NCs. The suspension was centrifuged (13.4 krpm, 12100 g) for 1 min. The supernatant was discarded, and the precipitate redissolved in 80 µL of chlorobenzene (or toluene). To this solution, 16 µL of PA-480 pre-dissolved in chlorobenzene (or

toluene) at a concentration of 5 wt/vol% was added, resulting in a solution with about 5 wt% NC and 0.8 wt% PA-480. This solution was spincoated on either a silicon substrate or a glass cover slip. The substrate was then bound between a glass slide and a patterned chrome on quartz mask using two binder clips. This stack was then exposed to 405 nm light (M405LP1-C1, Thorlabs, measured power density ~30 mW/cm^2) for 10 – 30 s. After exposure, the substrate was immersed into a toluene developer for ~10 s and dried with a N_2 gun. Occasionally, a pre-exposure and a post-exposure baking step at 70 °C was used to increase the contrast. For multiple layer patterning, an intermediate layer of PMMA (MW~120k, 2 wt/vol% in anisole) was spin-coated between each NC layer.

Ligand and anion exchange. To prepare the $PbBr_2$/OctAc/BuAm treatment solution, $PbBr_2$ (0.5 mmol, 183 mg) was dissolved in butylamine (3 mmol, 296 uL), octanoic acid (3 mmol, 475 uL) and hexane (300 uL) by stirring overnight at 70 °C (total volume ~ 1 mL). About 10 vol% of this solution (100 uL) was then mixed with 9.9 mL of ethyl acetate to give a solution with <5 mM $PbBr_2$ (saturated), 30 mM OctAc, 30 mM BuAm and 23 mM hexane. (White $PbBr_2$ slowly precipitates out, which indicates saturation.) To prepare the $PbBr_2$/OctAc/BuAm/TFA treatment solution, the same procedure was used but with trifluoroacetic acid (0.5 mmol, 38 uL) added to the starting solution which result in treatment solution of 5 mM TFA, <5 mM $PbBr_2$ (saturated), 30 mM OctAc, 30 mM BuAm and 23 mM hexane in ethyl acetate.

To carry out ligand exchange, the substrate with the patterned LHP NC layer was placed in a spin-coater and a ligand treatment solution was pipetted on the substrate and allowed to sit for ~10 s before spinning. This spin-coating step was then repeated another time. To carry out I^- anion exchange, the patterned substrates were immersed in a solution of PbI_2/oleic acid/oleylamine in

ethyl acetate. The extend of the exchange depends on the PbI_2 concentration and the duration of treatment. After the appropriate amount of treatment time, the substrates were removed and blown dry with N_2. Subsequent treatment of the iodide-exchanged film with an ethyl acetate solution of 5 mM trifluoroacetate and 5 mM butylamine can be used to further improve the PLQY. These ligand/anion steps can be carried out in air when the humidity is low (*e.g.* in the winter months), but should be carried out in a glovebox when the humidity is high.

Photoconductivity measurement. The device electrodes (channel width = 3 µm, total channel length = 13.2 mm) were fabricated on glass *via* a standard photolithography process with a direct laser writer (Heidelberg MLA 150). The electrodes were deposited by electron-beam evaporation of a 5-nm Ti adhesion layer and a 100-nm Au layer (AJA ATC-Orion 8E). $CsPbBr_3$ NCs were deposited and patterned on the electrodes followed by a ligand exchange with trifluoroacetic/butylamine/$PbBr_2$. Electrical measurements were carried out in a N_2 glovebox with probes connected to a parameter analyzer (Agilent B1500A). Violet light illumination was provided by a violet LED flashlight (TaoTronics, wavelength = 395 nm).

Characterization techniques. Optical absorption spectra of NP solutions or films were collected using a Shimadzu UV-3600i Plus UV-Vis-NIR spectrophotometer in transmission mode. Optical microscope images and fluorescent images were obtained using an Olympus BX51 microscope. The contrast and brightness of the optical images were manipulated using the camera software or with ImageJ. Transmission electron microscope (TEM) images were acquired using a Tecnai Spirit operated at 120kV. Wide angle powder X-ray diffraction (XRD) patterns were collected using a Rigaku Miniflex diffractometer with a Cu Kα X-ray sourc. Infrared absorption

spectra of thin films were obtained with a Thermo Nicolet iS50 Advanced FTIR in transmission mode (using a ZnSe substrate from Crystran Ltd.). Photoluminescence spectra were collected with a Horiba JobinYvon Fluoromax-4 system. Absolute photoluminescence quantum yield measurements were carried out using an integrating sphere (Labsphere) coupled with a computer-controlled spectrometer (Ocean Optics QE Pro) together with a 405-nm laser diode excitation source (LDM405, Thorlabs, 4 mW).

4.8. Chapter bibliography

1. Protesescu, L.; Yakunin, S.; Bodnarchuk, M. I.; Krieg, F.; Caputo, R.; Hendon, C. H.; Yang, R. X.; Walsh, A.; Kovalenko, M. V., Nanocrystals of Cesium Lead Halide Perovskites (CsPbX3, X = Cl, Br, and I): Novel Optoelectronic Materials Showing Bright Emission with Wide Color Gamut. *Nano Lett.* **2015,** *15* (6), 3692-3696.

2. Kovalenko, M. V.; Protesescu, L.; Bodnarchuk, M. I., Properties and potential optoelectronic applications of lead halide perovskite nanocrystals. *Science* **2017,** *358* (6364), 745-750.

3. Shamsi, J.; Urban, A. S.; Imran, M.; De Trizio, L.; Manna, L., Metal Halide Perovskite Nanocrystals: Synthesis, Post-Synthesis Modifications, and Their Optical Properties. *Chem. Rev.* **2019,** *119* (5), 3296-3348.

4. Nature MaterialsAkkerman, Q. A.; Rainò, G.; Kovalenko, M. V.; Manna, L., Genesis, challenges and opportunities for colloidal lead halide perovskite nanocrystals. *Nat. Mater.* **2018,** *17* (5), 394-405.

5. Kim, Y.-H.; Kim, S.; Kakekhani, A.; Park, J.; Park, J.; Lee, Y.-H.; Xu, H.; Nagane, S.; Wexler, R. B.; Kim, D.-H.; Jo, S. H.; Martínez-Sarti, L.; Tan, P.; Sadhanala, A.; Park, G.-S.; Kim, Y.-W.; Hu, B.; Bolink, H. J.; Yoo, S.; Friend, R. H.; Rappe, A. M.; Lee, T.-W., Comprehensive defect suppression in perovskite nanocrystals for high-efficiency light-emitting diodes. *Nat. Photonics* **2021,** *15* (2), 148-155.

6. Hassan, Y.; Park, J. H.; Crawford, M. L.; Sadhanala, A.; Lee, J.; Sadighian, J. C.; Mosconi, E.; Shivanna, R.; Radicchi, E.; Jeong, M.; Yang, C.; Choi, H.; Park, S. H.; Song, M. H.; De Angelis, F.; Wong, C. Y.; Friend, R. H.; Lee, B. R.; Snaith, H. J., Ligand-engineered bandgap stability in mixed-halide perovskite LEDs. *Nature* **2021,** *591* (7848), 72-77.

7. Zheng, X.; Yuan, S.; Liu, J.; Yin, J.; Yuan, F.; Shen, W.-S.; Yao, K.; Wei, M.; Zhou, C.; Song, K.; Zhang, B.-B.; Lin, Y.; Hedhili, M. N.; Wehbe, N.; Han, Y.; Sun, H.-T.; Lu, Z.-H.; Anthopoulos, T. D.; Mohammed, O. F.; Sargent, E. H.; Liao, L.-S.; Bakr, O. M., Chlorine

Vacancy Passivation in Mixed Halide Perovskite Quantum Dots by Organic Pseudohalides Enables Efficient Rec. 2020 Blue Light-Emitting Diodes. *ACS Energy Lett.* **2020,** *5* (3), 793-798.

8. Jeon, S.; Lee, S. Y.; Kim, S.-K.; Kim, W.; Park, T.; Bang, J.; Ahn, J.; Woo, H. K.; Chae, J.-Y.; Paik, T.; Seong, T.-Y.; Oh, S. J., All-Solution Processed Multicolor Patterning Technique of Perovskite Nanocrystal for Color Pixel Array and Flexible Optoelectronic Devices. *Adv. Opt. Mater.* **2020,** *8* (17), 2000501.

9. Xing, D.; Lin, C.-C.; Ho, Y.-L.; Kamal, A. S. A.; Wang, I. T.; Chen, C.-C.; Wen, C.-Y.; Chen, C.-W.; Delaunay, J.-J., Self-Healing Lithographic Patterning of Perovskite Nanocrystals for Large-Area Single-Mode Laser Array. *Adv. Funct. Mater.* **2021,** *31* (1), 2006283.

10. Wang, Y.; Li, X.; Song, J.; Xiao, L.; Zeng, H.; Sun, H., All-Inorganic Colloidal Perovskite Quantum Dots: A New Class of Lasing Materials with Favorable Characteristics. *Adv. Mater.* **2015,** *27* (44), 7101-7108.

11. Yakunin, S.; Protesescu, L.; Krieg, F.; Bodnarchuk, M. I.; Nedelcu, G.; Humer, M.; De Luca, G.; Fiebig, M.; Heiss, W.; Kovalenko, M. V., Low-threshold amplified spontaneous emission and lasing from colloidal nanocrystals of caesium lead halide perovskites. *Nat. Commun.* **2015,** *6* (1), 8056.

12. Liu, C.; Zeng, Q.; Wei, H.; Yu, Y.; Zhao, Y.; Feng, T.; Yang, B., Metal Halide Perovskite Nanocrystal Solar Cells: Progress and Challenges. *Small Methods* **2020,** *4* (10), 2000419.

13. Swarnkar, A.; Marshall, A. R.; Sanehira, E. M.; Chernomordik, B. D.; Moore, D. T.; Christians, J. A.; Chakrabarti, T.; Luther, J. M., Quantum dot-induced phase stabilization of alpha-CsPbI3 perovskite for high-efficiency photovoltaics. *Science* **2016,** *354* (6308), 92-95.

14. Ramasamy, P.; Lim, D.-H.; Kim, B.; Lee, S.-H.; Lee, M.-S.; Lee, J.-S., All-inorganic cesium lead halide perovskite nanocrystals for photodetector applications. *Chem. Commun.* **2016,** *52* (10), 2067-2070.

15. Gandini, M.; Villa, I.; Beretta, M.; Gotti, C.; Imran, M.; Carulli, F.; Fantuzzi, E.; Sassi, M.; Zaffalon, M.; Brofferio, C.; Manna, L.; Beverina, L.; Vedda, A.; Fasoli, M.; Gironi, L.; Brovelli, S., Efficient, fast and reabsorption-free perovskite nanocrystal-based sensitized plastic scintillators. *Nat. Nanotechnol.* **2020,** *15* (6), 462-468.

16. Chen, Q.; Wu, J.; Ou, X.; Huang, B.; Almutlaq, J.; Zhumekenov, A. A.; Guan, X.; Han, S.; Liang, L.; Yi, Z.; Li, J.; Xie, X.; Wang, Y.; Li, Y.; Fan, D.; Teh, D. B. L.; All, A. H.; Mohammed, O. F.; Bakr, O. M.; Wu, T.; Bettinelli, M.; Yang, H.; Huang, W.; Liu, X., All-inorganic perovskite nanocrystal scintillators. *Nature* **2018,** *561* (7721), 88-93.

17. Utzat, H.; Sun, W.; Kaplan, A. E. K.; Krieg, F.; Ginterseder, M.; Spokoyny, B.; Klein, N. D.; Shulenberger, K. E.; Perkinson, C. F.; Kovalenko, M. V.; Bawendi, M. G., Coherent single-photon emission from colloidal lead halide perovskite quantum dots. *Science* **2019,** *363* (6431), 1068.

18. Wu, S.; Fan, Z.; Wang, W.; Fan, H.; Mei, Z.; Sun, D.; Cheng, X.; Zhao, X.; Tian, Y., Microfabricable ratiometric gaseous oxygen sensors based on inorganic perovskite nanocrystals and PtTFPP. *Sens. Actuators, B* **2018,** *271*, 104-109.

19. Park, S.; Cho, J.; Jeong, D.; Jo, J.; Nam, M.; Rhee, H.; Han, J. S.; Cho, Y. J.; Ju, B.-K.; Ko, D.-H.; Jang, H. S., Simultaneous enhancement of luminescence and stability of CsPbBr3 perovskite nanocrystals via formation of perhydropolysilazane-derived nanopatterned film. *Chem. Eng. J.* **2020,** *393*, 124767.

20. Liu, Y.; Li, F.; Qiu, L.; Yang, K.; Li, Q.; Zheng, X.; Hu, H.; Guo, T.; Wu, C.; Kim, T. W., Fluorescent Microarrays of in Situ Crystallized Perovskite Nanocomposites Fabricated for Patterned Applications by Using Inkjet Printing. *ACS Nano* **2019,** *13* (2), 2042-2049.

21. Altintas, Y.; Torun, I.; Yazici, A. F.; Beskazak, E.; Erdem, T.; Serdar Onses, M.; Mutlugun, E., Multiplexed patterning of cesium lead halide perovskite nanocrystals by additive jet printing for efficient white light generation. *Chem. Eng. J.* **2020,** *380*, 122493.

22. Palazon, F.; Akkerman, Q. A.; Prato, M.; Manna, L., X-ray Lithography on Perovskite Nanocrystals Films: From Patterning with Anion-Exchange Reactions to Enhanced Stability in Air and Water. *ACS Nano* **2016,** *10* (1), 1224-1230.

23. Dou, L.; Lai, M.; Kley, C. S.; Yang, Y.; Bischak, C. G.; Zhang, D.; Eaton, S. W.; Ginsberg, N. S.; Yang, P., Spatially resolved multicolor CsPbX3 nanowire heterojunctions via anion exchange. *Proc. Natl. Acad. Sci. U. S. A.* **2017,** *114* (28), 7216-7221.

24. Lin, C. H.; Zeng, Q.; Lafalce, E.; Yu, S.; Smith, M. J.; Yoon, Y. J.; Chang, Y.; Jiang, Y.; Lin, Z.; Vardeny, Z. V.; Tsukruk, V. V., Large-Area Lasing and Multicolor Perovskite Quantum Dot Patterns. *Adv. Opt. Mater.* **2018,** *6* (16), 1800474.

25. Ko, J.; Ma, K.; Joung, J. F.; Park, S.; Bang, J., Ligand-Assisted Direct Photolithography of Perovskite Nanocrystals Encapsulated with Multifunctional Polymer Ligands for Stable, Full-Colored, High-Resolution Displays. *Nano Lett.* **2021,** *21* (5), 2288-2295.

26. Ko, J.; Chang, J. H.; Jeong, B. G.; Kim, H. J.; Joung, J. F.; Park, S.; Choi, D. H.; Bae, W. K.; Bang, J., Direct Photolithographic Patterning of Colloidal Quantum Dots Enabled by UV-Crosslinkable and Hole-Transporting Polymer Ligands. *ACS Appl. Mater. Interfaces* **2020,** *12* (37), 42153-42160.

27. Kim, H.; Hight-Huf, N.; Kang, J.-H.; Bisnoff, P.; Sundararajan, S.; Thompson, T.; Barnes, M.; Hayward, R. C.; Emrick, T., Polymer Zwitterions for Stabilization of CsPbBr3 Perovskite Nanoparticles and Nanocomposite Films. *Angew. Chem. Int. Ed.* **2020,** *59* (27), 10802-10806.

28. Lee, H.; Jeong, J. W.; So, M. G.; Jung, G. Y.; Lee, C. L., Design of Chemically Stable Organic Perovskite Quantum Dots for Micropatterned Light-Emitting Diodes through Kinetic Control of a Cross-Linkable Ligand System. *Adv. Mater.* **2021**, e2007855.

29. Minh, D. N.; Eom, S.; Nguyen, L. A. T.; Kim, J.; Sim, J. H.; Seo, C.; Nam, J.; Lee, S.; Suk, S.; Kim, J., Perovskite Nanoparticle Composite Films by Size Exclusion Lithography. *Adv. Mater.* **2018,** *30* (39), 1802555.

30. Huang, X.; Guo, Q.; Yang, D.; Xiao, X.; Liu, X.; Xia, Z.; Fan, F.; Qiu, J.; Dong, G., Reversible 3D laser printing of perovskite quantum dots inside a transparent medium. *Nat. Photonics* **2019,** *14* (2), 82-88.

31. Zhan, W.; Meng, L.; Shao, C.; Wu, X.-g.; Shi, K.; Zhong, H., In Situ Patterning Perovskite Quantum Dots by Direct Laser Writing Fabrication. *ACS Photonics* **2021,** *8* (3), 765-770.

32. Rainò, G.; Becker, M. A.; Bodnarchuk, M. I.; Mahrt, R. F.; Kovalenko, M. V.; Stöferle, T., Superfluorescence from lead halide perovskite quantum dot superlattices. *Nature* **2018,** *563* (7733), 671-675.

33. Krieg, F.; Sercel, P. C.; Burian, M.; Andrusiv, H.; Bodnarchuk, M. I.; Stöferle, T.; Mahrt, R. F.; Naumenko, D.; Amenitsch, H.; Rainò, G.; Kovalenko, M. V., Monodisperse Long-Chain Sulfobetaine-Capped CsPbBr3 Nanocrystals and Their Superfluorescent Assemblies. *ACS Cent. Sci.* **2021,** *7* (1), 135-144.

34. Wang, Y.; Pan, J.-A.; Wu, H.; Talapin, D. V., Direct Wavelength-Selective Optical and Electron-Beam Lithography of Functional Inorganic Nanomaterials. *ACS Nano* **2019,** *13* (12), 13917-13931.

35. Wang, Y.; Fedin, I.; Zhang, H.; Talapin, D. V., Direct optical lithography of functional inorganic nanomaterials. *Science* **2017,** *357* (6349), 385-388.

36. Pan, J.-A.; Rong, Z.; Wang, Y.; Cho, H.; Coropceanu, I.; Wu, H.; Talapin, D. V., Direct Optical Lithography of Colloidal Metal Oxide Nanomaterials for Diffractive Optical Elements with 2π Phase Control. *J. Am. Chem. Soc.* **2021,** *143* (5), 2372-2383.

37. Cho, H.; Pan, J. A.; Wu, H.; Lan, X.; Coropceanu, I.; Wang, Y.; Cho, W.; Hill, E. A.; Anderson, J. S.; Talapin, D. V., Direct Optical Patterning of Quantum Dot Light-Emitting Diodes via In Situ Ligand Exchange. *Adv. Mater.* **2020,** *32* (46), 2003805.

38. Imran, M.; Caligiuri, V.; Wang, M.; Goldoni, L.; Prato, M.; Krahne, R.; De Trizio, L.; Manna, L., Benzoyl Halides as Alternative Precursors for the Colloidal Synthesis of Lead-Based Halide Perovskite Nanocrystals. *J. Am. Chem. Soc.* **2018,** *140* (7), 2656-2664.

39. Nenon, D. P.; Pressler, K.; Kang, J.; Koscher, B. A.; Olshansky, J. H.; Osowiecki, W. T.; Koc, M. A.; Wang, L.-W.; Alivisatos, A. P., Design Principles for Trap-Free CsPbX3 Nanocrystals: Enumerating and Eliminating Surface Halide Vacancies with Softer Lewis Bases. *J. Am. Chem. Soc.* **2018,** *140* (50), 17760-17772.

40. Di Stasio, F.; Christodoulou, S.; Huo, N.; Konstantatos, G., Near-Unity Photoluminescence Quantum Yield in CsPbBr3 Nanocrystal Solid-State Films via Postsynthesis Treatment with Lead Bromide. *Chem. Mater.* **2017,** *29* (18), 7663-7667.

41. Ahmed, T.; Seth, S.; Samanta, A., Boosting the Photoluminescence of CsPbX3 (X = Cl, Br, I) Perovskite Nanocrystals Covering a Wide Wavelength Range by Postsynthetic Treatment with Tetrafluoroborate Salts. *Chem. Mater.* **2018,** *30* (11), 3633-3637.

42. Imran, M.; Ijaz, P.; Goldoni, L.; Maggioni, D.; Petralanda, U.; Prato, M.; Almeida, G.; Infante, I.; Manna, L., Simultaneous Cationic and Anionic Ligand Exchange For Colloidally Stable CsPbBr3 Nanocrystals. *ACS Energy Lett.* **2019,** *4* (4), 819-824.

43. Krieg, F.; Ochsenbein, S. T.; Yakunin, S.; ten Brinck, S.; Aellen, P.; Süess, A.; Clerc, B.; Guggisberg, D.; Nazarenko, O.; Shynkarenko, Y.; Kumar, S.; Shih, C.-J.; Infante, I.; Kovalenko, M. V., Colloidal CsPbX3 (X = Cl, Br, I) Nanocrystals 2.0: Zwitterionic Capping Ligands for Improved Durability and Stability. *ACS Energy Lett.* **2018,** *3* (3), 641-646.

44. Koscher, B. A.; Swabeck, J. K.; Bronstein, N. D.; Alivisatos, A. P., Essentially Trap-Free CsPbBr3 Colloidal Nanocrystals by Postsynthetic Thiocyanate Surface Treatment. *J. Am. Chem. Soc.* **2017,** *139* (19), 6566-6569.

45. De Roo, J.; Ibáñez, M.; Geiregat, P.; Nedelcu, G.; Walravens, W.; Maes, J.; Martins, J. C.; Van Driessche, I.; Kovalenko, M. V.; Hens, Z., Highly dynamic ligand binding and light absorption coefficient of cesium lead bromide perovskite nanocrystals. *ACS nano* **2016,** *10* (2), 2071-2081.

46. Shirai, M.; Kinoshita, H.; Tsunooka, M., Deblocking of poly(4-t-butoxycarbonyloxystyrene) using imino sulphonates as photoacid generators. *Eur. Polym. J.* **1992,** *28* (4), 379-385.

47. Lalevée, J.; Allonas, X.; Fouassier, J.-P.; Shirai, M.; Tsunooka, M., Photocleavage Processes in an Iminosulfonate Derivative Usable as Photoacid in Resist Technology. *Chem. Lett.* **2003,** *32* (2), 178-179.

48. Palm, A.; Werbin, H., The Infrared Spectra of Alpha and Beta Oximes. *Can. J. Chem.* **1953,** *31* (11), 1004-1008.

49. Goubeau, J.; Fromme, I., Beiträge zur Kenntnis der Stickstoff—Sauerstoff-Bindung. I. N-O-Bindungen ohne Mesomerie. *Zeitschrift für anorganische Chemie* **1949,** *258* (1-2), 18-26.

50. Perez De Berti, I. O.; Cagnoli, M. V.; Pecchi, G.; Alessandrini, J. L.; Stewart, S. J.; Bengoa, J. F.; Marchetti, S. G., Alternative low-cost approach to the synthesis of magnetic iron oxide nanoparticles by thermal decomposition of organic precursors. *Nanotechnology* **2013,** *24* (17), 175601.

51. Yang, D.; Li, X.; Zhou, W.; Zhang, S.; Meng, C.; Wu, Y.; Wang, Y.; Zeng, H., CsPbBr3 Quantum Dots 2.0: Benzenesulfonic Acid Equivalent Ligand Awakens Complete Purification. *Adv. Mater.* **2019,** *31* (30), 1900767.

52. Toso, S.; Baranov, D.; Altamura, D.; Scattarella, F.; Dahl, J.; Wang, X.; Marras, S.; Alivisatos, A. P.; Singer, A.; Giannini, C.; Manna, L., Multilayer Diffraction Reveals That

Colloidal Superlattices Approach the Structural Perfection of Single Crystals. *ACS Nano* **2021,** *15* (4), 6243-6256.

53. Dahl, J. C.; Wang, X.; Huang, X.; Chan, E. M.; Alivisatos, A. P., Elucidating the Weakly Reversible Cs–Pb–Br Perovskite Nanocrystal Reaction Network with High-Throughput Maps and Transformations. *J. Am. Chem. Soc.* **2020,** *142* (27), 11915-11926.

54. Liu, Z.; Bekenstein, Y.; Ye, X.; Nguyen, S. C.; Swabeck, J.; Zhang, D.; Lee, S.-T.; Yang, P.; Ma, W.; Alivisatos, A. P., Ligand Mediated Transformation of Cesium Lead Bromide Perovskite Nanocrystals to Lead Depleted Cs4PbBr6 Nanocrystals. *J. Am. Chem. Soc.* **2017,** *139* (15), 5309-5312.

55. Akkerman, Q. A.; D'Innocenzo, V.; Accornero, S.; Scarpellini, A.; Petrozza, A.; Prato, M.; Manna, L., Tuning the Optical Properties of Cesium Lead Halide Perovskite Nanocrystals by Anion Exchange Reactions. *J. Am. Chem. Soc.* **2015,** *137* (32), 10276-10281.

56. Nedelcu, G.; Protesescu, L.; Yakunin, S.; Bodnarchuk, M. I.; Grotevent, M. J.; Kovalenko, M. V., Fast Anion-Exchange in Highly Luminescent Nanocrystals of Cesium Lead Halide Perovskites (CsPbX3, X = Cl, Br, I). *Nano Lett.* **2015,** *15* (8), 5635-5640.

57. Li, X.; Yu, D.; Cao, F.; Gu, Y.; Wei, Y.; Wu, Y.; Song, J.; Zeng, H., Healing All-Inorganic Perovskite Films via Recyclable Dissolution–Recyrstallization for Compact and Smooth Carrier Channels of Optoelectronic Devices with High Stability. *Adv. Funct. Mater.* **2016,** *26* (32), 5903-5912.

58. Dong, Y.; Gu, Y.; Zou, Y.; Song, J.; Xu, L.; Li, J.; Xue, J.; Li, X.; Zeng, H., Improving All-Inorganic Perovskite Photodetectors by Preferred Orientation and Plasmonic Effect. *Small* **2016,** *12* (40), 5622-5632.

Chapter 5. Ligand-free direct optical lithography of bare colloidal nanocrystals via photo-oxidation of surface ions with porosity control

5.1. Introduction

Colloidal nanocrystals (NCs) have been extensively explored for their unique material properties, solution-processability, and device capabilities.[1-3] Most NC devices such as solar cells, photodetectors, and light-emitting diodes (LEDs) are fabricated and tested by the deposition of NCs as continuous thin films. However, the ability to form two-dimensional patterns of NCs is crucial for the assembly of more complex, real-world devices including LED and photodetector arrays,[4-5] multiplexed gas sensors,[6] and nanophotonic elements (e.g. waveguides, diffractive optics, and lasers). [7-9]

There are many well-developed methods for depositing NCs as a patterned layer. This includes ink-jet printing,[10-12] electron-beam lithography,[13-14] transfer printing,[15] nanoimprinting,[16] and photolithography.[17-19] Each of these patterning techniques has its advantages and limitations in terms of cost, scalability, pattern resolution, and generality of approach. A particularly important factor to consider is the ligand environment of the NCs after patterning. In many cases, NCs are patterned in a matrix of long-chain organic ligands or polymer additives which limits the NC electronic coupling, lower the temperature stability of the film, and significantly reduce the packing fraction of the NCs.

In our lab, we have been developing chemical methods that enable the direct optical lithography of functional inorganic nanomaterials (DOLFIN). This resist-free approach involves exploring suitable photosensitive ligands or additives that modulate the surface charge/polarity of semiconducting, metal oxide and lead halide perovskite NCs.[5, 9, 20-22] A key philosophy of our

patterning approach is the use minimal additives in our process to maximize the packing density and coupling of patterned NC films. To this end, it is useful to utilize NCs that have their organic chains removed via ligand stripping approaches, giving "bare" NCs that are charge-stabilized with a non-coordinating anion such as BF_4^-.[23-27] Previously, we have found that "bare" NCs can be patterned by introducing a photo-active chemical compound that reduces the surface charge upon photodecomposition.[9, 21] However, another unexplored patterning mechanism involves harnessing photogenerated holes and electrons in the NCs to drive chemical reactions on the NC surface (such as photo-oxidation), which subsequently changes the NC solubility and formation of photo-patterns.

The photo-induced oxidation of semiconductor NCs has been carefully studied due to the importance of surface chemistry for achieving optimal optoelectronic and luminescent performance. X-ray photoelectron spectroscopy (XPS) of organic-capped CdSe NCs has shown the presence of SeO_2 upon irradiation in air,[28] while UV-vis studies has shown blue-shifting, broadening and reduction of the excitonic features upon prolonged exposure to light.[29] Similar effects have been found in aqueous dispersions of CdS NCs. [30-31] Besides that, the photo-oxidation of InP NCs and nanowires in the presence of HF is a common technique to increase their PL quantum yield. [32-34] In addition, surface oxidation of colloidal nanocrystals can be used to induce oriented attachment to create hierarchical self-assembled structures.[35] Although the photo-oxidation of various NCs have been studied and used to create self-assembled hierarchical structures, it has not been used to modulate the NC solubility for direct patterning of arbitrary structures.

Another advantage of using colloidal NCs in devices is the ability to independently control the nano- and meso-scale morphology of the NC films. The crystallinity, crystallite size, and

composition of the film can be precisely controlled by using nanocrystal of different size and composition and can take advantage of nearly 30 years of synthetic development for colloidal inorganic nanocrystals. Further hierarchical structures can be developed using a variety of thin film modification strategies. For instance, there is a well-developed route to introduce mesoscale porosity into films of bare NCs via polymer templating. [36-40] This first involves mixing the NCs with micelles made of amphiphilic block copolymers. The mixture is then deposited as a film that consists of NCs assembled around the micelle template. Upon removal of this template, an open porous network of NCs is formed. On the other hand, post-processing methods such as thermal annealing and hot isostatic pressing can be used to decrease the NC film porosity and allow for further densification of NC films. These approaches have yet to be integrated with strategies to lithographically pattern nanocrystal films. This would enable applications which simultaneously require hierarchical mesoscale structures and microscale patterned elements such as porous waveguides,[41-42] multiplexed gas sensors,[6] and diffractive optical elements with refractive index tunability. [43-44]

Here, we explore the ligand-free direct optical lithography of colloidal NCs through the photo-oxidation of surface ions. The native NC ligands are first stripped by a strong acid such as HBF_4 in DMF to yield electrostatically stabilized, bare NCs. The NCs are deposited as a film and irradiated selectively to induce local photo-oxidation of surface atoms on portions of the film which remain insoluble upon development with DMF. High-quality and high-resolution (~1 μm feature sizes) patterns are achievable using ZnSe-BF_4 NCs and 405 nm light exposure. This approach is also generalizable to other bare NCs such as CdSe, ZnS, InP and CeO_2 NCs. Furthermore, ZnSe NCs can be used as a sensitizer/spacer to enable the patterning of other NCs such as HfO_2, ZrO_2, and CdSe/CdS NCs. We used XPS and FTIR to determine that this patterning

works by the oxidation of surface ions (e.g., Se^{2-} is oxidized to SeO_2). Finally, we demonstrate methods to tune the porosity of the patterned NC film through block-copolymer templating and hot isostatic pressing. This allows the refractive index of a ZnSe NC patterns to be tuned within a range of $\Delta n \approx 0.23$, which extends its versatility for nanophotonic and gas sensing applications.

5.2. Photo-oxidation patterning of NCs

The patterning process via photo-oxidation is shown in **Figure 5.1.** Colloidal NCs capped with long-chain organic ligands are first synthesized by literature methods. The organic ligands are then removed through a single-phase ligand exchange by adding HBF_4 in DMF to colloidal NCs dispersed in toluene, causing the NCs immediately precipitate out. To remove the displaced organic ligands and excess ions, the NCs are washed several times by dissolving them in DMF followed by precipitation with toluene. The bare NCs are finally dispersed in DMF with a concentration of about 5–10 wt% (50–100 mg/mL).

The bare NCs are then spincoated as a thin film, which is then immediately irradiated selectively using a photomask and a suitable light source (405 nm light for most NCs, 254 nm for ZnS NCs). This leads to the local photo-oxidation of surface ions of the irradiated NCs, reducing their solubility. The film is then developed in DMF, removing unexposed areas while leaving the irradiated NCs behind as a patterned layer.

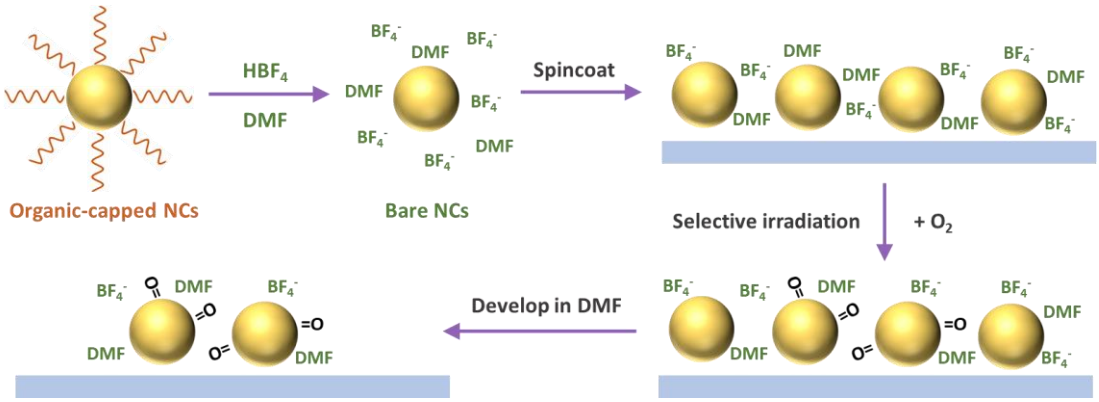

Figure 5.1. Schematic of the patterning process via surface photo-oxidation of bare NCs.

Micro-scale patterns of ZnSe-BF_4 NCs obtained through the photo-oxidation process are shown in **Figure 5.2**. The optical microscope images show uniform layers with a pattern resolution down to 2 μm and feature sizes as small as 1 μm (the smallest feature of our photomask). The generality of this approach is demonstrated by the patterning of various types of NCs and changing the identity of the counterion. For instance, the patterning process also works for ZnSe NCs that have been stripped with triflic (trifluoromethanesulfonate) acid instead of HBF_4 (**Figure 5.3A**). This suggests that the patterning process is not unique to the chemistry of a specific counterion. We also show the patterning of other bare semiconductor and oxide NCs such as CdSe, ZnS, InP and CeO_2 NCs (**Figure 5.3B–E**). Although the patterning dose changes depending on the identity of the NCs, the successful patterning of all these NCs support a general patterning approach that should be extendable to other types of NCs with some optimization. The only obvious requirement is that the NCs need to have significant absorption at the irradiation wavelength.

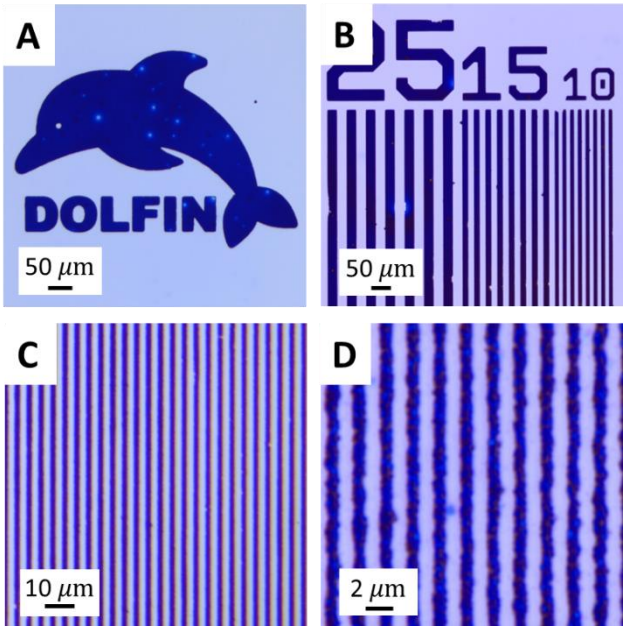

Figure 5.2. Optical microscope images showing patterns of ZnSe-BF_4 NCs obtained by photo-oxidation patterning.

For bare NCs that were not patternable on their own, we were able to pattern them by mixing with NCs that were patternable. For instance, visibly transparent HfO_2 and ZrO_2 NCs can be patterned by mixing in about 25 wt% of ZnSe NCs that act as a sensitizer to enable patterning with 405 nm light (**Figure 5.3F-G**). The quality and resolution of the patterns remain good as shown by the patterning of 1 μm features (**Figure 5.3F, inset**), although a significantly higher dose (~1.8 J/cm^2) is required. Besides that, we show that luminescent CdSe/CdS-BF_4 NCs can also be patterned by mixing it with ZnSe-BF_4 NCs (**Figure 5.3H**). CdSe/CdS-BF_4 NCs were difficult to pattern on its own through this approach due to two hypothesized reasons: (1) the size of these core-shell NCs are significantly larger than the core NCs, which leads to significantly stronger van der Waals forces and irreversible aggregation upon deposition in the absence of any additives, and (2) higher photoluminescence (PL) quantum yield of these QDs leads to a lower photo-oxidation efficiency due to preferential localization of the holes on the CdSe core rather than being available

for surface oxidation. Thus, the addition of ZnSe-BF_4 NCs is required to overcome these effects by serving as a spacer and sensitizer.

There are several requirements we have empirically determined for achieving high-quality patterns through this approach. First, it is important that non-irradiated NCs are sufficiently spaced apart prior to the development step to avoid getting trapped in the deep primary minimum of a DLVO potential. In previous patterning approaches using a photo-sensitive additive, the un-irradiated additive molecule/ions play the role of spacers between NCs which prevents the NCs from falling into the primary minimum and subsequently irreversible aggregating.[21] In this ligand-free approach, this role falls on the DMF molecules that are adsorbed on the NC surface as L-type ligands, as previously studied.[23, 26] The downside of this is that DMF slowly desorbs from the NC surface over time, leading to the irreversible aggregation and insolubility of the whole film after a certain period of time. Hence, it is important that the deposited NC film is promptly irradiated and developed to prevent this from occurring. Alternatively, this issue should be mitigated by controlling the saturation of DMF in the atmosphere or by including an L-type ligand with higher boiling point or stronger binding affinity to the NC surface.

Another unexpectedly important part of this process is the number of washing cycles after ligand stripping, which dictates how many free ions remain in the solution (and in the deposited film). We found that the highest sensitivity was achieved when the NCs were washed extensively (more than 6 rounds of DMF/toluene washing). We hypothesize that this also relates to a spacing effect: excess free ions also serve as a spacer that keeps NCs apart, increasing their solubility. This weakens the effect of photo-oxidation aggregation and reduces its sensitivity. With extensive washing, doses as low as 90 mJ/cm^2 and 20 mJ/cm^2 were sufficient to pattern ~100 nm thick film of ZnSe NCs and ZnS NCs, respectively. These doses are comparable to other DOLFIN

approaches that utilize photosensitive ligands or additives,[9, 21] and comparable or lower than the dosage required for patterning commercial polymer photoresists. [45]

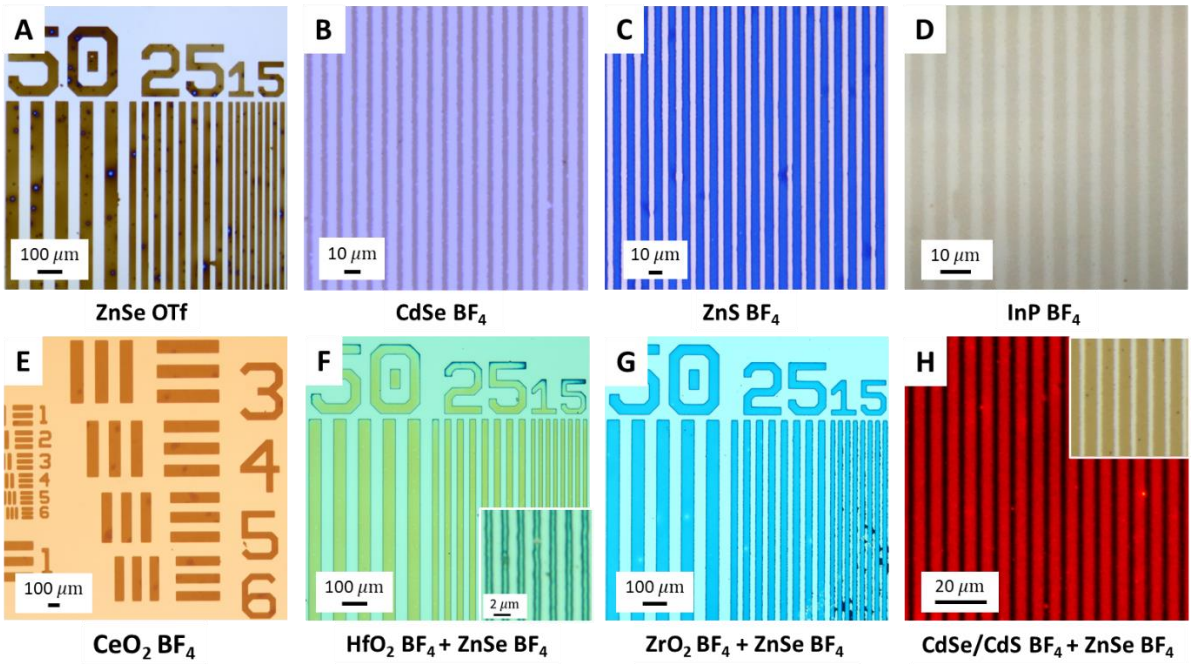

Figure 5.3. Optical microscope images of patterns made of various NCs and counterions. (A) Patterns of ZnSe NCs with triflate (OTf^-) counterions. (B–E) Patterns of CdSe, ZnS, InP and CeO_2 NCs with BF_4^- counterions. (F–G) Patterns of HfO_2 (F) and ZrO_2 NCs (G) mixed with ZnSe NCs (as the sensitizer). (H) PL image of patterns of CdSe/CdS NCs mixed with ZnSe NCs. Inset: bright-field microscope image.

5.3. Investigating the mechanism of photo-oxidation patterning

To elucidate the patterning mechanism, we investigated changes to the NCs during the photo-irradiation process. UV-vis spectroscopy showed small blue-shift and reduction in the absorbance of ZnS, CdSe and ZnSe NCs upon irradiation with light (**Figure 5.4A–C**). This is consistent with previous reports on the photo-oxidation of colloidal NCs. [29, 31] We also found that the photo-degradation is much more significant for bare NCs compared to organic-capped NCs (**Figure 5.5**). This is reasonable since bare NCs lack the protecting organic ligands that can repel

most of the oxygen from interacting with the NC surface. Also, no significant change to the absorption features is observed upon the irradiation of ZnSe-BF_4 NCs in a nitrogen atmosphere (**Figure 5.4D**). To conclusively demonstrate the importance of oxygen for this patterning mechanism, we carried out control experiments that involve the irradiation of ZnSe-BF_4 NC film in a nitrogen atmosphere (**Figure 5.6**). Our results show that irradiation in air-free conditions does not result in a solubility change of the ZnSe-BF_4 NC film even at a high dose (~1.8 J/cm^2, 60 s exposure time). In contrast, an exposure dose of 0.15 J/cm^2 to a similar ZnSe NC film in air leads to the clear reduction of colloidal solubility.

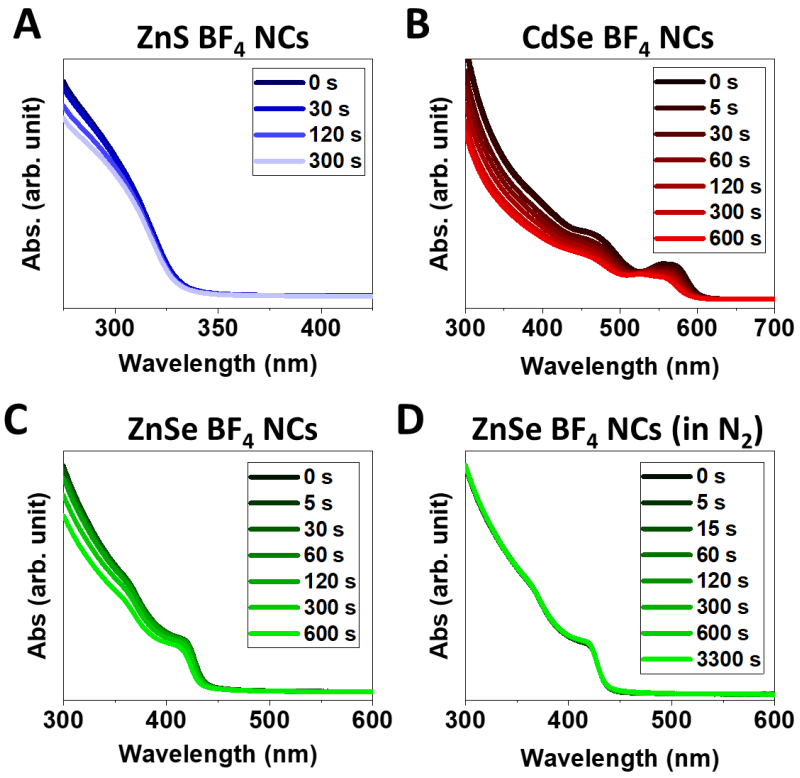

Figure 5.4. UV-vis spectra showing changes in the NC absorption spectra upon increasing light exposure. A 254 nm light source (~6 mJ/cm^2) was used to irradiate the ZnS NCs (A), while a 405 nm light (~30 mJ/cm^2) source was used for CdSe and ZnSe NCs (B–D). Exposures done in air (A–C) showed a clear blue-shift in the spectra, while exposure in a nitrogen atmosphere (D) shows no pronounced changes to the spectrum.

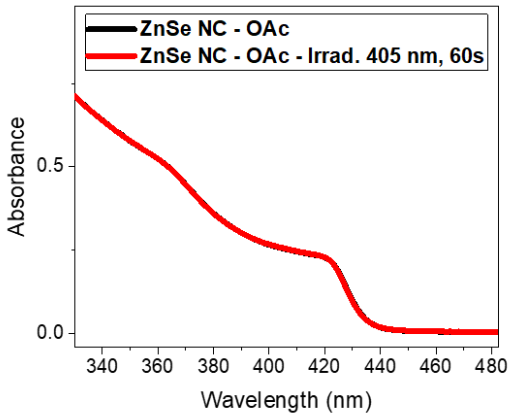

Figure 5.5. UV-vis of oleate-capped NCs in toluene before and after irradiation.

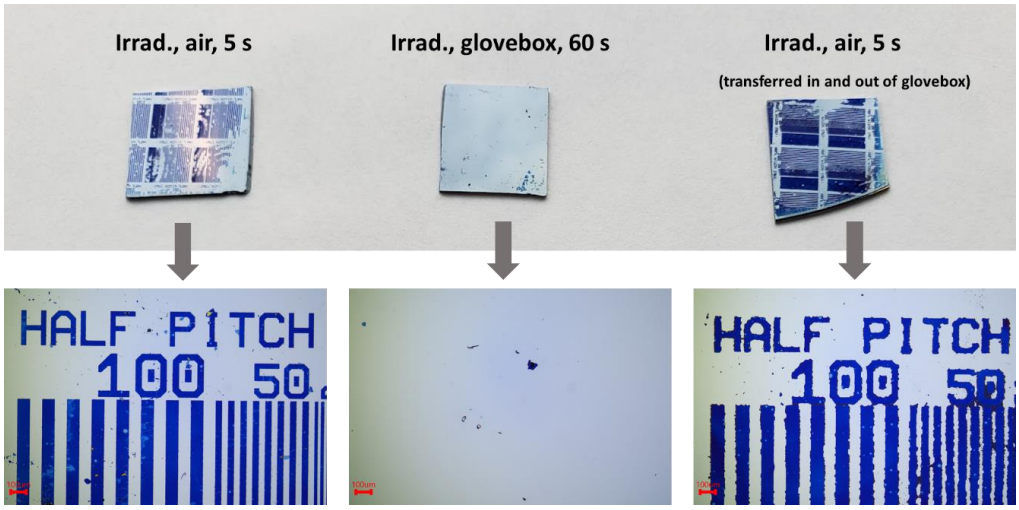

Figure 5.6. Pictures and optical microscope images upon irradiation of ZnSe-BF_4 NCs in air or in air-free conditions.

We also carried out X-ray photoelectron spectroscopy (XPS) to reveal changes in the chemical bonding of surface ions (**Figure 5.7A–B**). Before irradiation, the Se 3d region of ZnSe-BF_4 NCs show peaks that can be primarily attributed ZnSe (Se $3d_{5/2}$: 54.10 eV; Se $3d_{3/2}$: 54.96) and potentially a small amount of Se/SeOH (Se $3d_{5/2}$: 55.20 eV; Se $3d_{3/2}$: 56.06).[46] Upon irradiation, new peaks in the Se 3d region were observed (Se $3d_{5/2}$: 59.0 eV; Se $3d_{3/2}$: 59.86) that

corresponds to SeO_2 and is consistent with previous reports.[28, 46-47] At the same time, there is also a perceivable increase in the Se/SeOH peaks upon irradiation. These observations are consistent with the photo-oxidation of surface Se^{2-} ions into several different oxidation species. On the other hand, we do not observe any noticeable change in the oxidation state of Zn based on the the XPS spectra for the Zn $2p_{3/2}$ core level.

FTIR spectroscopy was also used to investigate changes in the ligand chemistry (**Figure 5.7C**). As-deposited CdSe-BF_4 NCs show the distinctive peaks of DMF (e.g., 1650 cm^{-1}, C=O stretch), which confirm that there is adsorbed DMF in the NC film. FTIR spectra of NC films also show the peak from the BF_4^- counterions at ~1040 cm^{-1}. Upon drying in air for 3 days, the intensities of DMF-related absorption peaks are reduced significantly compared to the BF_4^- peaks. After irradiating this dried NC film with 405 nm light for 2 mins (~3.6 J/cm^2), there is no observable change to the BF_4^- peaks. Hence, we deduce that the counterions do not play a significant role in the photo-oxidation patterning mechanism.

We also carried out dynamic light-scattering (DLS) and zeta-potential experiments to probe the changes in colloidal stability of the bare NCs upon irradiation. Before irradiation, DLS shows that ZnSe-BF_4 NCs have a hydrodynamic radius of ~7 nm and no presence of larger aggregates (**Figure 5.7D**). Upon increasing durations of irradiation, peaks at larger sizes emerge and intensify, showing the effect of photo-induced NC aggregation. Interestingly, the measured zeta potential of the NCs during this photo-aggregation process was mostly unchanged at ~50 mV (**Figure 5.8**). This contrasts with other pattering approaches that show the reduction of the zeta potential due to neutralization of the surface charge.[9] Hence, it appears that the aggregation of NCs by photo-oxidation does not stem from the neutralization of the positive surface charges.

To account for all these experimental observations, we hypothesize that the photo-oxidation patterning of NCs may be due to the desorption of DMF molecules due to steric hindrance by oxidized species on the NC surface. For instance, the oxidation of surface Se^{2-} into bulkier SeOH or SeO_3^{2-} groups will block the binding of DMF ligands to the surface metal sites. This would be consistent with the dramatic reduction in NC solubility without any progressive neutralization of the surface charge.

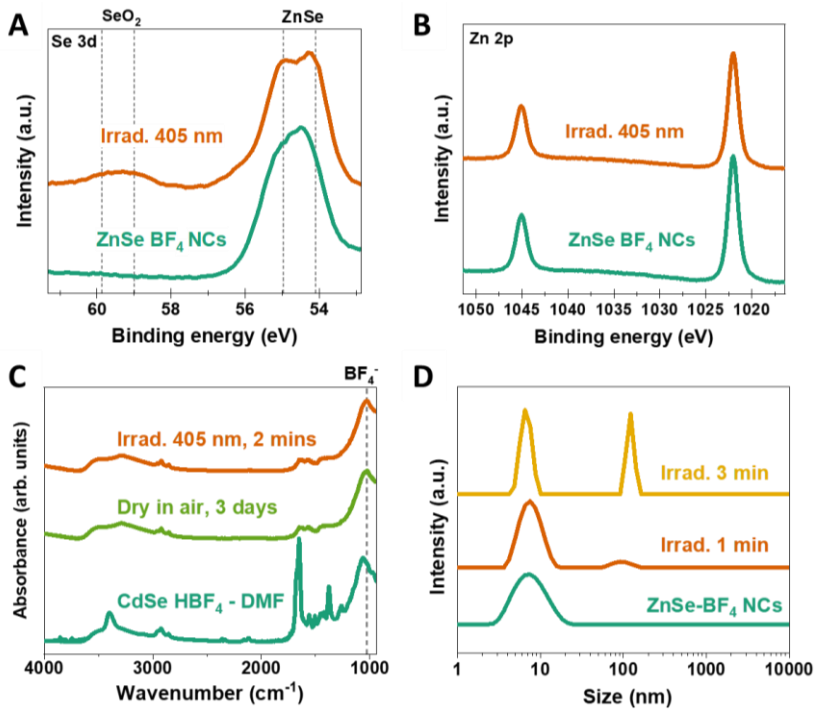

Figure 5.7. Further investigation of the pattering mechanism via photo-oxidation. (A–B) XPS spectra of the Se 3d and Zn 2p region for ZnSe-BF_4 NCs before and after irradiation. (C) FTIR of CdSe-BF_4 NCs right after spincoating, after drying for 3 days and after irradiation. (D) DLS of ZnSe-BF_4 NCs upon increasing irradiation times showing the light-induced aggregation of the NCs.

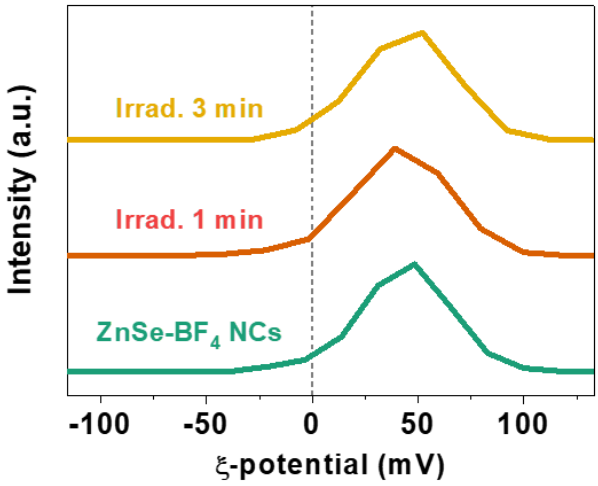

Figure 5.8. Zeta potential measurements of ZnSe-BF_4 NCs upon various irradiation times with 405 nm light.

5.4. Porosity control of patterned NC films

The porosity of NC films is an important parameter for the functionality of various NC devices. For instance, the porosity has a big influence on the accessibility of the NC surface upon deposition, which is crucial for resistive gas sensors and other NC devices. In this case, it is often beneficial to have a higher porosity to allow for quick and efficient gas accessibility to the NC surface sites. For other applications, it is more desirable to have the highest NC packing density as possible. As an example, a dense NC film is desirable for optical applications which benefit from a high refractive index for light confinement (e.g., for waveguides).

Here, we demonstrate two approaches to modulate the porosity of patterned NC films. To increase the porosity of our patterned films, we show that our photo-oxidation patterning process is compatible with established routes of introducing mesopores into NC films by polymer templating (**Figure 5.9A**). [36-40] In this approach, block-copolymer micelles are mixed with the bare NCs in DMF and deposited as a film. Subsequent local irradiation of the NC film leads to the oxidation of the exposed NCs and decrease of solubility in DMF. Upon development with DMF,

both the NCs and polymer in the unexposed parts of the film are fully dissolved away. In contrast, in the irradiated parts of the film, only the polymer is washed away while the templated NCs remain insoluble, forming a patterned mesoporous NC film. This ability to maintain a mesoporous structure that does not collapse suggests that the oxidative photopatterning results in relatively strong interactions bonds between NCs.

Optical microscopy shows that micro-patterns of mesoporous ZnSe NC films can be formed (**Figure 5.9B**). Notably, a higher dose of ~2.7 J/cm^2 is required for patterning, which we attribute to the effect of hydrophilic segments of the polymer intercalating between NCs and reducing the photo-aggregation efficiency. SEM imaging confirms the presence of 50–100 nm mesopores within the patterned structure (**Figure 5.9C**), which is also consistent with the decrease in the refractive index of the mesoporous film ($n = 1.87$), which is appreciably lower than that of a standard, non-templated ZnSe NC film ($n = 1.94$), as measured by ellipsometry (**Figure 5.9D**).

On the other hand, we carried out preliminary experiments on the use of hot isostatic pressing (HIP) to increase the densification of patterned NC films. HIP is a well-established densification technique that uses a combination of elevated temperatures and high gas pressures to remove pores from a material while reducing undesirable deformation.[48] We subjected ZnSe-BF_4 NC films to HIP at 270 °C and 15,000 psi for 16 h and found that the NC patterns remained well preserved during this treatment (**Figure 5.9D**). SEM imaging showed significant densification of the NC film with the notable absence of the 10–20 nm pores found in untreated ZnSe-BF_4 NC films (**Figure 5.9F–G**). In agreement with this, the refractive index after HIP increased to $n = 2.10$, which is significantly higher than the refractive index of $n = 1.97$ obtained upon the simple thermal treatment of ZnSe-BF_4 NCs under atmospheric pressure (**Figure 5.9D**) at an identical temperature. X-ray diffraction (XRD) showed that there was no significant change to the width of

the ZnSe zinc-blende peaks, indicating the lack of grain growth under our HIP conditions (**Figure 5.10**).

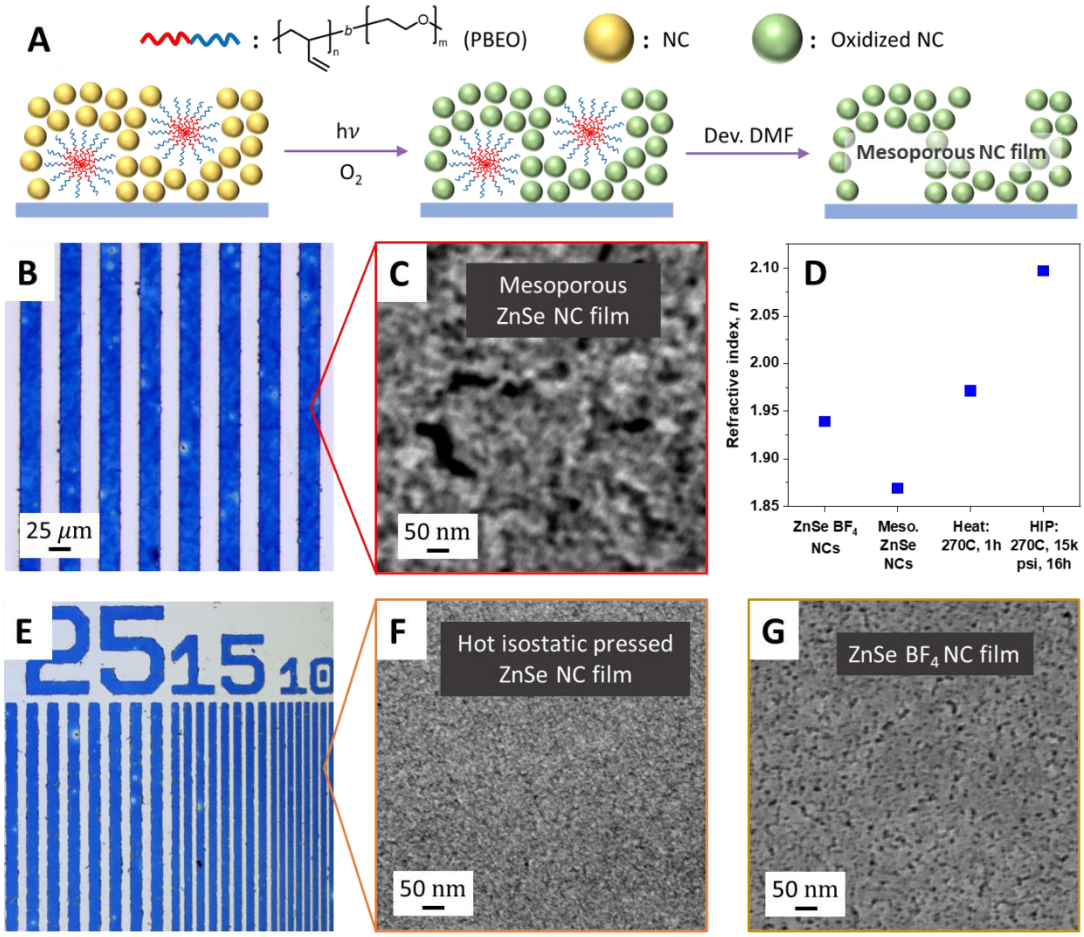

Figure 5.9. Tuning the porosity and refractive index of patterned ZnSe NC films. (A) Scheme showing a film of NCs mixed with poly(1,2-butadiene)-b-poly(ethylene oxide) (PBEO), followed by photo-oxidation patterning and development to produce a mesoporous patterned film. (B–C) Optical microscope and SEM images of patterned mesoporous ZnSe NC layers. The mesoporosity was introduced by adding 14 wt% PBEO to the ZnSe-BF_4 NC solution. (D) Refractive indices of ZnSe NC films upon mesoporous templating, heating at 270 °C and hot isostatic pressing at a temperature of 270 °C and a pressure of 15,000 psi. (E–F) Optical microscope and SEM images of ZnSe NCs after hot isostatic pressing (270 °C; 15,000 psi). (G) SEM image of a ZnSe-BF_4 NC film with no templating or post-processing.

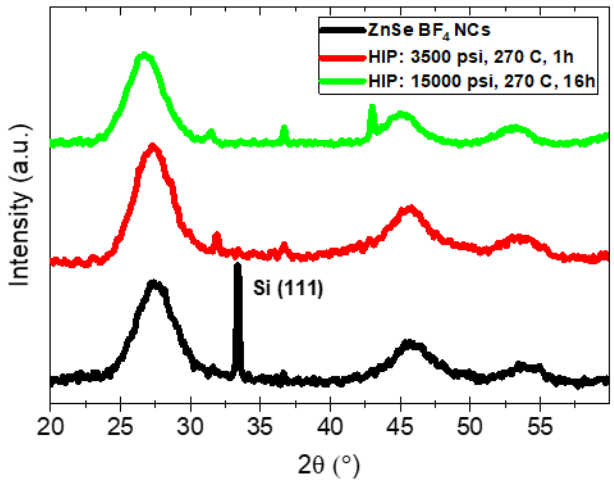

Figure 5.10. XRD spectra before and after hot isostatic pressing treatment of ZnSe-BF_4 NCs.

We have shown that the porosity of patterned NC films can be tuned significantly by block-copolymer templating and HIP. Using these two approaches, the refractive index of a ZnSe-BF_4 NC film can be tuned within a range of $\Delta n \approx 0.23$ (from 1.87 to 2.10), simply by controlling the porosity and densification of the film. Future work involves exploring a wider temperature and pressure range used in the HIP process. This may enable grain growth and further densification of the NC films to approach the refractive index of bulk inorganic materials. On the other hand, the meso-porosity of the NC film may be further optimized by tuning the amount of polymer added as well as the chemical interactions between NC surface and the polymer.[36-37]

5.5. Summary

In summary, we demonstrate the direct optical lithography of ligand-stripped, all-inorganic colloidal NCs via the photo-oxidation of surface ions. We show the high-quality patterning of a variety of NCs such as ZnSe, CdSe, CdS, InP and CeO_2 NCs, as well as mixtures of NCs. We also probed the chemical changes induced during the patterning process and our results are consistent

with the oxidation of surface ions by molecular oxygen that leads to the aggregation of NCs and their reduction of solubility in polar solvents. Finally, we used polymer templating and hot isostatic pressing to modulate the porosity and refractive index of the patterned NC films.

5.6. Materials and methods

Chemicals. *N*,*N*-Dimethylformamide (DMF, anhydrous, 99.8%), tetrafluoroboric acid diethyl ether complex, zinc carbonate basic (purum p.a.), cadmium oxide (>99.99%), zinc chloride (>98%), oleic acid (technical grade, 90%), oleylamine (technical grade, 70%), trioctylphosphine oxide (99%), and 1-octadecene (technical grade, 90%) were purchased from Millipore Sigma. Trifluoromethanesulfonic acid (99%), sulfur flakes (99.998%), and selenium powder (>99.5%, 200 mesh) were purchased from Fisher Scientific. Poly(1,2-butadiene)-b-poly(ethylene oxide) with a mass ratio of PB(5200)-b-PEO(4500) was obtained from Polymer Source, Inc.

Nanocrystal syntheses. ZnSe NCs were synthesized by a scaled-up, modified procedure from Flamee *et al*.[49] Briefly, zinc carbonate basic (6.4 mmol, 3.71 g), oleic acid (96 mmol, 27.1 g, 30.2 mL) and octadecene (200 mL) was loaded in a 500 mL 3-neck flask. The mixture was degassed at 120 °C for a few minutes and then heated to 200 °C under N_2 to form a clear Zn(oleate)$_2$ solution. Upon reaching 200 °C, the heating was stopped immediately, and the flask cooled to 90 °C. The solution was then degassed at 90 °C for 1 h under vacuum. In the meantime, and ODE-Se suspension was made in the glovebox. This involves the sonication of Se powder (24 mmol, 1.89 g, 200 mesh) in ODE (20 mL). After degassing the Zn(oleate)$_2$ solution for an hour, it was heated up to 270 °C and the ODE-Se suspension was swiftly injected. The solution was heated at 260 °C for 25 min. The solution turns from a black suspension to dark red and then to light orange. Upon

cooling, the NCs were washed several times with IPA and MeOH as the non-solvent and toluene as the solvent. The purification process required heating the solution to 70 °C in a water bath to help solubilize the unreacted Zn(oleate)$_2$ from the precipitated NCs.

CdSe NCs were synthesized by a scaled-up, modified procedure from Flamee *et al*.[49] Briefly, cadmium oxide (50 mmol, 6.42 g), oleic acid (150 mmol, 47 mL) and ODE (50 mL) we loaded in a 3-neck flask. The solution was degassed at 115 °C for 2 hours and then heated to 270 °C to form the cadmium oleate complex. Upon reaching 270°C, the solution was immediately cooled down to 115 °C. Then, the solution was degassed for another 1 hour at 115 °C. In the meantime, a Se-ODE solution was prepared by sonicating Se powder (30 mmol, 2.37 g, 200 mesh) in ODE (6 mL). After the cadmium oleate solution was degassed for an hour, it was heated to 270 °C and the Se-ODE swiftly injected. The solution was heated at 260 °C for 10 mins before being cooled down. The NCs were purified several times with IPA and MeOH as the non-solvent and toluene as the solvent.

ZnS NCs were synthesized by a scaled-up, modified procedure from Herron *et al*.[50] Briefly, $ZnCl_2$ (60 mmol, 8.18 g), oleic acid (50 mL), oleylamine (50 mL) and trioctylphosphine oxide (60 mmol, 23 g) were added to a 3-neck flask and degassed at 140 °C for 2.5 hrs. In the meantime, an OAm-S solution was made by adding sulfur flakes (30 mmol, 0.96 g) to degassed oleylamine (20 mL) and heating at 125 °C for 1 hour. After the zinc oleate mixture has been degassed, it was heated to 320 °C under N_2. The OAm-S was swiftly injected at 320 °C and the solution was heated at 320 °C for 7 mins. The NC solution was then cooled and washed several times with EtOH and MeOH.

Tetragonal zirconia NCs capped with TOPO were synthesized by a procedure by Joo *et al*.[51] Briefly, trioctylphosphine oxide (30 g) was degassed at 80 °C for 1 hour in a 3-neck round-

bottom flask. The flask was sealed, brought into a glove box and $Zr(O\text{-}iPr)_4 \cdot (IPA)$ (2.34 g, 6 mmol) and $ZrCl_4$ (1.75 g, 7.5 mmol) was added. The mixture was then degassed again at 70 °C for 30 mins. Under nitrogen, the solution was heated to 340 °C and held there for 2 hours. The NCs were purified several times by acetone and toluene.

Monoclinic HfO_2 NCs capped with TOPO were synthesized by a procedure by Tirosh et al.[52] Briefly, trioctylphosphine oxide (30 g) was degassed at 80 °C for 1 hour in a 3-neck round-bottom flask. The flask was sealed, brought into a glove box and $Hf(O\text{-}iPr)_4 \cdot (IPA)$ (2.85 g. 6 mmol) and $HfCl_4$ (1.95 g, 6 mmol) was added. The mixture was then degassed again at 70 °C for 30 mins. Under nitrogen, the solution was heated to 360 °C and held there for 2 hours. The NCs were purified several times by acetone and toluene.

Ligand stripping of NCs. Organic-capped colloidal ZnSe, ZnS, CdSe, ZrO_2, HfO_2 and CdSe/CdS NCs were synthesized by modified recipes from published literature. More details on the syntheses can be found in the supporting information. InP NCs were obtained from Nanosys and used after several rounds of washing.

HBF_4 in DMF (5 wt%, 0.57 M) was first made by adding HBF_4-diethyl ether complex solution dropwise to DMF with a volume ratio of 1:9 (*caution: vigorous reaction*). About 0.1 mL of this HBF_4 solution was added to a solution of organic-capped NCs dispersed in 1 mL toluene (~20 mg/mL). The addition of acid immediately induced the precipitation of the NCs. After vortexing for 20 s, the NC suspension was centrifuged. The supernatant was discarded, and the NC residue was washed between 3–6 times with DMF/toluene, depending on the type of NC. (For ZnSe NCs, 6 washing cycles were done, each involving 0.5 mL DMF followed by ~1.5 mL of toluene.) After washing, the NCs were finally dispersed in DMF at a concentration of about 50–

100 mg/mL. This ligand-stripping procedure was scaled up by a volume factor of 10 without any substantial effect on the colloidal stability. For ligand-stripping with triflic acid, the same procedure was used except using triflic (trifluoromethanesulfonic) acid dissolved in DMF (0.5 M).

Photo-oxidation patterning. Silicon wafers with a native oxide layer were cut into 1 × 1 inch substrates and sonicated in acetone (5 min) and ethanol (5 min). The substrates were then subjected to oxygen plasma treatment for about 10 mins. The bare NCs were then deposited onto the substrate by spincoating. The substrate was then bound between a glass slide and a patterned chrome mask using two binder clips. This stack was then exposed to 405 nm light (M405LP1-C1, Thorlabs, measured power density ~30 mW/cm^2) or a low-pressure mercury vapor grid lamp emitting at 254 nm (~6 mW/cm^2, Jelight Company, Inc). After exposure, the substrate was immersed into a DMF developer for ~10 s and then dried with a N_2 gun. Mixtures of bare NCs were obtained by mixing and vortexing two different NCs together and using the same patterning procedure as above.

Patterning of mesoporous NC films. Poly(1,2-butadiene)-b-poly(ethylene oxide) (PBEO) with a mass ratio of PB(5200)-b-PEO(4500) was dissolved in DMF (2.5 wt%) and stirred for a few hours at room temperature. The PBEO solution was then added to a solution of ZnSe-BF_4 NC solution to obtain 14 wt% of PBEO with respect to NCs. This mixture was then vortexed and then patterned according to the same procedure as above.

Hot isostatic pressing (HIP) of NC films. Patterned ZnSe-BF_4 NC films on Si substrates were inserted into a stainless-steel reactor and sealed. At room temperature, the pressure in the

reactor was increased to about 8,000 psi using ultra-high purity N_2 gas with the aid of a pressure booster. The reactor was then heated to 270 °C, which also led to the increase in pressure to about 15,000 psi. The HIP treatment was carried out for 16 h, after which the reactor was cooled down and depressurized.

Characterization techniques. Optical absorption spectra of NP solutions or films were collected using a Shimadzu UV-3600i Plus UV-Vis-NIR spectrophotometer in transmission mode. Optical microscope images and fluorescent images were obtained using an Olympus BX51 microscope. The contrast and brightness of the optical images were manipulated using the camera software or with ImageJ. Wide angle powder X-ray diffraction (XRD) patterns were collected using a Rigaku Miniflex diffractometer with a Cu Kα X-ray sourc. Infrared absorption spectra of thin films were obtained with a Thermo Nicolet iS50 Advanced FTIR in transmission mode (using a ZnSe substrate from Crystran Ltd.). Scanning electron microscope (SEM) images were acquired using a Carl Zeiss MERLIN field emission SEM. Single-wavelength (633 nm) refractive index of films was determined with a Gaertner Waferskan ellipsometer. The hydrodynamic size of colloidal nanoparticles was obtained with a Malvern Zetasizer Nano ZS. XPS analysis was performed on a Kratos Axis Nova spectrometer using monochromatic Al Kα source (1486.6 eV).

5.7. Chapter bibliography

1. Talapin, D. V.; Lee, J.-S.; Kovalenko, M. V.; Shevchenko, E. V., Prospects of Colloidal Nanocrystals for Electronic and Optoelectronic Applications. *Chem. Rev.* **2010,** *110* (1), 389-458.

2. Arquer, F. P. G. d.; Talapin, D. V.; Klimov, V. I.; Arakawa, Y.; Bayer, M.; Sargent, E. H., Semiconductor quantum dots: Technological progress and future challenges. *Science* **2021,** *373* (6555), eaaz8541.

3. Kagan, C. R.; Lifshitz, E.; Sargent, E. H.; Talapin, D. V., Building devices from colloidal quantum dots. *Science* **2016,** *353* (6302), aac5523.

4. Kim, J.; Kwon, S.-M.; Kang, Y. K.; Kim, Y.-H.; Lee, M.-J.; Han, K.; Facchetti, A.; Kim, M.-G.; Park, S. K., A skin-like two-dimensionally pixelized full-color quantum dot photodetector. *Science Advances* **2019,** *5* (11), eaax8801.

5. Cho, H.; Pan, J. A.; Wu, H.; Lan, X.; Coropceanu, I.; Wang, Y.; Cho, W.; Hill, E. A.; Anderson, J. S.; Talapin, D. V., Direct Optical Patterning of Quantum Dot Light-Emitting Diodes via In Situ Ligand Exchange. *Adv. Mater.* **2020,** *32* (46), 2003805.

6. Yang, D.; Fuadi, M. K.; Kang, K.; Kim, D.; Li, Z.; Park, I., Multiplexed Gas Sensor Based on Heterogeneous Metal Oxide Nanomaterial Array Enabled by Localized Liquid-Phase Reaction. *ACS Appl. Mater. Interfaces* **2015,** *7* (19), 10152-10161.

7. Prins, F.; Kim, D. K.; Cui, J.; De Leo, E.; Spiegel, L. L.; McPeak, K. M.; Norris, D. J., Direct Patterning of Colloidal Quantum-Dot Thin Films for Enhanced and Spectrally Selective Out-Coupling of Emission. *Nano Lett.* **2017,** *17* (3), 1319-1325.

8. Gheshlaghi, N.; Foroutan-Barenji, S.; Erdem, O.; Altintas, Y.; Shabani, F.; Humayun, M. H.; Demir, H. V., Self-Resonant Microlasers of Colloidal Quantum Wells Constructed by Direct Deep Patterning. *Nano Lett.* **2021**.

9. Pan, J.-A.; Rong, Z.; Wang, Y.; Cho, H.; Coropceanu, I.; Wu, H.; Talapin, D. V., Direct Optical Lithography of Colloidal Metal Oxide Nanomaterials for Diffractive Optical Elements with 2π Phase Control. *J. Am. Chem. Soc.* **2021,** *143* (5), 2372-2383.

10. Zhang, L.; Chao, D.; Yang, P.; Weber, L.; Li, J.; Kraus, T.; Fan, H. J., Flexible Pseudocapacitive Electrochromics via Inkjet Printing of Additive-Free Tungsten Oxide Nanocrystal Ink. *Advanced Energy Materials* **2020,** *10* (17), 2000142.

11. Liu, Y.; Li, F.; Qiu, L.; Yang, K.; Li, Q.; Zheng, X.; Hu, H.; Guo, T.; Wu, C.; Kim, T. W., Fluorescent Microarrays of in Situ Crystallized Perovskite Nanocomposites Fabricated for Patterned Applications by Using Inkjet Printing. *ACS Nano* **2019,** *13* (2), 2042-2049.

12. Sliz, R.; Lejay, M.; Fan, J. Z.; Choi, M.-J.; Kinge, S.; Hoogland, S.; Fabritius, T.; García de Arquer, F. P.; Sargent, E. H., Stable Colloidal Quantum Dot Inks Enable Inkjet-Printed High-Sensitivity Infrared Photodetectors. *ACS Nano* **2019**.

13. Dieleman, C. D.; van der Burgt, J.; Thakur, N.; Garnett, E. C.; Ehrler, B., Direct Patterning of CsPbBr3 Nanocrystals via Electron-Beam Lithography. *ACS Applied Energy Materials* **2022**.

14. Miszta, K.; Greullet, F.; Marras, S.; Prato, M.; Toma, A.; Arciniegas, M.; Manna, L.; Krahne, R., Nanocrystal Film Patterning by Inhibiting Cation Exchange via Electron-Beam or X-ray Lithography. *Nano Lett.* **2014,** *14* (4), 2116-2122.

15. Kim, T.-H.; Cho, K.-S.; Lee, E. K.; Lee, S. J.; Chae, J.; Kim, J. W.; Kim, D. H.; Kwon, J.-Y.; Amaratunga, G.; Lee, S. Y., Full-colour quantum dot displays fabricated by transfer printing. *Nat. Photonics* **2011,** *5* (3), 176.

16. Kothari, R.; Beaulieu, M. R.; Hendricks, N. R.; Li, S.; Watkins, J. J., Direct Patterning of Robust One-Dimensional, Two-Dimensional, and Three-Dimensional Crystalline Metal Oxide Nanostructures Using Imprint Lithography and Nanoparticle Dispersion Inks. *Chem. Mater.* **2017,** *29* (9), 3908-3918.

17. Yang, J.; Hahm, D.; Kim, K.; Rhee, S.; Lee, M.; Kim, S.; Chang, J. H.; Park, H. W.; Lim, J.; Lee, M.; Kim, H.; Bang, J.; Ahn, H.; Cho, J. H.; Kwak, J.; Kim, B.; Lee, C.; Bae, W. K.; Kang, M. S., High-resolution patterning of colloidal quantum dots via non-destructive, light-driven ligand crosslinking. *Nat. Commun.* **2020,** *11* (1), 2874.

18. Kim, W. J.; Kim, S. J.; Lee, K.-S.; Samoc, M.; Cartwright, A. N.; Prasad, P. N., Robust microstructures using UV photopatternable semiconductor nanocrystals. *Nano Lett.* **2008,** *8* (10), 3262-3265.

19. Hahm, D.; Park, J.; Jeong, I.; Rhee, S.; Lee, T.; Lee, C.; Chung, S.; Bae, W. K.; Lee, S., Surface Engineered Colloidal Quantum Dots for Complete Green Process. *ACS Appl. Mater. Interfaces* **2020,** *12* (9), 10563-10570.

20. Pan, J.-A.; Ondry, J. C.; Talapin, D. V., Direct Optical Lithography of CsPbX3 Nanocrystals via Photoinduced Ligand Cleavage with Postpatterning Chemical Modification and Electronic Coupling. *Nano Lett.* **2021,** *21* (18), 7609-7616.

21. Wang, Y.; Pan, J.-A.; Wu, H.; Talapin, D. V., Direct Wavelength-Selective Optical and Electron-Beam Lithography of Functional Inorganic Nanomaterials. *ACS Nano* **2019,** *13* (12), 13917-13931.

22. Wang, Y.; Fedin, I.; Zhang, H.; Talapin, D. V., Direct optical lithography of functional inorganic nanomaterials. *Science* **2017,** *357* (6349), 385-388.

23. Dong, A.; Ye, X.; Chen, J.; Kang, Y.; Gordon, T.; Kikkawa, J. M.; Murray, C. B., A generalized ligand-exchange strategy enabling sequential surface functionalization of colloidal nanocrystals. *J. Am. Chem. Soc.* **2010,** *133* (4), 998-1006.

24. Nag, A.; Kovalenko, M. V.; Lee, J.-S.; Liu, W.; Spokoyny, B.; Talapin, D. V., Metal-free inorganic ligands for colloidal nanocrystals: S2–, HS–, Se2–, HSe–, Te2–, HTe–, TeS32–, OH–, and NH2–as surface ligands. *J. Am. Chem. Soc.* **2011,** *133* (27), 10612-10620.

25. Rosen, E. L.; Buonsanti, R.; Llordes, A.; Sawvel, A. M.; Milliron, D. J.; Helms, B. A., Exceptionally mild reactive stripping of native ligands from nanocrystal surfaces by using Meerwein's salt. *Angew. Chem. Int. Ed.* **2012,** *51* (3), 684-689.

26. Doris, S. E.; Lynch, J. J.; Li, C.; Wills, A. W.; Urban, J. J.; Helms, B. A., Mechanistic insight into the formation of cationic naked nanocrystals generated under equilibrium control. *J. Am. Chem. Soc.* **2014,** *136* (44), 15702-15710.

27. Wang, W.; Pan, Z.; Rao, H.; Zhang, G.; Song, H.; Zhang, Z.; Zhong, X., Proton Initiated Ligand Exchange Reactions for Colloidal Nanocrystals Functionalized by Inorganic Ligands with Extremely Weak Coordination Ability. *Chem. Mater.* **2019**.

28. Maenosono, S.; Ozaki, E.; Yoshie, K.; Yamaguchi, Y., Nonlinear Photoluminescence Behavior in Closely Packed CdSe Nanocrystal Thin Films. *Japanese Journal of Applied Physics* **2001,** *40* (Part 2, No. 6B), L638-L641.

29. Manner, V. W.; Koposov, A. Y.; Szymanski, P.; Klimov, V. I.; Sykora, M., Role of Solvent–Oxygen Ion Pairs in Photooxidation of CdSe Nanocrystal Quantum Dots. *ACS Nano* **2012,** *6* (3), 2371-2377.

30. Dunstan, D. E.; Hagfeldt, A.; Almgren, M.; Siegbahn, H. O.; Mukhtar, E., Importance of surface reactions in the photochemistry of zinc sulfide colloids. *J. Phys. Chem.* **1990,** *94* (17), 6797-6804.

31. Spanhel, L.; Haase, M.; Weller, H.; Henglein, A., Photochemistry of colloidal semiconductors. 20. Surface modification and stability of strong luminescing CdS particles. *J. Am. Chem. Soc.* **1987,** *109* (19), 5649-5655.

32. Wang, F.; Yu, H.; Li, J.; Hang, Q.; Zemlyanov, D.; Gibbons, P. C.; Wang; Janes, D. B.; Buhro, W. E., Spectroscopic Properties of Colloidal Indium Phosphide Quantum Wires. *J. Am. Chem. Soc.* **2007,** *129* (46), 14327-14335.

33. Janke, E. M.; Williams, N. E.; She, C.; Zherebetskyy, D.; Hudson, M. H.; Wang, L.; Gosztola, D. J.; Schaller, R. D.; Lee, B.; Sun, C.; Engel, G. S.; Talapin, D. V., Origin of Broad Emission Spectra in InP Quantum Dots: Contributions from Structural and Electronic Disorder. *J. Am. Chem. Soc.* **2018,** *140* (46), 15791-15803.

34. Adam, S.; Talapin, D. V.; Borchert, H.; Lobo, A.; McGinley, C.; de Castro, A. R. B.; Haase, M.; Weller, H.; Möller, T., The effect of nanocrystal surface structure on the luminescence properties: Photoemission study of HF-etched InP nanocrystals. *The Journal of Chemical Physics* **2005,** *123* (8), 084706.

35. Srivastava, S.; Santos, A.; Critchley, K.; Kim, K.-S.; Podsiadlo, P.; Sun, K.; Lee, J.; Xu, C.; Lilly, G. D.; Glotzer, S. C.; Kotov, N. A., Light-Controlled Self-Assembly of Semiconductor Nanoparticles into Twisted Ribbons. *Science* **2010,** *327* (5971), 1355-1359.

36. Rivest, J. B.; Buonsanti, R.; Pick, T. E.; Zhu, L.; Lim, E.; Clavero, C.; Schaible, E.; Helms, B. A.; Milliron, D. J., Evolution of Ordered Metal Chalcogenide Architectures through Chemical Transformations. *J. Am. Chem. Soc.* **2013,** *135* (20), 7446-7449.

37. Buonsanti, R.; Pick, T. E.; Krins, N.; Richardson, T. J.; Helms, B. A.; Milliron, D. J., Assembly of Ligand-Stripped Nanocrystals into Precisely Controlled Mesoporous Architectures. *Nano Lett.* **2012,** *12* (7), 3872-3877.

38. Rauda, I. E.; Buonsanti, R.; Saldarriaga-Lopez, L. C.; Benjauthrit, K.; Schelhas, L. T.; Stefik, M.; Augustyn, V.; Ko, J.; Dunn, B.; Wiesner, U.; Milliron, D. J.; Tolbert, S. H., General

Method for the Synthesis of Hierarchical Nanocrystal-Based Mesoporous Materials. *ACS Nano* **2012,** *6* (7), 6386-6399.

39. Rauda, I. E.; Saldarriaga-Lopez, L. C.; Helms, B. A.; Schelhas, L. T.; Membreno, D.; Milliron, D. J.; Tolbert, S. H., Nanoporous Semiconductors Synthesized Through Polymer Templating of Ligand-Stripped CdSe Nanocrystals. *Adv. Mater.* **2013,** *25* (9), 1315-1322.

40. Ondry, J. C.; Robbennolt, S.; Kang, H.; Yan, Y.; Tolbert, S. H., A Room-Temperature, Solution Phase Method for the Synthesis of Mesoporous Metal Chalcogenide Nanocrystal-Based Thin Films with Precisely Controlled Grain Sizes. *Chem. Mater.* **2016,** *28* (17), 6105-6117.

41. Gupta, R.; Goddard, N. J., Broadband absorption spectroscopy for rapid pH measurement in small volumes using an integrated porous waveguide. *Analyst* **2017,** *142* (1), 169-176.

42. Girault, P.; Lorrain, N.; Lemaitre, J.; Poffo, L.; Guendouz, M.; Hardy, I.; Gadonna, M.; Gutierrez, A.; Bodiou, L.; Charrier, J., Racetrack micro-resonators based on ridge waveguides made of porous silica. *Opt. Mater.* **2015,** *50*, 167-174.

43. Burgess, I. B.; Koay, N.; Raymond, K. P.; Kolle, M.; Lončar, M.; Aizenberg, J., Wetting in Color: Colorimetric Differentiation of Organic Liquids with High Selectivity. *ACS Nano* **2012,** *6* (2), 1427-1437.

44. Singleton, T. A.; Burgess, I. B.; Nerger, B. A.; Goulet-Hanssens, A.; Koay, N.; Barrett, C. J.; Aizenberg, J., Photo-tuning of highly selective wetting in inverse opals. *Soft Matter* **2014,** *10* (9), 1325-1328.

45. Campo, A. d.; Greiner, C., SU-8: a photoresist for high-aspect-ratio and 3D submicron lithography. *Journal of Micromechanics and Microengineering* **2007,** *17* (6), R81-R95.

46. Hellgren, N.; Steves, M. A.; Shallenberger, J.; O'Boyle, S. K.; Mellott, E.; Noble, A. R., Effect of etching on the oxidation of zinc selenide surfaces characterized by X-ray photoelectron spectroscopy. *Appl. Surf. Sci.* **2020,** *528*, 146604.

47. Dabbousi, B. O.; Rodriguez-Viejo, J.; Mikulec, F. V.; Heine, J. R.; Mattoussi, H.; Ober, R.; Jensen, K. F.; Bawendi, M. G., (CdSe)ZnS Core−Shell Quantum Dots: Synthesis and Characterization of a Size Series of Highly Luminescent Nanocrystallites. *The Journal of Physical Chemistry B* **1997,** *101* (46), 9463-9475.

48. Atkinson, H. V.; Davies, S., Fundamental aspects of hot isostatic pressing: An overview. *Metallurgical and Materials Transactions A* **2000,** *31* (12), 2981-3000.

49. Flamee, S.; Cirillo, M.; Abe, S.; De Nolf, K.; Gomes, R.; Aubert, T.; Hens, Z., Fast, High Yield, and High Solid Loading Synthesis of Metal Selenide Nanocrystals. *Chem. Mater.* **2013,** *25* (12), 2476-2483.

50. Herron, S. M.; Lawal, Q. O.; Bent, S. F., Polysulfide ligand exchange on zinc sulfide nanocrystal surfaces for improved film formation. *Appl. Surf. Sci.* **2015,** *359*, 106-113.

51. Joo, J.; Yu, T.; Kim, Y. W.; Park, H. M.; Wu, F.; Zhang, J. Z.; Hyeon, T., Multigram scale synthesis and characterization of monodisperse tetragonal zirconia nanocrystals. *J. Am. Chem. Soc.* **2003,** *125* (21), 6553-6557.

52. Tirosh, E.; Markovich, G., Control of defects and magnetic properties in colloidal HfO2 nanorods. *Adv. Mater.* **2007,** *19* (18), 2608-2612.

Chapter 6. Conclusions and Outlook

6.1. Thesis summary

In summary, this thesis has focused on the development and study of chemical approaches for the direct photolithography of colloidal inorganic nanomaterials. This patterning relies upon the light-induced solubility change of NCs through various photo-chemical pathways. This involves either using photosensitive binding ligands, photosensitive additives or through photo-chemical reactions of the surface ions. Using various chemical approaches, we elucidated the mechanism of how each photo-chemical reaction leads to the change in NC solubility. Photo-sensitive ligands were designed to be sensitive to different wavelengths of light and their suitability for different classes of nanomaterials was studied.

The properties of these NC patterns made by direct photolithography were also thoroughly evaluated. We found that high resolution patterns with < 1 μm feature sizes were achievable, which is limited by the resolution of the light exposure system. The doses that were needed to induce solubility change depends on the specific photo-chemical process but were very comparable to commercial photoresists. We were also able to patterns nanoparticles with thicknesses up to 1 μm, which opens the door for their use as diffractive optical elements and in other photonic devices.

We also studied the effect of the direct patterning process on the quality of the resulting NCs in the patterns. For photoluminescent NCs, we found that the PLQY of the NCs depends highly on the photo-chemical approach used. With an optimized photosensitizer, PLQYs remain as high as 75% of un-patterned NCs. For perovskite NCs, we were able to achieve a 79% absolute PLQY of patterned film by introducing a post-patterning treatment step that improves the surface passivation. We also demonstrated the utility of photo-patterning through the fabrication and

testing of various patterned NC-based devices including photodetectors, diffractive optical elements, and light-emitting diodes. These proof-of-concept devices showcase the importance of obtaining high-quality NC patterns in the fabrication more advanced NC-based photonic and optoelectronic devices. This expands the application of colloidal NCs and helps in their integration in next-generation devices.

6.2. Future directions

In this final section, I will discuss potential future directions that builds upon the work done in this thesis. One area that can be further expanded is the photosensitive ligand chemistry. In this thesis, we limited our scope to commercially available ligands or simple ligands that can be synthesized with just a few steps. I believe that we were only scratching the surface in the possibilities of chemical pathways that can be applied for direct patterning of NCs. However, exploring future generations of photosensitive ligands should be guided by either a specific desirable NC property, an application goal, or the requirement of a specific wavelength of light or other stimuli. For instance, one may want to investigate photosensitive ligands that can further improve the PLQY of NC patterns while leaving behind as little organic residue as possible. Most of the photosensitive stabilizing ligands used in this thesis involves the binding of a thiol group to the NC surface. Since thiols are not considered the best ligands for preserving high PLQY, other chemical approaches can be explored to leave behind a more amenable surface group upon patterning. Another example could be the development of ligands that are sensitive to infrared (IR) light that can reduce the NC solubility upon IR irradiation. This could allow visible-light absorbing QDs to be patterned with larger thicknesses due to deeper penetration of the IR light. All these examples rely on the further expansion of photosensitive ligand chemistry.

Another direction to be explored is the improvement of the NC pattern resolution, which opens its use in another range of applications. For example, the fabrication of high-performance metasurfaces relies upon the patterning of features with below 500 nm, which is currently beyond the capabilities of the work in this thesis. Similar feature sizes are required for making distributed feedback lasers using NCs. To properly explore the resolutions limitations of DOLFIN, an appropriate high-resolution exposure method is required. One relatively simple way to obtain diffraction limited light exposure is using interference lithography such as Lloyd lithography. This method of exposure allows the exposure of 1D strips with feature sizes down to $\lambda/2$, where λ is the exposure wavelength. Hence, Lloyd lithography can be used as a simple way to test the resolution limits of a particular patterning chemistry. Once a suitable patterning chemistry had been found for high-resolution patterning, more complex high-resolution features can be patterned using more sophisticated exposure "steppers".

Most of the work done in this thesis involves two-dimensional (2D) patterns, whereby there is only arbitrary control in the x-y plane of the substrate but not in the height of the patterns. Extending this patterning chemistry into the third dimension is a very interesting path forward that could have a potential impact on the 3D-printing community. This is because most 3D-printing approaches are often limited to a relatively small library of polymer or organic-based materials. On the other hand, here have not been many approaches to 3D-print high-quality inorganic structures. The 3D-printing of NCs may overcome some of the limitations of current approaches due to the pre-formed crystallinity of the NCs; this enables relatively mild conditions to be used to obtain a densified 3D structures compared to methods that require high thermal treatments for densification.

The 3D patterning of NCs can be explored on two different platforms. The first platform is through two-photon lithography (2PL), which is an expensive technique but allows for the patterning of sub-micron features and the use of very small amounts of material. On the other hand, 3D printing through stereolithography, or digital light projection (DLP) has reached commercial viability and is very affordable (<$400 for a DLP 3D-printer). However, its resolution is typically limited to >100 μm and it requires more material. Another significant difference between these two techniques is that 2PL can be used on a dried NC film, while DLP relies upon the photo-induced gelation of a liquid precursor. From this standpoint, 2PL should be an easier extension from the 2D patterning approaches in this thesis. The only change that needs to be considered is the two-photon absorption cross-section of the sensitizer. For DLP printing, preliminary studies have shown that the photo-induced solubility changes of the NCS does not usually provide sufficient forces to drive the liquid to solid gelation process that is required for the formation of 3D features. Further studies need to be done on both the photochemistry and processing of the NCs that can allow for robust photo-induced gelation.

Finally, we can use this direct photopatterning approach for other applications that have not been explored in this thesis. For example, the proper control of the porosity of the NC patterns may allow it to be use for chemical sensing or as porous waveguides. Different types of NCs with different surface functionalization can be patterned as an array that allows for a high sensitivity and/or specificity in the sensing of gas molecules. Another idea involves the patterning of self-assembled NCs, which opens the controlled micro-fabrication of ordered arrays of NCs. Also, it would be interesting to demonstrate the fabrication of a functional devices (e.g., transistor or LED) that only utilizes the direct patterning of various types NCs (with no steps required vapor-phase

deposition). This would show the capability of a completely solution-processed deposition and patterning approach that is low-cost, simpler, and more scalable than traditional approaches.